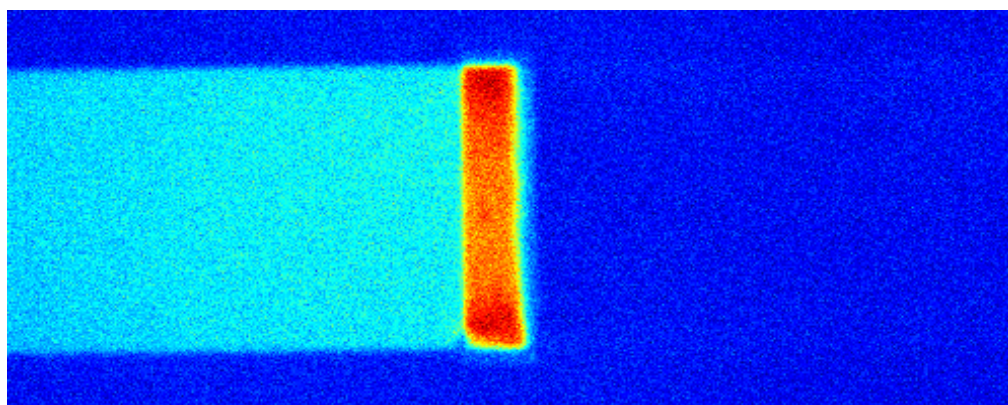


Master Thesis, s031849

# Theoretical aspects of nonlinear electrokinetic phenomena in microfluidics

Mathias Bækbo Andersen



Supervisor: Professor Henrik Bruus

Department of Micro- and Nanotechnology  
Technical University of Denmark

27 January 2009

The picture on the front page is a post-processed optical epifluorescence microscopy image from an experiment conducted in the Nanolab at University of California, Santa Barbara.

# Abstract

We present results from two investigations: (*i*) a combined experimental and numerical study of electrically induced concentration drops across un-biased electrodes in buffer-filled microchannels, and (*ii*) a purely numerical comparison of a full nonlinear model, a linear slip-velocity model, and a nonlinear slip-velocity model.

First, we have made a parametric study of concentration drops in fluorescent dyes across un-biased, metal electrodes in microchannels. Then, we make a numerical 2D model of our system and find in agreement with the experimental observations: (*i*) a concentration drop in the dye across the un-biased electrode, (*ii*) the drop increases with increasing applied voltage, (*iii*) the drop is affected by the concentration of buffer and dye, and (*iv*) high concentration enrichment of dye on the un-biased electrode. Furthermore, we use our numerical results to give insight into the dynamics of the concentration drop phenomenon.

Secondly, we do a purely numerical investigation of three different electrokinetic models. These models are widely used and rely on different degrees of approximation; a surprisingly large deviation between the most simple and more comprehensive model is found. The model system is a planar, un-biased electrode in a microchamber filled with a binary, symmetric electrolyte, subjected to an external and homogeneous electric field. This field gives rise to a symmetric induced-charge electro-osmotic (ICEO) flow on the electrode which is quantified in the three models by its kinetic energy. The characterization is done for different strengths of the applied electric field ranging from linear to nonlinear regimes. Additionally, we vary the Debye-length-to-electrode-width ratio going from a very thick to a very thin double layer. Even for parameters where the approximation of the simple model is generally thought of to be good ( $\lambda_D/a = 0.01$  and  $aE < k_B T/(Ze)$ ) it overestimates the ICEO flow energy by around 25%. This discrepancy has so far been unnoticed and the discovery might help explain some of the large differences when comparing other experimentally observed electrokinetic phenomena to the simple model.



# Resumé

Vi præsenterer resultater fra to undersøgelser: (*i*) en kombination af eksperimentelt arbejde og numeriske beregninger på elektrisk inducerede fald i koncentrationer henover metal objekter i buffer-fyldte mikrokkanaler og (*ii*) en ren numerisk sammenligning en komplet ikke-lineær model, af en lineær slip-hastigheds model og en ikke-lineær slip-hastigheds model.

Første pointe er, at vi har lavet en undersøgelse for flere parametre af faldet i koncentration af fluorescens-aktive farvestoffer henover et metal objekt i en mikrokkanal. Vi laver herefter en numerisk 2D model af vores system og finder i overensstemmelse med de eksperimentelle resultater: (*i*) et fald i koncentrationen af farvestof henover metal objektet, (*ii*) faldets størrelse stiger når den påtrykte spændingsforskel øges, (*iii*) faldet er afhængig af koncentrationen af buffer og farvestof og (*iv*) stor forøgelse i koncentrationen af farvestof på metal objektet. Vi bruger herefter vores numeriske model til at undersøge fænomenet.

Andet hovedresultat er en ren numerisk undersøgelse af tre forskellige elektrokinetiske modeller. Disse modeller er velkendte og baseret på forskellige antagelser. Vi viser, at der er en overraskende stor forskel mellem den mest simple og den mere omfattende model. Vores model system består af et plant stykke metal i et mikrokammer fyldt med en binær og symmetrisk elektrolyt. Vi påtrykker et homogent elektrisk felt, som giver anledning til et symmetrisk, induceret-ladning elektro-osmotisk (induced-charge electro-osmotic ICEO) flow på metallet. Vi sammenligner den kinetiske energi i de inducerede flows for de forskellige modeller og for forskellige styrker af det påtrykte elektriske felt. Vi går fra det lineære til det ikke-lineære regime, og for forskellige Debye-længde til metal-bredde forhold, gående fra et meget tykt til et meget tyndt Debye-lag. Selv for parametre hvor den simple model forventes at give præcise resultater ( $\lambda_D/a = 0.01$  and  $aE < k_B T / (Ze)$ ) overestimerer den ICEO flowets energi med omkring 25%. Denne afvigelse har været upåagtet indtil nu og opdagelsen kan måske hjælpe med at forklare nogle af de store forskelle mellem andre eksperimentelle observationer og den simple model.



# Preface

The present thesis is submitted as fulfillment of the prerequisites for obtaining the Master of Science and Engineering degree at the Technical University of Denmark (DTU). The work has been carried out at the Department of Micro- and Nanotechnology (DTU Nanotech) in the Theoretical Microfluidics Group (DTU-TMF group) headed by professor Henrik Bruus. The duration of this 50 ECTS credits project is the 12 month period from January 2008 to January 2009.

I have had a terrific time in the DTU-TMF group, and I have enjoyed a working environment that has been both professional and social rewarding. This is in part due to the great facilities that have been put to my disposal by the department, and in part due to the great people. I would like to thank all the people from DTU Nanotech, and especially I would like to emphasize my most sincere gratefulness to professor Henrik Bruus for being a fantastic supervisor; Misha Marie Gregersen for answering questions of all kinds, but especially on electrokinetics; Martin Heller, likewise, for answering my questions, especially on COMSOL and Latex; Rune Barnkob for being an unsurpassed fellow student, and the rest of the people I know through the DTU-TMF group.

During the project, I spent around two months in the Nanolab of professor Sumita Pennathur at the University of California, Santa Barbara (UCSB-Nanolab). My stay there was more than pleasant. I want to thank everybody in the Nanolab, but in particular professor Sumita Pennathur for her unrivaled hospitality and great personality; Gaurav Soni for his openness and for taking his time to help me; Trevor Wolfcale and Jared Frey for invaluable collaboration on the experimental part, both at and while away from the UCSB-Nanolab.

Finally, I would like to thank my family for their support and especially my wife Maria for always being there for me.

Mathias Bækbo Andersen  
Department of Micro- and Nanotechnology  
Technical University of Denmark  
27 January 2009





# Contents

<b>List of Figures</b>	<b>xiii</b>
<b>List of Tables</b>	<b>xv</b>
<b>List of Symbols</b>	<b>xvii</b>
<b>1 Introduction</b>	<b>1</b>
1.1 Microfluidics . . . . .	1
1.2 Electrokinetic phenomena . . . . .	3
1.3 Outline of thesis . . . . .	4
1.4 Publications during the MSc studies . . . . .	5
<b>2 Experimental motivation</b>	<b>7</b>
2.1 Nanofluidics . . . . .	7
2.2 Fluorescence microscopy . . . . .	8
2.3 Experimental procedure . . . . .	10
2.4 The microfluidic chip . . . . .	11
2.5 Buffers . . . . .	12
2.6 Fluorescence dye . . . . .	14
2.7 Post-processing and experimental observations . . . . .	15
2.7.1 Concentration drop across a rectangular un-biased electrode . . . . .	16
2.7.2 Diffusion of BODIPY . . . . .	18
2.8 Unexplained electrokinetic phenomena . . . . .	19
<b>3 Electrokinetic theory</b>	<b>21</b>
3.1 Basic physical picture . . . . .	21
3.2 Full nonlinear model . . . . .	22
3.2.1 Continuity equation . . . . .	23
3.2.2 Momentum conservation . . . . .	23
3.2.3 Electric interaction . . . . .	24
3.2.4 Transport of species . . . . .	25
3.2.5 Remark on the full nonlinear model . . . . .	26
3.2.6 The electric double layer at a charged surface . . . . .	26
3.2.7 Infinite plane . . . . .	27

3.2.8	Parallel plates channel . . . . .	28
3.2.9	Application of external electric field to parallel plates channel . . . .	28
3.3	Slip-velocity models . . . . .	30
3.3.1	Effective slip-velocity boundary condition for the linear and nonlinear slip-velocity models . . . . .	30
3.3.2	Bulk equations for the linear and nonlinear slip-velocity models . . .	31
3.4	Linear slip velocity model . . . . .	32
3.5	Nonlinear slip velocity model . . . . .	32
3.5.1	Induced-charge electro-osmosis . . . . .	32
3.5.2	Surface conduction . . . . .	33
3.5.3	Charge conservation in the double layer . . . . .	34
<b>4</b>	<b>Numerical implementation and validation in COMSOL</b>	<b>37</b>
4.1	Weak form implementation in COMSOL . . . . .	37
4.1.1	Short derivation of the weak form . . . . .	38
4.1.2	Weak constraints . . . . .	38
4.2	Validation . . . . .	39
4.2.1	Model . . . . .	40
4.2.2	Boundary conditions . . . . .	41
4.2.3	Results . . . . .	41
<b>5</b>	<b>Numerical analysis of analyte transport across un-biased electrodes in microchannels</b>	<b>43</b>
5.1	Model system . . . . .	43
5.2	Boundary conditions . . . . .	45
5.3	Initial conditions . . . . .	46
5.4	Numerics in COMSOL . . . . .	46
5.4.1	Constant potential on the un-biased electrode . . . . .	46
5.4.2	Logarithmic concentration fields . . . . .	47
5.5	Results . . . . .	48
5.6	Discussion . . . . .	49
5.7	Conclusion . . . . .	51
<b>6</b>	<b>Numerical analysis of finite Debye-length effects in induced-charge electro-osmosis</b>	<b>55</b>
6.1	Introduction . . . . .	55
6.2	Model system . . . . .	56
6.3	Full nonlinear model (FN) . . . . .	57
6.3.1	Dimensionless form . . . . .	57
6.3.2	Boundary conditions . . . . .	58
6.3.3	The strongly nonlinear regime . . . . .	59
6.4	The linear slip-velocity model (LS) . . . . .	59
6.4.1	Dimensionless form . . . . .	60
6.5	The nonlinear slip-velocity model (NLS) . . . . .	61

---

6.5.1	Dimensionless form . . . . .	61
6.6	Numerics in COMSOL . . . . .	61
6.6.1	Convergence analysis . . . . .	62
6.7	Results . . . . .	63
6.7.1	Zero height of the un-biased electrode . . . . .	63
6.7.2	Finite height of the un-biased electrode . . . . .	66
6.8	Conclusion . . . . .	67
<b>7</b>	<b>Conclusion and outlook</b>	<b>69</b>
<b>A</b>	<b>Borate buffer and fluorescein dye</b>	<b>71</b>
A.1	Borate buffer . . . . .	71
A.2	Fluorescein dye . . . . .	72
<b>B</b>	<b>COMSOL–MATLAB script for EO-flow in parallel plates</b>	<b>73</b>
<b>C</b>	<b>COMSOL–MATLAB script for concentration drop across un-biased electrode in a microchannel</b>	<b>75</b>
<b>D</b>	<b>COMSOL–MATLAB scripts for finite Debye-length investigation</b>	<b>81</b>
D.1	Grid Engine script for utilizing the high performance computing facility at DTU . . . . .	81
D.2	Full nonlinear model . . . . .	82
D.3	Linear slip model . . . . .	86
D.4	Nonlinear slip model . . . . .	87
	<b>Bibliography</b>	<b>91</b>



# List of Figures

1.1	Development in the number of scientific papers that includes the keyword <i>microfluidic</i> . . . . .	2
2.1	(a) Stokes shift (b) Dichromatic mirror . . . . .	9
2.2	(a) Picture of the experimental setup (b) Schematic of the epifluorescence setup . . . . .	10
2.3	(a) Picture of a microchip. (b) Sketch of a microchannel. . . . .	11
2.4	(a) Molecular structure of a BODIPY molecule (b) Spectral absorption and emission profiles for BODIPY . . . . .	15
2.5	(a) 3D view of microchip. (b) Top-down view on microchip. (c) Authentic raw data image . . . . .	15
2.6	(a) The corrected intensity $I_{\text{corr}}$ . (b) Plot of $I_x$ . . . . .	17
2.7	Example of the spatial and temporal evolution of the intensity in a microchannel . . . . .	17
2.8	Frames from experiemtal movie . . . . .	18
2.9	Experimental diffused length . . . . .	19
3.1	(a) Microscopic view of the interface region. (b) Sketch of electric potential and concentrations. . . . .	22
3.2	(a) Two wall EO-flow. (b) One wall EO-flow. . . . .	29
3.3	One- and two-wall EO-flow velocity profiles . . . . .	31
3.4	Symmetric ICEO on a flat, planar, and un-biased electrode . . . . .	33
3.5	Sketches for the derivation of the surface charge conservation law . . . . .	35
4.1	EO-flow validation, computational domain . . . . .	40
4.2	Parallel plates EO-flow . . . . .	42
5.1	The 2D computational domain. . . . .	44
5.2	Steady-state concentration drop for low buffer concentrations. . . . .	49
5.3	Steady-state concentration drop for high buffer concentrations. . . . .	50
5.4	Explanation plots . . . . .	53
5.5	Plot of the charge density . . . . .	54
6.1	Model system . . . . .	56

---

6.2	Computational domain with governing equations. . . . .	58
6.3	Computational domain for the strongly nonlinear regime. . . . .	60
6.4	Mesh convergence analysis. . . . .	62
6.5	Kinetic energies relative to the linear slip-velocity model. . . . .	64
6.6	Differences in induced kinetic energies. . . . .	65
6.7	Differences in kinetic energies relative to the full nonlinear model. . . . .	65
6.8	Kinetic energies for finite height electrode. . . . .	66
A.1	(a) Molecular structure of fluorescein (b) Spectral absorption and emission profiles for fluorescein . . . . .	72

# List of Tables

2.1	Concentrations of charged species in the phosphate buffers . . . . .	14
2.2	Concentrations of BODIPY . . . . .	14
4.1	EO-flow calculation parameters . . . . .	42
5.1	Variable parameters. . . . .	44
5.2	Constant parameters. . . . .	45
A.1	Concentrations of charged species in the borate buffers . . . . .	71





# List of Symbols

Symbol	Description	Unit
$\mathbf{v}$	Velocity vector	$\text{m s}^{-1}$
$\mathbf{E}$	Electric field	$\text{V m}^{-1}$
$\varepsilon_0$	Electric permittivity of vacuum	$\text{F m}^{-1}$
$\zeta$	Potential at outer Helmholtz layer	V
$\eta$	Dynamic viscosity	$\text{Pa s}$
$a$	Characteristic length	m
$e$	Elementary charge	C
$V_0$	Potential difference	V
$k_B$	Boltzmann constant	$\text{J K}^{-1}$
$T$	Temperature	K
$\rho_b$	Mass density (of buffer)	$\text{kg m}^{-3}$
$\partial_j = \frac{\partial}{\partial x_j}$	Partial derivative after $j$ th co-ordinate	
$\nabla$	Nabla or gradient operator	
$\nabla \cdot$	Divergence operator	
$\nabla \times$	Rotation operator	
$\nabla^2$	Laplace operator	
$p$	Pressure	Pa
$\beta$	Dimensionless viscosity ratio and dimensionless height ratio	
$\rho_{\text{el}}$	Electric charge density	$\text{C m}^{-3}$
$\lambda_D$	Debye–Hückel screening length	m
$c^{(i)}$	Concentration of species $i$	$\text{m}^{-3}$
$c_a$	Speed of sound	$\text{m s}^{-1}$
$\mathbf{J}$	Particle current density	$\text{m}^{-2} \text{s}^{-1}$
$\mu$	Chemical potential	J
$Z$	Valence	
$\phi$	Potential	V
$D$	Diffusivity	$\text{m}^2 \text{s}^{-1}$
$\omega$	Angular frequency	$\text{s}^{-1}$
$c_l$	Speed of light in vacuum	$\text{m s}^{-1}$
$\mathbf{D}$	Electric displacement	$\text{C m}^{-2}$

Symbol	Description	Unit
$t$	Time	s
$\mathbf{r}$	Position vector	m
$\nu$	Kinematic viscosity	$\text{m}^2 \text{s}^{-1}$
$\epsilon$	Dimensionless ratio	
$Re$	Reynolds number, inertial force to viscous force	
$pK_a$	Equilibrium constant	
$\sigma$	Electric conductivity or hydrodynamic stress tensor	$\text{A V}^{-1} \text{m}^{-1}$ or $\text{Pa m}^{-1}$
$\mu_{eo}$	Electro-osmotic mobility	$\text{m}^2 \text{V}^{-1} \text{s}^{-1}$
$Q$	Volumetric flow rate	$\text{m}^3 \text{s}^{-1}$
$\rho_b$	Mass density	$\text{kg m}^3$
$\sigma_s$	Surface conductivity	$\text{A V}^{-1}$
$\mathbf{J}_s$	Electrical surface current	$\text{C m}^{-1} \text{s}^{-1}$
$q$	Surface charge density	$\text{C m}^{-2}$
$v_{eo}$	Electro-osmotic velocity	$\text{m s}^{-1}$

# Chapter 1

## Introduction

The title of the current thesis *Theoretical aspects of nonlinear electrokinetic phenomena in microfluidics* contains several concepts which might be more or less familiar to the reader. This chapter is meant to give an introduction to these concepts, in particular to microfluidics and electrokinetic phenomena.

Microfluidics, i.e. the physical properties of liquids and solutions at the micrometer scale, is a framework that enables a whole new range of scientific and technological possibilities, especially in the development of microdevices for medical and biological use.

Secondly, electrokinetic phenomena is introduced and linked to microfluidics. The sections on microfluidics and electrokinetic phenomena are mainly based on *Stone et al.* [1].

### 1.1 Microfluidics

Microfluidics refers to devices and methods for controlling and manipulating fluid flows with length scales less than a millimeter. Such studies are not new but have for a long time been part of colloid science and plant biology.

However, within the last decade there has been a major increase in the research within the area [2], see Figure 1.1, which among other things is due to (*i*) the general spread of tools for fabricating microfluidic systems, (*ii*) a growing trend within biology and biotechnology where using small quantities and very small volumes gives advantages, (*iii*) a desire to make cheap portable devices for fast point-of-care analysis, and (*iv*) using microfluidics for fundamental studies of physical, chemical and biological processes.

Microfluidics utilizes many different components such as valves, pumps, sensors, mixers, filters, separators, heaters etc. These are combined into lab-on-a-chip systems in which one tries to do such things as chemical synthesis, analysis, and reactions only by using very small fluid volumes. One of the advantages of microfluidics is then that a single channel is easily replicated and large networks can be built.

Manipulation of microfluidic flows can be obtained by using different external fields (pressure, electric, magnetic, capillary etc.). In general, when dimensions shrink, the relative importance of surface to volume forces increases. The manipulation can be achieved

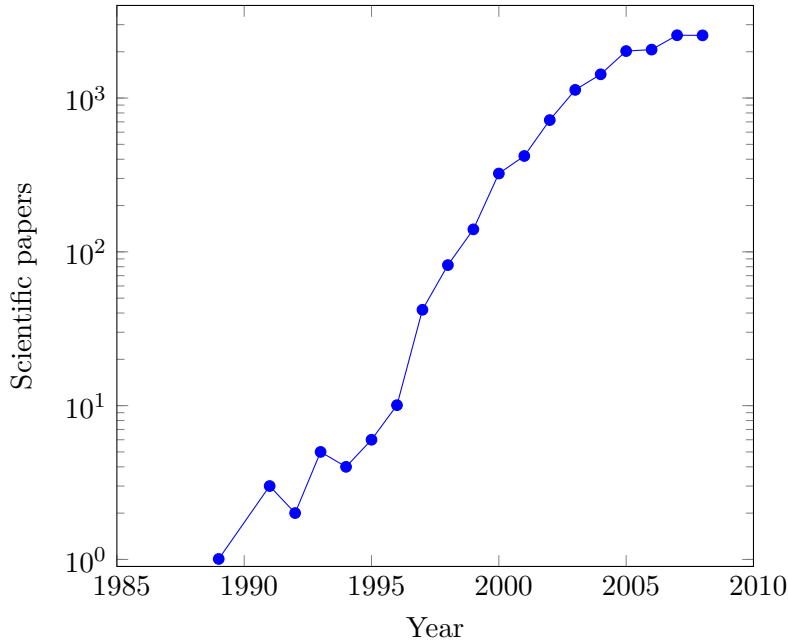


**Figure 1.1:** Semilogarithmic plot of the number of scientific papers per year from a search on the keyword microfluidic in the citation database *ISI Web of Knowledge* [2]. It is clear from the trend of the graph that microfluidic is an area of new and increasing interest.

by either applying the external field at inlets and outlets, or it can be applied locally in the microchannel by integrated components.

Visualization of microflows can be accomplished by use of optical microscopes. One technique is particle image velocimetry (PIV) which can yield a spatial resolution of the flow approximately down to one micron. Another approach is fluorescence microscopy, which we use in this work and which will be introduced in Chapter 2.

A typical microchannel is produced with planar lithographic techniques and has a rectangular cross section, and the working fluid is most often water. Normally the Reynolds number is very low (on the order of unity or smaller) which means that viscosity dominates and the convective term of the Navier–Stokes equations are insignificant. This means that microflows most often are laminar and consequently that the typical velocity profiles in simple geometries are parabolic for pressure-driven flows and almost uniform for electro-osmotic flows (EO-flows), and in the general situation a superposition of both. Another consequence of the low value of the Reynolds number is that turbulence is very rare in microflows, and hence it is difficult to achieve mixing.

As a result, the Stokes equation is often applicable for incompressible fluids and combined with no-slip boundary conditions analytical solutions can be derived for simple geometries. As an example, the volumetric flow rate  $Q$  through a rectangular channel with width  $w$  and height  $h$  generated from a pressure drop  $\Delta p$  over a distance  $L$  is to a good approximation given by the expression  $Q \approx wh^3 \Delta p (1 - 0.630h/w)/(12\eta L)$ , with  $\eta$  being the dynamic viscosity of the fluid [3]. The factor of  $wh^3$  shows the significant impact

of changes in the smallest dimensions.

## 1.2 Electrokinetic phenomena

Electrokinetics refers to the coupling between electric currents and mass flow in electrolytes. This coupling is often due to the electric Debye screening layer that forms at charged interfaces.

When the walls surrounding a liquid are charged, there is one electro-hydrodynamic effect especially important for the current work; electro-osmosis which is the flow generated from the application of an electric field in a liquid-filled channel. Another effect, not central in the current work, is called streaming current, which is when a pressure driven flow drags ions tangential to the surface and thereby generates an electric current. A similar coupling is responsible for the third effect called electrophoresis where an electric field acts on the charged interface between an immersed charged (colloidal) object and the fluid thereby making the particle move. Yet another effect is called sedimentation potential which is generated by charged particles moving relative to a stationary liquid.

In general, when an electrolyte is brought in contact with a surface, there will be a charge transfer at the interface. This happens either by ionization of covalently bound surface groups, or by ion adsorption. This means that there is a region close to the interface which is not electroneutral (e.g. common glass SiOH in the presence of water, ionizes to produce charged surface groups  $\text{SiO}^-$ , and releases a proton).

The net charge at the interface in the electrolyte will be attracted to the surface by electrostatic forces but this is opposed by thermal fluctuations whereby a charged layer, called the Debye layer, of characteristic thickness  $\lambda_D$  is generated. In water  $\lambda_D \approx 1 - 100 \text{ nm}$  and in most situations the electrolyte is charge-neutral a couple of Debye lengths from the interface.

When an electric field  $E_{\text{ext}}$  is applied along a channel, a conductive current and the corresponding local field  $E$  are established throughout the liquid. Since the bulk electrolyte is charge neutral it will not experience any body force. However, the non-zero charge density in the Debye layer will experience a force from the local electric field  $E$  that is tangent to the surface and thereby generate a body force on the fluid which induces a shear. As a result, the fluid velocity will go from zero at the no-slip surface to a finite value  $\mu_{\text{eo}}E$  at the edge of the thin Debye layer, where  $\mu_{\text{eo}}$  is a local mobility characteristic of the surface. This mobility is dependent on the surface charge  $q$  and for small surface potentials  $\zeta$  the following relation is valid  $\mu_{\text{eo}} = q\lambda_D/\eta = \varepsilon_r\varepsilon_0\zeta/\eta$  where  $\varepsilon_r$  is the dielectric constant of the electrolyte and  $\varepsilon_0$  is the vacuum permittivity. In common devices, the Debye layer is much smaller than any of the macroscopic dimensions (channel widths or heights) and the liquid therefore appears to have a slip velocity  $\mu_{\text{eo}}E$  along the surface. This simplification makes it possible to decouple the electrostatic problem from the hydrodynamic problem by introducing the slip velocity as an effective slip boundary condition. But as we show in this thesis, it is not without loss of accuracy to use this boundary condition.

The magnitude of the EO-flow is independent of channel dimensions (if larger than  $\lambda_D$ ) and is solely dependent on the effective slip velocity. Typical surface potentials have

values around tens of millivolts which gives a mobility for aqueous solutions of  $\mu_{\text{eo}} \approx 7 \times 10^{-9} \text{ m}^2 \text{ V}^{-1} \text{ s}^{-1}$  meaning that to get a velocity of a few millimeters per second requires electric fields of the order  $10^5 \text{ V m}^{-1}$ . Consequently, to create such an electric field between the ends of a centimeter-long channel requires a drop in the electrostatic potential in the kilovolt range which is rather impracticable for portable devices.

Electrokinetic phenomena can be important and useful in microfluidics due to some important features which are (i) in a microchannel of width  $w$  and height  $h$  the electro-osmotic volume flow scales with  $wh$  for a given potential drop, whereas the volume flow in a pressure driven flow scales with  $wh^3$ . (ii) The small cross-section of a microchannel makes the ohmic resistance of the electrolyte-filled channel very high whereby high electric fields can be applied using very low currents. In addition, ohmic heating is generally limited by the efficient removal of thermal energy in narrow geometries. (iii) Usually the EO-flow is a plug flow which means that sample analytes can be transported without broadening due to hydrodynamic dispersion as in pressure-driven flows. (iv) The ability to integrate local electric components in a microchannel allows for local manipulation of the EO-flow.

### 1.3 Outline of thesis

#### Chapter 2: Experimental motivation

We start by giving an experimental motivation for the current work. We introduce optical epifluorescence microscopy as it is used to obtain the experimental data that forms the basis and starting point for this thesis. Next, we give a description of the experimental setup which leads to a short review of simple buffer theory. After presenting the specific buffer and dye used in this report, we give some examples of experimental observations. Finally, a general motivation for the study of nonlinear electrokinetic phenomena is given based on unresolved problems from the literature.

#### Chapter 3: Electrokinetic theory

The governing equations are introduced in this chapter. From these we define three models: (i) the full nonlinear model, also known as the Poisson–Nernst–Planck model, (ii) the linear slip-velocity model, and (iii) the nonlinear slip-velocity model. The main assumption in the two slip-velocity models are the Helmholtz–Smoluchowski slip velocity, which we derive for the parallel plates channel. Finally, we give a detailed derivation of the charge conservation law that leads to an effective PDE boundary condition in the nonlinear model.

#### Chapter 4: Numerical implementation and validation in COMSOL

We use the finite-element-software COMSOL for the numerical simulations and thus we introduce it in this chapter. The special COMSOL syntax called weak form is presented as we use it extensively in the current work. Finally, we benchmark our code against the analytical solution for an EO-flow in a parallel plates channel.

**Chapter 5: Numerical analysis of analyte transport across un-biased electrodes in microchannels**

In this chapter we set up a numerical model for the experimental system. Then, we run simulations for different parameters and compare the results against our experimental data. We achieve the main goal; to reproduce the observed concentration drop. Additionally, we get some qualitative reproduction between our numerical model and the experiments when we vary the applied voltage and the concentrations of buffer and dye.

**Chapter 6: Numerical analysis of finite Debye-length effects in induced-charge electro-osmosis**

We have discovered a large discrepancy in calculated flow kinetic energy between different electrokinetic models. Thus, we nondimensionalize the governing equations and do a parametric study of the induced flow kinetic energies using the three electrokinetic models. Additionally, we show that the kinetic energy in the induced flow increases up to five times if the finite height of an electrode is included. Our results may help explain the difference in experimentally observed ICEO flow velocities and those from numerical simulations using the linear slip-velocity model.

**Chapter 7: Conclusion and outlook**

We present concluding remarks on our work on nonlinear electrokinetics.

**1.4 Publications during the MSc studies**

1. M.B. Andersen, M.M. Gregersen, T. Wolfcale, S. Pennathur, and H. Bruus, “Microchannel electrokinetics of charged analytes in buffered solutions near floating electrodes”, GAMM 2009, *The 80th annual meeting of the international association of applied mathematics and mechanics*, Gdansk, Poland, February 9th to 13th, 2009.
2. M.M. Gregersen, M.B. Andersen, G. Soni, C. Meinhart, and H. Bruus, “A numerical analysis of finite Debye-length effects in induced-charge electro-osmosis”, (*Phys. Rev. E.*, submitted, 2009)





## Chapter 2

# Experimental motivation

We start out by giving a short introduction to the field of nanofluidics. Secondly, we move on to the point of departure for the current thesis; experimental observations of electrokinetic phenomena around an un-biased electrode in a microfluidic channel. The initial observations are credited to professor Sumita Pennathur from the UCSB–Nanolab. This data is acquired using optical epifluorescence microscopy which is such a refined technique that it needs an introduction and the second part of this chapter is therefore devoted to a presentation hereof. The information in this part is mainly from [4].

Unfortunately, the initial experimental observations were made in a setup too complex to allow for a simple theoretical analysis. Consequently, these observations play little role in the current work and will therefore only be briefly covered despite that a considerable work effort was put into an analysis of it. Instead, more emphasis will be put on the second generation experiments carried out by the author during a visit to the UCSB–Nanolab.

Finally, the last part of this chapter presents some of the general experimental observations in microfluidic electrokinetics that are still not understood.

### 2.1 Nanofluidics

Nanofluidics is experiencing the same boom in research as microfluidics did in the beginning of the 1990s. The surface-to-volume ratio is high in nanochannels, resulting in surface-charged-governed transport, which allows ion separation and is described by a comprehensive electrokinetic theory. The charge selectivity is most pronounced if the Debye screening length  $\lambda_D$  is comparable to the smallest dimension of the nanochannel cross section [5]. In a KCl electrolyte with typical concentrations of 1 mM and 0.1 mM the Debye screening length is  $\lambda_D \approx 10$  nm and  $\lambda_D \approx 30$  nm, respectively.

Fabrication of nanochannels is becoming increasingly accessible; Persson *et al.* [6] demonstrate a planar fabrication technique for producing nanochannels with heights from 14 – 300 nm. Thamdrup *et al.* [7] investigated the filling speed in SiO<sub>2</sub> nanoslits with heights ranging from 33 – 158 nm and found an increase in bubble formation in nanoslits with heights below 100 nm that increases the fluidic resistance.

Pennathur *et al.* [8, 9] present several points; (*i*) a theoretical model demonstrating that

the effective mobility governing electrophoretic transport of charged species in nanochannels depends not only on electrolyte mobility values but also on the  $\zeta$ -potential, ion valence, and background electrolyte concentration. (ii) An experimental study of nanoscale electrokinetic transport in custom-fabricated quartz nanochannels using quantitative epifluorescence imaging and current monitoring techniques. Their results confirm the usefulness of continuum theory in predicting electrokinetic transport and electrophoretic separations in nanochannels and show that the effective mobility governing electrophoretic transport of charged species in nanochannels depends not only on ion mobility values but also on the shape of the electric double layer and analyte ion valence. Part of the current work is a continuation of the research in nanochannel electrokinetic transport phenomena. The next section describe the important concept of fluorescence microscopy.

## 2.2 Fluorescence microscopy

The experimental data is acquired optically using fluorescently marked electrolytes and an inverted fluorescence microscope. Fluorescence is the process of absorption and re-radiation of light. The emission of light in a fluorescence process is almost simultaneous with the absorption of the excitation light since the delay between photon absorption and emission is on the order of  $10^{-9}$ – $10^{-7}$  s [10]. If the emission persists longer after excitation the process is called phosphorescence.

The technique of fluorescence microscopy is an essential tool in biology, biomedical science and materials science, among other reasons because it is possible to detect single molecules by use of fluorophores (also referred to as fluorochromes or dyes). Fluorophores are stains that attach themselves to visible or sub-visible structures, are very specific in their attachment targeting, and have a significant quantum yield (the ratio of photon absorption to emission). It is hereby possible to identify targets with a high degree of specificity among non-fluorescence materials.

The basic function of fluorescence microscopy is to irradiate a specimen with a desired and specific band of wavelengths and then to separate out the much weaker emitted fluorescence from the excitation light. In a properly configured setup, only the emission light should reach the eye or detector so that the fluorescence signal is contrasted against a very dark background. Typically, the detection limit is governed by the darkness of the background, and the excitation light is usually from a hundred thousand to a million times brighter than the emitted fluorescence.

The principle behind the change in wavelength between the excitation and emission light is called Stokes law or Stokes shift, see Figure 2.1 (a). The physical explanation is that vibrational energy is lost when electrons relax from the excited state back to the ground state. It is due to this energy loss that the emission spectrum of an excited fluorophore is shifted to longer wavelengths compared to the absorption spectrum. The greater the Stokes shift, the easier it is to separate excitation from emission light by use of filters. Consequently, the emission intensity peak value is usually larger in wavelength and lower in magnitude than that of the excitation peak, and the emission spectral profile is often close to a mirror-image of the excitation curve, but it is shifted to longer wavelengths,

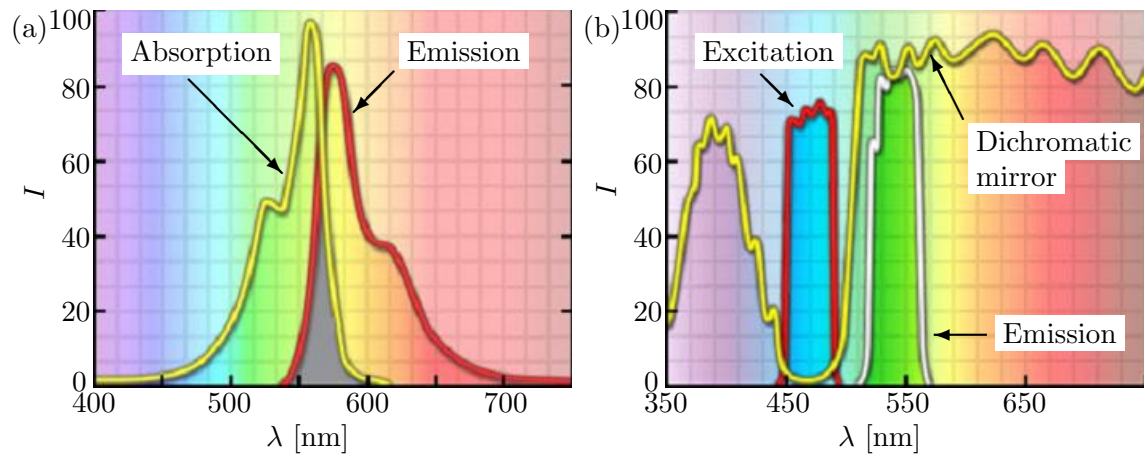


**Figure 2.1:** (a) Absorption (yellow) and emission (red) spectral profiles for a fluorescence dye [4]. (b) Example of transmission profiles for excitation filter (red), dichromatic mirror (yellow), and emission filter (white) [4].

see Figure 2.1 (a). Therefore, in order to achieve maximum benefit from fluorescence microscopy, the dye has to be excited at wavelengths near the peak of the excitation curve and the widest possible range of emission wavelengths that include the emission peak are selected for detection.

Light of a specific wavelength is produced by passing multispectral light from an arc-discharge lamp through a wavelength selective excitation filter. The wavelengths that pass through the excitation filter are reflected from the surface of a dichromatic mirror (also called a beamsplitter) through the microscope objective to bath the specimen with intense light. If the specimen fluoresces the emission light passes back through objective and the dichromatic mirror and is filtered by an emission filter that blocks the unwanted excitation wavelengths, see Figure 2.1 (b).

This technique, called epifluorescence illumination, is especially advantageous and is used in the current work. It is important to note that in epifluorescence illumination the excitation light is passed through the objective and onto the specimen and subsequently the same objective is used to gather the emitted light. Hence, three main advantages in this technique are (i) the microscope objective serves first as a well-corrected optical condenser and secondly as the image-forming light gatherer. Because these two functions are integrated into one unit, the condenser/gatherer is always in perfect alignment. (ii) A majority of the excitation light reaching the specimen passes through it without interaction and travels away from the objective, thereby not contributing with disturbing background light. (iii) The illuminated area is restricted to that which is seen through the eyepieces, which reduces the overall amount of fading (the reduction of fluorescence emission due to "wear"). A point to note is that the emitted light radiates spherically in all directions, regardless of the excitation light source.

## 2.3 Experimental procedure

In the current work we use an inverted epifluorescence microscopy setup shown in Figure 2.2 (a). A mercury arc-discharge lamp functions as light source and shines light horizontally into a filter cube as shown in Figure 2.2 (b). As the light enters the cube it passes an excitation filter that only allows passage of a desired band of wavelengths, see Figure 2.1 (b). The light then continues to the dichromatic beam splitting mirror which effectively reflects shorter wavelength light and efficiently passes longer wavelength light, see Figure 2.1 (b). The dichromatic beamsplitter is tilted  $45^\circ$  with respect to the incoming excitation light and reflects this illumination at a  $90^\circ$  angle directly through the objective and onto the microchip.

The microchip contains fluorophores and some of the re-emitted, longer wavelength fluorescence light is guided by the objective down through the dichromatic beamsplitter, where it passes without reflection. A final filtering is done by the emission filter to make sure only emission light passes, see Figure 2.1 (b). The light is guided into a digital CCD camera, where it is stored as digital images on a computer. The digital images, often in tiff format, are post-processed in MATLAB where background signals are removed and uneven lighting compensated.

The next sections describe in turn the microsystem, the buffers, the fluorescence dyes, and finally the post-processing and the experimental observations in the current work.

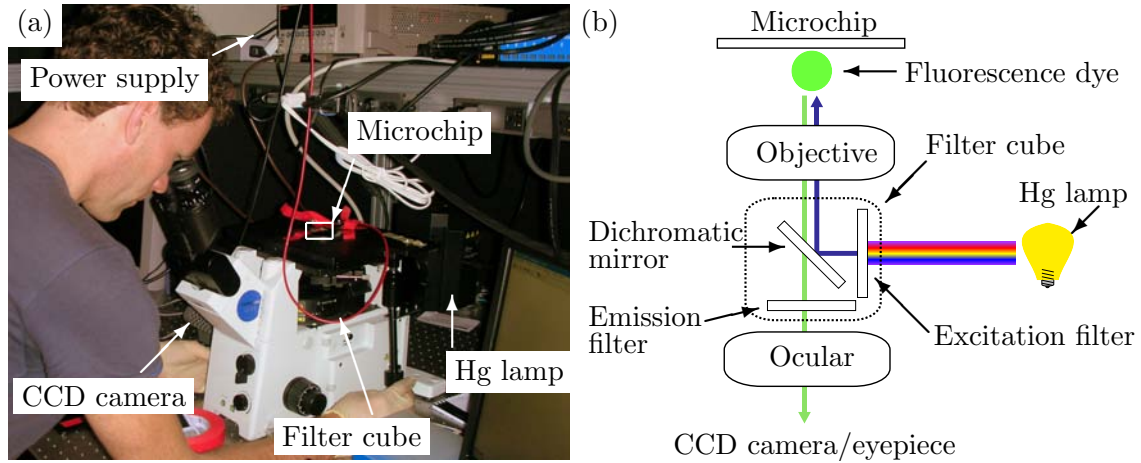


**Figure 2.2:** (a) Picture of the experimental setup in the UCSB-Nanolab. The main experimental components are the microchip, the mercury lamp (Hg lamp), the filter cube, the CCD camera, and the power supply. (b) Schematic of the epifluorescence experimental setup; a Hg lamp shines multispectral light through an excitation filter that only allows a certain band to pass. The dichromatic mirror reflects the excitation light up through an objective where it hits the microchannel and the fluorescence dye. Some of the emission light from the dye is gathered by the objective and guided downwards where it passes through the dichromatic mirror and the emission filter that filters away all light except the emission light. Finally, the emission light is directed through an ocular and into a CCD camera or an eyepiece.

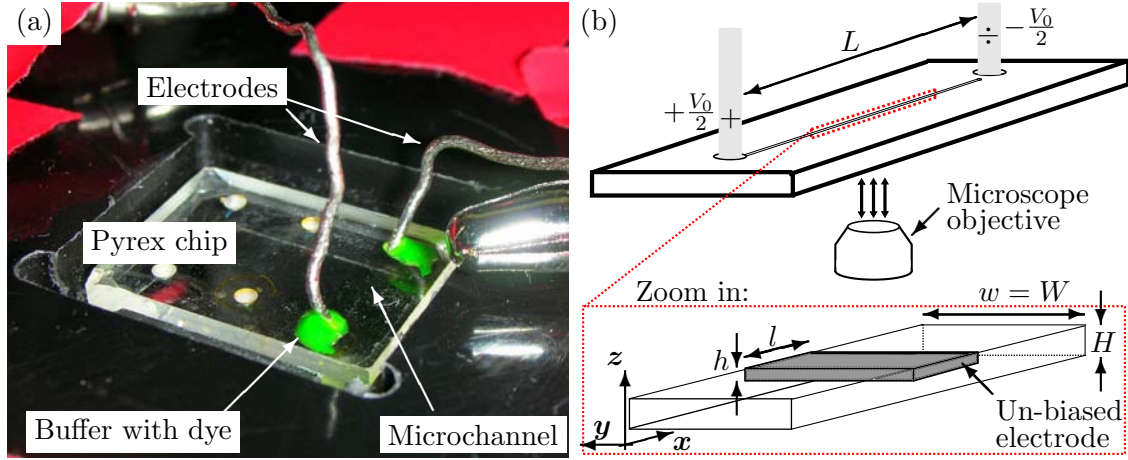


**Figure 2.3:** (a) Picture of a microchip containing three parallel microchannels; the channel to the right has been filled with a buffer containing fluorescence dye (green) and electrodes have been submerged into the inlets. Also, the picture is a close up on the microchip-holder that sits right above the microscope objective. (b) Sketch of the microchannel showing the distance between the inlets  $L = 9$  mm, the widths of the channel and metal  $W = w = 250$   $\mu\text{m}$ , respectively, the height of the channel  $H = 0.5$   $\mu\text{m}$ , the height of the metal  $h = 0.1$   $\mu\text{m}$ , and the length of the metal  $l = 60$   $\mu\text{m}$ .

## 2.4 The microfluidic chip

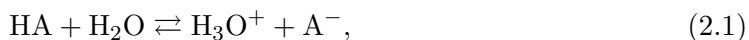
The microchip is fabricated in pyrex, a transparent borosilicate glass, to allow passage of light, see Figure 2.3 (a). It contains straight microchannels of length  $L \approx 9$  mm, with rectangular cross sections of width  $W \approx 250$   $\mu\text{m}$  and height  $H \approx 0.5$   $\mu\text{m}$ , see Figure 2.3 (a) and (b). Also, the microchannels have cylindrical inlets at both ends of the channel, entering from the top side of the chip, and with a diameter around 1 mm; the inlets represent reservoirs as they hold a relatively large volume of fluid. Inside the channel at the midpoint between the inlets a small amount of metal (referred to as un-biased electrode), either gold or platinum, is deposited in different planar geometries with heights around 0.1  $\mu\text{m}$  and a typical extent in the two other dimensions of around 100  $\mu\text{m}$ , see Figure 2.3 (b). The microchannels are filled with different types of aqueous buffer solutions containing small concentrations of different fluorescence tracker dyes.

Electrodes of platinum wire are submerged into the inlets and during the course of the experiment, typically 30 s, a voltage difference  $V_0$  from 50 V to 300 V is applied, see Figure 2.3. The applied voltage produces an EO-flow throughout the channel, but at the same time also ICEO in the vicinity of the metal structure. Thus, the fluorescence dyes will interact with the hydrodynamic flow and electric field in the channel and around the metal, thereby creating regions of high and low concentration which can be observed; it is exactly this interaction that we try to explain. The next section describes the essentials of buffer theory plus a more detailed description of the specific buffer used in the current work.

## 2.5 Buffers

During the experiments we used phosphate and borate buffers, but we only use results relating to the phosphate buffer when we compare with numerical simulations. Hence, we only present the phosphate buffer in this chapter and refer the reader to Appendix A for information about the borate buffer. The phosphate buffer is in reality a weak acid; a concept that is important to understand and thus is described below.

When a weak acid HA is mixed with water H<sub>2</sub>O a fraction of it dissociates into hydrogen ions H<sup>+</sup> and conjugate base ions A<sup>-</sup>. The dissociated hydrogen ions combine with water molecules to create hydronium ions H<sub>3</sub>O<sup>+</sup> and the overall reaction is



a process that reaches a dynamic equilibrium where the forward and backward rates of conversion are equal. This dynamic equilibrium can be described by a thermodynamic equilibrium constant  $K^\ominus$  which may be defined in terms of the activities  $\{X_i\}$  of the four species  $X_i$ ,  $i = 1 \dots 4$  given in Equation (2.1)

$$K^\ominus = \frac{\{\text{H}_3\text{O}^+\}\{\text{A}^-\}}{\{\text{HA}\}\{\text{H}_2\text{O}\}}. \quad (2.2)$$

The activity of a species  $X_i$  can be expressed as the product of its concentration  $[X_i]$  with its activity coefficient  $\gamma_i$  and the expression for the thermodynamic equilibrium constant becomes

$$K^\ominus = \frac{[\text{H}_3\text{O}^+][\text{A}^-]}{[\text{HA}][\text{H}_2\text{O}]} \frac{\gamma_{\text{H}_3\text{O}^+}\gamma_{\text{A}^-}}{\gamma_{\text{HA}}\gamma_{\text{H}_2\text{O}}}. \quad (2.3)$$

For simplicity the quotient of activities can be assumed to be constant, and likewise for the concentration of water which in aqueous solutions is invariant at a value around  $[\text{H}_2\text{O}] = 55 \text{ M}$ . Thus, if these two constant factors are incorporated into the thermodynamic equilibrium constant the result is the acid dissociation constant  $K_a$

$$K_a = \frac{[\text{H}_3\text{O}^+][\text{A}^-]}{[\text{HA}]}, \quad (2.4)$$

for which precaution has to be exercised since the concentrations in this expression usually are given in units of mol L<sup>-1</sup> [11]. However, the unit of  $K_a$  is left out when the cologarithm<sup>1</sup> is applied to it, leading to another definition of the acid dissociation constant called  $\text{p}K_a$

$$\text{p}K_a = -\log_{10}(K_a), \quad (2.5)$$

which is convenient to work with since  $K_a$  can vary many orders of magnitude. Additionally, pH is defined as the cologarithm of the concentration (in mol L<sup>-1</sup>) of hydronium ions

$$\text{pH} = -\log_{10}([\text{H}_3\text{O}^+]). \quad (2.6)$$

---

<sup>1</sup>The cologarithm to  $x$  is the negative of the logarithm to  $x$ ;  $\text{colog} x = -\log x$

For the numerical simulations it is important to know the amount of charged species. Therefore, the concentrations of hydronium  $[\text{H}_3\text{O}^+]$  and conjugate base  $[\text{A}^-]$  have to be calculated. First, note that the concentrations of the two are equal and have a constant value denoted by  $\Delta c$

$$\Delta c = [\text{H}_3\text{O}^+] = [\text{A}^-]. \quad (2.7)$$

The concentration of the weak acid before dissociation is denoted  $c_0$ , and consequently there will be an amount

$$[\text{HA}] = c_0 - \Delta c \quad (2.8)$$

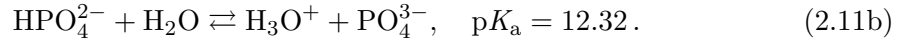
at the dynamic equilibrium. The expressions for the concentrations of hydronium, conjugate base, and weak acid are inserted into Equation (2.4) and a quadratic equation in  $\Delta c$  appears

$$\Delta c^2 - K_a c_0 \left(1 - \frac{\Delta c}{c_0}\right) = 0, \quad (2.9)$$

Furthermore, if the degree of dissociation  $\Delta c$  is small compared to the initial concentration of the weak acid  $\Delta c/c_0 \ll 1$  it follows from Equation (2.9) that

$$\Delta c \approx \sqrt{K_a c_0}. \quad (2.10)$$

The phosphate buffer used in the current work is an aqueous solution of disodium phosphate  $\text{Na}_2\text{HPO}_4$  that forms four charged species when it dissociates in water; sodium  $\text{Na}^+$ , hydrogen phosphate  $\text{HPO}_4^{2-}$ , hydronium  $\text{H}_3\text{O}^+$ , and phosphate  $\text{PO}_4^{3-}$ , through the two reaction steps



The first reaction step Equation (2.11a) is not a dynamic equilibrium since this corresponds to the dissolution of a salt in water. The solubility of disodium phosphate in water is around 500 mM [12], and hence it dissolves completely for the concentrations of 1 mM and 10 mM used here. The second reaction step Equation (2.11b) is a dynamic equilibrium and the acid dissociation constant at 25 °C is listed to the right [13].

As already mentioned, numerical computations need as input parameters the concentrations of charged species. We therefore need to estimate the amount of charged species in the buffer solution given by Equations (2.11). First, the concentrations of sodium  $[\text{Na}^+]$  and hydrogen phosphate  $[\text{HPO}_4^{2-}]$  are related to the initial concentration of disodium phosphate  $[\text{Na}_2\text{HPO}_4]$  by

$$[\text{HPO}_4^{2-}] = [\text{Na}_2\text{HPO}_4], \quad (2.12a)$$

$$[\text{Na}^+] = 2[\text{Na}_2\text{HPO}_4]. \quad (2.12b)$$

Thus, since the  $\text{p}K_a$  of Equation (2.11b) is relatively large, Equation (2.10) is a good approximation from which the concentrations of hydronium and phosphate are calculated. For the experimentally used concentrations of disodium phosphate of 1 mM and 10 mM, all concentrations of charged species are listed in Table 2.1. It is noted that in order to make

**Table 2.1:** The concentrations of charged species ( $[\text{Na}^+]$ ,  $[\text{HPO}_4^{2-}]$ ,  $[\text{H}_3\text{O}^+]$ , and  $[\text{PO}_4^{3-}]$ ) for the two concentrations 1 mM (low) and 10 mM (high) of disodium phosphate ( $[\text{Na}_2\text{HPO}_4]$ ) in the phosphate buffers used in the experiments.

Symbol	Low	High	Symbol	Low	High
$[\text{Na}^+]$	2 mM	20 mM	$[\text{H}_3\text{O}^+]$	21.88 nM	69.18 nM
$[\text{HPO}_4^{2-}]$	1 mM	10 mM	$[\text{PO}_4^{3-}]$	21.88 nM	69.18 nM

**Table 2.2:** Concentrations of charged species ( $[\text{Na}^+]$  and  $[\text{B}^-]$ ) for the two concentrations 1  $\mu\text{M}$  (low) and 10  $\mu\text{M}$  (high) of BODIPY used in the experiments.

Symbol	Low	High
$[\text{Na}^+]$	1 $\mu\text{M}$	10 $\mu\text{M}$
$[\text{B}^-]$	1 $\mu\text{M}$	10 $\mu\text{M}$

the numerical computations simple, a reasonable approximation is to leave out hydronium  $\text{H}_3\text{O}^+$  and phosphate  $\text{PO}_4^{3-}$ , since these appear in very low concentrations relative to the concentrations of sodium  $\text{Na}^+$  and hydrogen phosphate  $\text{HPO}_4^{2-}$ .

## 2.6 Fluorescence dye

We used both BODIPY and fluorescein dyes in the experiments, but we only include results that relate to the BODIPY dye. Thus, only BODIPY is introduced in this section and we refer the reader to Appendix A for information about fluorescein.

BODIPY, short for boron-dipyrromethane, is a class of fluorescence dyes which is characterized by (i) a very small Stokes shift, (ii) high, pH-independent quantum yield that is close to 100%, and (iii) sharp excitation and emission peaks, see Figure 2.4 (b) [14]. The particular BODIPY fluorophore we use in the current work is the sodium salt  $\text{C}_{20}\text{H}_{14}\text{BF}_6\text{N}_2\text{NaO}_5\text{S}$  (denoted by BNa) which we assume to dissociate completely in an aqueous buffer through the reaction



and thus the concentrations of charged BODIPY  $[\text{B}^-]$  and sodium  $[\text{Na}^+]$  are equal to the initial concentrations of BODIPY  $[\text{BNa}]$

$$[\text{B}^-] = [\text{Na}^+] = [\text{BNa}], \quad (2.14)$$

in our case 1  $\mu\text{M}$  and 10  $\mu\text{M}$ , as listed in Table 2.2. The molecular structure of the BODIPY molecule is shown in Figure 2.4 (a). The next section presents selected parts of the experimental data.



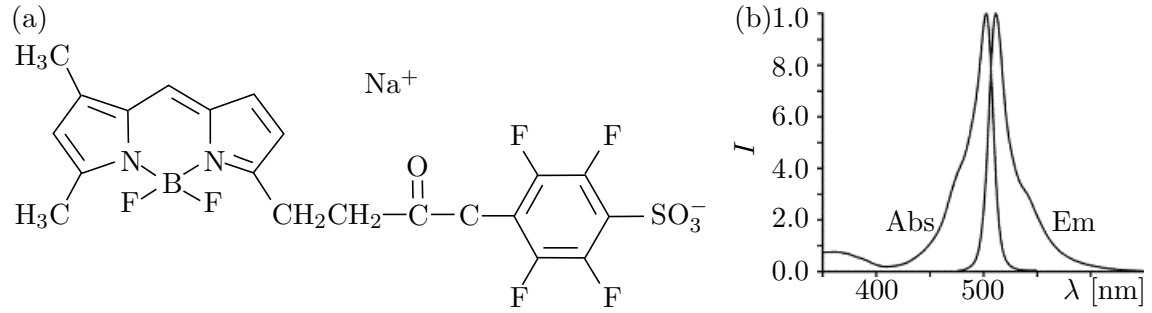


**Figure 2.4:** (a) BODIPY molecule with a negatively charged sulfur oxide group  $\text{SO}_3^-$  and a dissociated, positively charged sodium atom  $\text{Na}^+$  [15]. (b) Spectral profile of the BODIPY dye used in the current work, showing the intensity  $I$  curves of absorption Abs and emission Em as function of light wavelength  $\lambda$ , each normalized against its maximum value [16]. Note the sharp absorption and emission peaks at 504 nm and 513 nm, respectively, which shows the small Stokes shift.

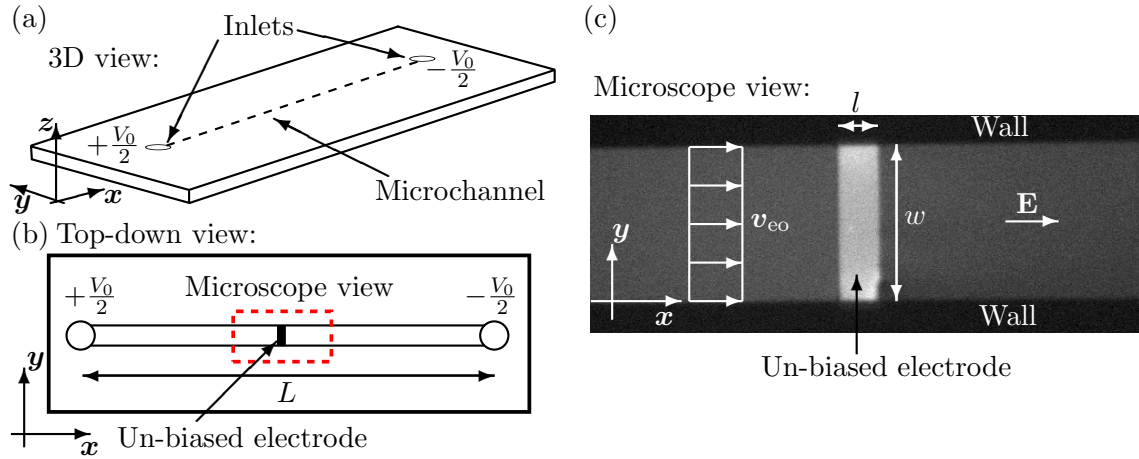


**Figure 2.5:** (a) Schematic of the microchip where the red, dashed box shows the microscopic view (not to scale) that the CCD camera records. (b) Example of a raw data image showing the position of the rectangular, un-biased spanning the microchannel from wall to wall. Also, the electric field is indicated along with an EO-flow. The image is in gray-scale; each pixel has a value that corresponds to the recorded light intensity.

## 2.7 Post-processing and experimental observations

The experimental data consists of digital image files which have to be post-processed before any quantitative analysis and comparison to numerical simulations can be realized, see Figure 2.5. The raw images  $I_{\text{raw}} = I_{\text{raw}}(x, y, t)$  are post-processed in MATLAB with the main purpose to make corrected image data  $I_{\text{corr}} = I_{\text{corr}}(x, y, t)$ . This is done by subtracting a background image  $I_{\text{background}} = I_{\text{background}}(x, y)$  and by normalizing against the difference between a flat field image  $I_{\text{flatfield}} = I_{\text{flatfield}}(x, y)$  and the background image

[17]. Thus, each image is subjected to the following matrix operation

$$I_{\text{corr}} = \frac{I_{\text{raw}} - I_{\text{background}}}{I_{\text{flatfield}} - I_{\text{background}}}. \quad (2.15)$$

The background image is obtained by acquiring a frame of the microchannel without fluorescence dye; when subtracting this from the raw data, any signal not stemming from the dye, is removed. The flatfield image is a frame of the microchannel with a homogeneous concentration of dye. Moreover, to remove any lack of uniformity in the illumination from the arc-discharge lamp, the data is normalized against the flatfield; however, the flatfield itself also has to be corrected for background faults. The non-uniformity stems from the arc-discharge lamp and its arrangement within several reflecting mirrors.

Note, it is a tedious procedure to correct the raw images since the alignment between  $I_{\text{raw}}$ ,  $I_{\text{background}}$ , and  $I_{\text{flatfield}}$  might be more or less offset relative to each other. This offset is due to the slight change in position of the microchip when it is un- and remounted during the experiments. This displacement has to be identified for each individual set of data, a process that is difficult and hard to automatize.

The next two sections introduce two experimentally observed phenomena (i) a concentration drop across a rectangular metal shape, as seen in Figure 2.5 (b), and this is a main focus of the current work. (ii) Diffusion of the fluorescence dye BODIPY and determination of its diffusion constant in 2D. This is not a main focus of the current work.

### 2.7.1 Concentration drop across a rectangular un-biased electrode

By inspiration of similar work [18], we have observed a concentration drop across a rectangular un-biased electrode spanning the width of the microchannel when a DC voltage is applied between the inlets, see Figure 2.6 (a).

In order to compare the experimental data to numerical simulations, the intensity in the corrected images is averaged across the width of the channel  $w$  in the transverse direction  $y$  to get an intensity  $I_x = I_x(x, t)$  that is a function of the axial coordinate  $x$  and time  $t$  only

$$I_x(x, t) = \frac{1}{w} \int_0^w I_{\text{corr}}(x, y, t) dy, \quad (2.16)$$

of which an example is shown in Figure 2.6 (b). The geometry of the deposited metal comes in many different shapes, but the rectangular shape gives the best possibility for comparison to numerical simulations. This is because the numerical simulations are done in the 2D cross-sectional  $xz$ -plane; the rectangular shapes have the highest degree of translational invariance along the transverse direction  $y$  that is consistent with this 2D description.

The concentration drop is investigated as a function of three parameters (i) applied voltage difference, (ii) buffer concentration, and (iii) dye concentration. Figure 2.7 (a) and (b) show combined spatial and temporal plots of  $I_x$  for two applied voltages  $V_0 = \{50 \text{ V}, 100 \text{ V}\}$ . The data contains the transients at the turn on and off of the applied voltage at  $t \approx 0 \text{ s}$  and  $t \approx 25 \text{ s}$ , respectively. However, we focus on steady-state in the

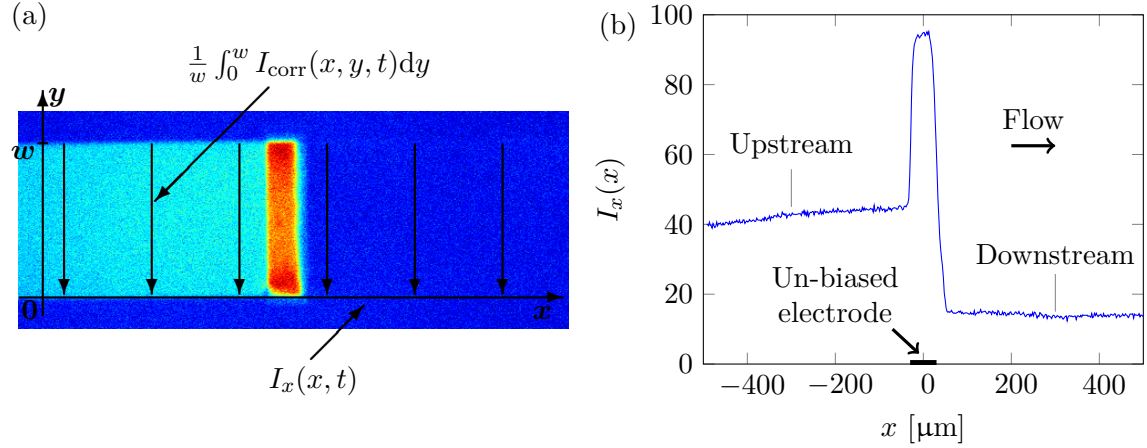


**Figure 2.6:** (a) Example of an image of the corrected intensity  $I_{\text{corr}}$ . The arrows indicate how the average is taken in the transverse direction to produce  $I_x$ . Note, the section to the left of the un-biased metal electrode is lighter due to a higher intensity compared to the section to the right. (b) Example of a plot of  $I_x$  in a steady-state situation. The position of the un-biased electrode is at  $x = 0$ . The peak in  $I_x$  shows a high intensity on the electrode which might be due to a concentration enhancement of dye in the induced electrical double layer.

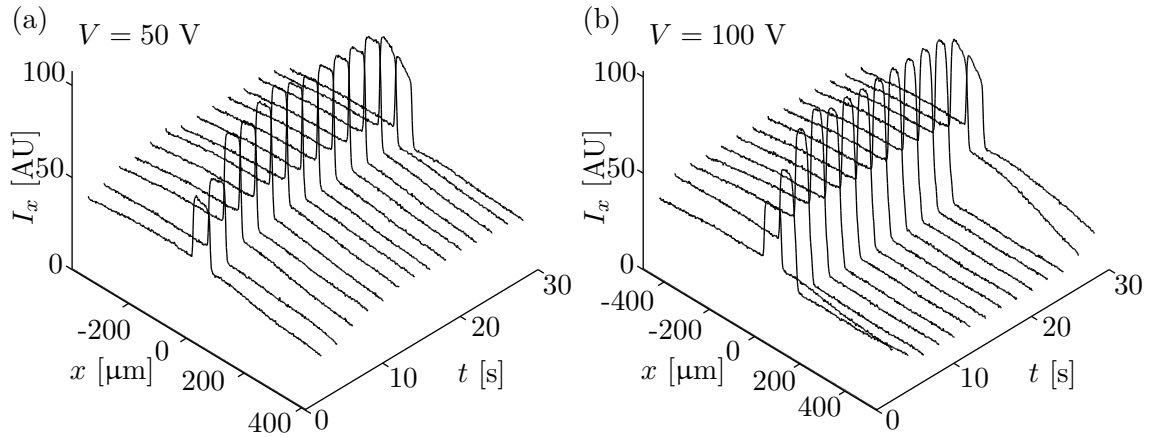


**Figure 2.7:** Plots of spatial and temporal evolution of the averaged intensity  $I_x$ . The buffer is phosphate, the fluorescence dye is BODIPY, and the applied potential difference is in (a) 50 V, and in (b) 100 V. Note, in each plot there is a short transient immediately after the voltage difference is applied  $t \approx 0$  s (barely visible in these graphs) where  $I_x$  goes from zero to a step-like function across the un-biased electrode. The height of this step is greater for 100 V than for 50 V. Finally, the voltage difference is turned off and another short transient (diffusive process) is just visible at the final times  $t \approx 25$  s–30 s.

current work and use a particular frame as a representation. Typically, we assume steady-state at  $t \approx 20$  s where the temporal change in the data is seen to be very small. In the next section we determine the diffusion constant of BODIPY.

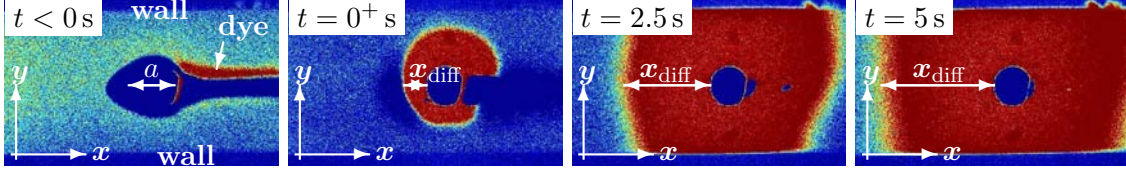


**Figure 2.8:** Selected frames from the electrokinetic experiment showing a bottom view (the  $xy$ -plane) of the microchannel of height  $0.5\ \mu\text{m}$  ( $z$ -direction) in the region around a metal cylinder (circular object) with diameter of  $a = 60\ \mu\text{m}$  and height  $0.1\ \mu\text{m}$ . The frames show the temporal evolution of the corrected intensity  $I_{\text{corr}}$ , going from low (blue) to high (red), in a borate buffer with a concentration of  $1\ \text{mM}$  containing BODIPY dye with a concentration of  $100\ \mu\text{M}$ . Contrary to the rectangular shape, the metal cylinder sits on the bottom wall and blocks the view to the dye above it, hence no signal is received from that area and the contour of the cylinder is dark blue. In the first frame  $t < 0$  the applied voltage is  $800\ \text{V}$  over the channel length of  $9\ \text{mm}$  (corresponding to  $5.3\ \text{V}$  across the cylinder); at  $t = 0^+$  the voltage is turned off and diffusion of a large concentration of dye with a front at a distance  $x_{\text{diff}}$  from the metal cylinder is seen at subsequent times.

### 2.7.2 Diffusion of BODIPY

An example of a relatively simple phenomenon in this otherwise complex framework is that of diffusion of the dye, see Figure 2.8. This is not a main focus of the current work but is included, since it helps determining the diffusion constant of BODIPY, which is otherwise difficult to find in the literature. The sequence of movie frames show when an externally applied DC electric field between the microchannel inlets is turned off, a big concentration of dye diffuses away from the metal object.

The movie is analyzed by following the front of the dye as a function of time; the square of the distance from the front to the metal cylinder  $x_{\text{diff}}^2$  is directly proportional to time with the constant of proportionality being six times (in 3D) the diffusion constant  $D$  [3]

$$x_{\text{diff}}^2 = 6Dt. \quad (2.17)$$

The square of the diffusion length  $x_{\text{diff}}^2$  is plotted against time  $t$  in Figure 2.9. The experimental data is fitted to a straight line which gives the regression

$$x_{\text{diff}}^2 = (3.5 \times 10^{-9} \text{ m}^2\text{s}^{-1}) t \Rightarrow \quad (2.18a)$$

$$D = 5.8 \times 10^{-10} \text{ m}^2\text{s}^{-1}. \quad (2.18b)$$

Sugar is comparable to BODIPY with regards to size and structure, and since our experimentally determined diffusion constant is close to the diffusion constant of sugar in water  $D_{\text{sugar}} \approx 5 \times 10^{-10} \text{ m}^2\text{s}^{-1}$  [3], we conclude that it is reasonable. Additionally, the experiment confirms that a large concentration of dye is contained in the Debye layer on the metal electrode. This concludes the experimental observation on the diffusion of BODIPY and also the general observation of the concentration drop. The next section introduces two unexplained electrokinetic phenomena found in the literature.

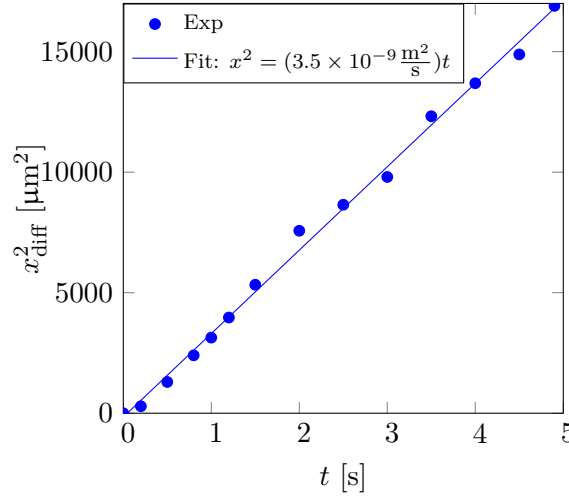


**Figure 2.9:** Plot of the square of the diffusion length  $x_{\text{diff}}^2$  (in  $\mu\text{m}^2$ ) of the dye front in Figures 2.8 against time  $t$ . The experimental data (Exp) are fitted to a line (Fit) which has a slope of  $3.5 \times 10^{-9} \text{ m}^2\text{s}^{-1}$ , and consequently the diffusion constant of BODIPY (in 2D) is found to be  $5.8 \times 10^{-10} \text{ m}^2\text{s}^{-1}$ .

## 2.8 Unexplained electrokinetic phenomena

To this day there are still fundamental aspects of electrokinetic theory that remain unexplained. As a consequence, some experimental observations lack reasonable theoretical explanations.

One of the applications of electrokinetics in microfluidics is as a pumping mechanism where a class of devices are named AC electrokinetic micropumps. To achieve pumping in AC electrokinetic micropumps an asymmetric array of interdigitated electrodes are deposited on the wall of a microchannel. The microchannel is filled with an electrolyte e.g. water and KCl and a time varying AC field is applied to each pair of electrodes in the array. Due to the asymmetry of the electrode array and the nature of the time varying electric field a net DC flow is generated in the channel. The strength and direction of the DC component of the flow is dependent on the strength and frequency of the applied AC field and it is in this dependence that experiment and theory deviates. Among a lot of experimental evidence, work done in the DTU-TMF group shows that for low applied voltages  $V_{\text{rms}} < 1.5 \text{ V}$  and low frequencies  $f < 20 \text{ kHz}$  the pumping direction reverses [19]. The reversal of the pumping direction in the AC electrokinetic micropump is qualitatively reproduced by a theoretical model [20], but with rather large quantitative discrepancies. Also, the experimental observations clearly show a dependence on the concentration of the electrolyte which is not present in the theoretical model.

Another example of an unexplained experimental observation is that of ICEO flow. In the experiment a planar unbiased electrode is deposited on a wall in a microchamber. The microchamber is filled with a KCl electrolyte and an external electric field is applied tangential to the surface of the electrode producing ICEO flow in the electrolyte. Due to

nonlinear effects the measured velocity of the ICEO is much smaller than those predicted by linear theory. Even if nonlinear effects are taken into account theory still overestimates the induced flow velocities [21]. These two examples of experimental and theoretical differences demonstrate the need for continued research in the area of nonlinear electrokinetic effects.

## Chapter 3

# Electrokinetic theory

In this chapter we introduce three electrokinetic models; the full nonlinear, the linear slip-velocity, and the nonlinear slip-velocity model. These models are the tools used in the numerical simulations in this thesis and they each represent different levels of approximation and ease of numerical execution.

### 3.1 Basic physical picture

The main concern in the current thesis is the description of an electrolyte under an external voltage bias and its interaction with a charged surface; the charged surface stems from an intrinsic surface charge or from induced charge around a conducting surface.

An understanding of the microscopic picture is helpful in this context and to this purpose Figure 3.1 shows the Gouy–Chapman–Stern model of a binary, symmetric electrolyte at the interface of a charged surface. The figure is a snap shot of e.g. an aqueous solution of potassium chloride (KCl) next to poly-methyl methacrylate (PMMA), both common components in the world of electrokinetics.

One of the most significant effects of the charged surface is attraction of ions with opposite sign of charge (counter-ions) and repulsion of ions with similar sign of charge (co-ions). At zero absolute temperature the counter-ions would screen the surface charge perfectly, but due to thermal fluctuations the screening is only partial.

A region close to the interface, where ions still have the ability to move around freely, is called the diffuse layer and is illustrated in Figure 3.1 (a). Note how emphasis is put on a pronounced majority of counter-ions in the diffuse layer. The different distributions of counter- and co-ions give rise to a non-zero electric charge density and with this a varying electric potential  $\phi$ . As sketched in Figure 3.1 (b) the potential drop between the interface and the bulk is called the  $\zeta$ -potential (also denoted zeta-potential). For low  $\zeta$  (linear regime) the decay is exponential and characterized by a length scale (Debye–Hückel screening length)  $\lambda_D$ , with typical values in the range 1 – 100 nm.

It is important to note some of the challenges in describing the picture above. The current thesis employs a smooth continuum description of the ionic species by introducing concentration fields; this is in some cases an over-simplification. First, Figure 3.1 (a) shows

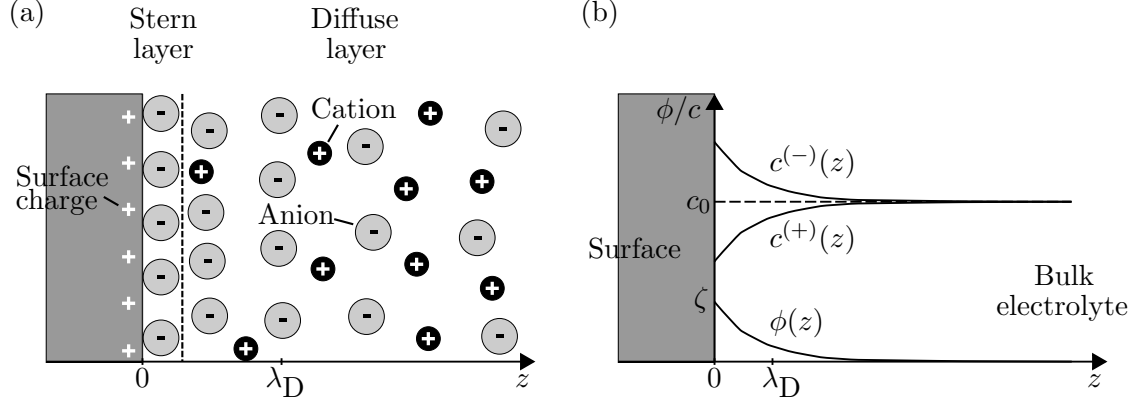


**Figure 3.1:** Interface region between a solid with a surface charge and a binary, symmetric electrolyte. (a) Microscopic view showing how the co-ions (same sign of charge as solid  $+$ ) and counter-ions (different sign of charge as solid  $-$ ) are distributed in two regions; a thin, immobile layer sitting directly on the solid, the Stern layer, and a broader region with a majority of mobile counter-ions, the diffuse layer. (b) Sketch of the electric potential  $\phi(z)$  (bottom graph), cation concentration field  $c^{(+)}(z)$  and anion concentration field  $c^{(-)}(z)$  (upper graphs). The electric potential has a value at the interface  $\zeta$  and for low values of  $\zeta$  the variation in the potential is exponential going from the interface into the bulk. This exponential decay has a characteristic length scale  $\lambda_D$  with typical values in the range  $1 - 100$  nm. In Debye-Hückel theory the exponential variation in electric potential is reflected in the distribution of the ions in the electrolyte such that these also decay exponentially toward an equilibrium bulk value  $c_0$ .

a very weak presence of co-ions in the diffuse layer; the use of a continuum description of the few co-ion molecules is questionable and simulations of individual molecules might be more appropriate. Second, there is a physical upper limit to the concentration of counter-ions in the diffuse layer; this limit is reached for high surface charge, also called the nonlinear regime, where the distance between counter-ion molecules equals their diameter. In this situation the molecules start to pack in a condensed structure and the concentration reaches a maximum [22]; the continuum description in its simplest form is unable to capture this phenomenon.

In direct connection with the problem at large surface charge is the description of immobile molecules in the region between the interface and the diffuse layer, called the Stern layer. In the linear regime the Stern layer is only one (and at most a few) atomic layers thick. A simple approximation is to model it as a slab of dielectric material but for simplicity we omit it in the current work. In the next section we introduce the three different electrokinetic models used in the current work.

### 3.2 Full nonlinear model

Different models are employed to describe electrokinetic phenomena. In the current work focus is on three models (full nonlinear, linear slip-, and nonlinear slip-velocity) which



utilizes different assumptions and thus are more or less complex. The models build on a similar framework, which the full nonlinear model gives a good intuitive feeling of; hence, this model is described first, where after the details of the remaining two are accounted for.

### 3.2.1 Continuity equation

Conservation of mass is enforced by the continuity equation [3]

$$\partial_t \rho_b + \nabla \cdot (\rho_b \mathbf{v}) = 0, \quad (3.1)$$

where  $\rho_b = \rho_b(\mathbf{r}, t)$  is the mass density of the electrolyte buffer and  $\mathbf{v} = \mathbf{v}(\mathbf{r}, t)$  is the velocity field.

We assume incompressibility of the fluid since our systems are without shock waves or fast pressure oscillations. Basically, this means that the speed of the fluid  $v$  has to be much smaller than the speed of sound in the fluid  $c_a$

$$v \ll c_a, \quad (3.2)$$

or that any pressure oscillation with angular frequency  $\omega_a$  in the confined space of length  $l$  fulfills the requirement

$$\omega_a l \ll c_a. \quad (3.3)$$

Under these conditions Equation (3.1) reduces to

$$\nabla \cdot \mathbf{v} = 0. \quad (3.4)$$

### 3.2.2 Momentum conservation

Momentum flow is governed by Navier–Stokes equations [3]

$$\rho_b [\partial_t \mathbf{v} + (\mathbf{v} \cdot \nabla) \mathbf{v}] = -\nabla p_{\text{dyn}} + \eta \nabla^2 \mathbf{v} - \rho_b \nabla \Phi + \beta \eta \nabla (\nabla \cdot \mathbf{v}) + \rho_{\text{el}} \mathbf{E} - k_B T \nabla c, \quad (3.5)$$

where  $p_{\text{dyn}} = p_{\text{dyn}}(\mathbf{r}, t)$  is the hydrodynamical pressure,  $\eta$  is the dynamic viscosity,  $\Phi$  is the gravitational potential,  $\beta$  is a dimensionless viscosity ratio,  $\rho_{\text{el}} = \rho_{\text{el}}(\mathbf{r}, t)$  is the electric charge density,  $\mathbf{E} = \mathbf{E}(\mathbf{r}, t)$  is the electric field,  $k_B$  is Boltzmann constant,  $T$  the temperature, and

$$c = c(\mathbf{r}, t) = \sum_i [c^{(i)}(\mathbf{r}, t) - c_0^{(i)}] \quad (3.6)$$

is the sum over the ionic concentration deviations from their equilibrium values  $c_0^{(i)}$ . We define the hydrostatic  $p_{\text{hs}}$  and the osmotic  $p_{\text{os}}$  pressures as

$$p_{\text{hs}} = \rho_b \Phi, \quad (3.7a)$$

$$p_{\text{os}} = k_B T c. \quad (3.7b)$$

Furthermore, we define the total pressure  $p$  as the sum

$$p = p_{\text{dyn}} + p_{\text{hs}} + p_{\text{os}}. \quad (3.8)$$

Hence, we combine the hydrodynamic, the hydrostatic and osmotic pressures into the total pressure. Note, even though the hydrostatic and osmotic pressures do not appear explicit in Navier–Stokes equation when we use the total pressure formulation, their effects do not disappear. The charged ionic species make up the electric charge density in terms of their valences  $Z^{(i)}$  and their concentration fields

$$\rho_{\text{el}} = e \sum_i Z^{(i)} c^{(i)}, \quad (3.9)$$

where  $e$  is the elementary charge. The electric field is related to the magnetic field  $\mathbf{B} = \mathbf{B}(\mathbf{r}, t)$  through the Maxwell–Faraday equation

$$\nabla \times \mathbf{E} = -\partial_t \mathbf{B}. \quad (3.10)$$

Electric quasi-statics is assumed under the presumption that any electric oscillations with angular frequency  $\omega_l$  and in the confined space of size  $l$  meet the demand

$$\omega_l l \ll c_l, \quad (3.11)$$

where  $c_l$  is the speed of light in the fluid. In this regime Equation (3.10) simplifies to

$$\nabla \times \mathbf{E} = 0, \quad (3.12)$$

which implies that the electric vector field can be represented by the gradient of an electric scalar potential  $\phi = \phi(\mathbf{r}, t)$

$$\mathbf{E} = -\nabla \phi. \quad (3.13)$$

Utilizing the assumption of incompressibility, the total pressure, the expression of the electric charge density, and the scalar formulation of the electric field, the Navier–Stokes equations are

$$\rho_b [\partial_t \mathbf{v} + (\mathbf{v} \cdot \nabla) \mathbf{v}] = -\nabla p + \eta \nabla^2 \mathbf{v} - e \left( \sum_i Z^{(i)} c^{(i)} \right) \nabla \phi. \quad (3.14)$$

### 3.2.3 Electric interaction

Electric interactions are governed by Poisson’s equation

$$\nabla \cdot \mathbf{D} = \rho_{\text{el}}, \quad (3.15)$$

where  $\mathbf{D}$  is the electric displacement field, in general defined by

$$\mathbf{D} = \varepsilon_0 \mathbf{E} + \mathbf{P}, \quad (3.16)$$

where  $\mathbf{P}$  is the electric polarization and  $\varepsilon_0$  is the permittivity of free space. The electrolyte is assumed to be linear, isotropic and homogeneous with respect to its electric properties whereby the electric polarization is directly proportional to the electric field

$$\mathbf{P} = \varepsilon_0 \chi_e \mathbf{E}, \quad (3.17)$$

where  $\chi_e$  is the constant electric susceptibility. This in turn makes the electric displacement field directly proportional to the electric field

$$\mathbf{D} = (1 + \chi_e) \varepsilon_0 \mathbf{E} = \varepsilon_r \varepsilon_0 \mathbf{E} = \varepsilon \mathbf{E}. \quad (3.18)$$

With the above definitions and the expression of the charge density from Equation (3.9), Poisson's equation for an isotropic electrolyte simplifies to

$$\nabla^2 \phi = -\frac{e}{\varepsilon} \sum_i Z^{(i)} c^{(i)}. \quad (3.19)$$

### 3.2.4 Transport of species

The continuum assumption makes it possible to use conservation equations for the ionic species of the form

$$\partial_t c^{(i)} + \nabla \cdot \mathbf{J}^{(i)} = 0, \quad (3.20)$$

where  $\mathbf{J}^{(i)}$  are particle current densities with contributions from diffusion, electro-migration and convection. Diffusion and electro-migration are caused by gradients in the electrochemical potential  $\mu^{(i)} = \mu^{(i)}(\mathbf{r}, t)$ ; convection stems from an imbalance of forces on the solution [20, 23]

$$\mathbf{J}^{(i)} = c^{(i)} \left( -D^{(i)} \nabla \mu^{(i)} + \mathbf{v} \right), \quad (3.21)$$

where  $D^{(i)}$  is the diffusivity for species  $c^{(i)}$ . For an ideal dilute system the interaction between different species can be neglected and the electrochemical potential can be decomposed into separate entropic and electric terms [20]

$$\mu^{(i)} = k_B T \ln \frac{c^{(i)}}{c_0} + Z^{(i)} e \phi, \quad (3.22)$$

where  $k_B$  is Boltzmann's constant,  $T$  the temperature and  $c_0$  a reference concentration. With these assumptions Equations (3.21) reduce to the Nernst–Planck equations

$$\mathbf{J}^{(i)} = -D^{(i)} \left( \nabla c^{(i)} + \frac{Z^{(i)} e}{k_B T} c^{(i)} \nabla \phi \right) + c^{(i)} \mathbf{v}. \quad (3.23)$$

Note, that in this framework the particle current can be written as a sum of a purely diffusive term  $\mathbf{J}_{\text{diff}}^{(i)}$ , a purely electro-migrative term  $\mathbf{J}_{\text{em}}^{(i)}$  and a purely convective term  $\mathbf{J}_{\text{conv}}^{(i)}$

$$\mathbf{J}^{(i)} = \mathbf{J}_{\text{diff}}^{(i)} + \mathbf{J}_{\text{em}}^{(i)} + \mathbf{J}_{\text{conv}}^{(i)}, \quad (3.24)$$

where the terms are given by

$$\mathbf{J}_{\text{diff}}^{(i)} = -D^{(i)} \nabla c^{(i)}, \quad (3.25a)$$

$$\mathbf{J}_{\text{eo}}^{(i)} = -D^{(i)} \frac{Z^{(i)} e}{k_B T} c^{(i)} \nabla \phi, \quad (3.25b)$$

$$\mathbf{J}_{\text{conv}}^{(i)} = c^{(i)} \mathbf{v}. \quad (3.25c)$$

### 3.2.5 Remark on the full nonlinear model

One of the main characteristics that sets the full nonlinear model apart from the two others, is that it allows concentration gradients and hence a non-zero charge density. The non-zero charge density occurs in the region of the electric double layer. In this region many of the physical fields change rapidly over a typical distance of 10 nm which has to be compared to the size of a typical microsystem, where dimensions range from  $\mu\text{m}$  to  $\text{mm}$ . In numerical simulations of electrokinetic phenomena in microsystems the model requires that this difference in length scales is accounted for. Unfortunately, this is troublesome since it entails the use of many computational degrees of freedom (DOFs) in order to ensure sufficient resolution of the thin double layer. For this reason, it is attractive to use effective boundary conditions to model the physics of the thin Debye layer. The effective slip-velocity boundary condition we use here is derived from the full nonlinear model and this derivation is the subject of the next section.

### 3.2.6 The electric double layer at a charged surface

In this section we investigate the equilibrium of a binary, symmetric electrolyte at a charged surface. The result is an effective slip-velocity boundary condition.

The electrolyte consists of positively charged  $c^{(+)} = c^{(+)}(\mathbf{r})$  and negatively charged  $c^{(-)} = c^{(-)}(\mathbf{r})$  ionic species. The valence of the positive  $Z^{(+)}$  and negative  $Z^{(-)}$  ionic species are related by

$$Z^{(+)} = -Z^{(-)} = Z. \quad (3.26)$$

The electric potential at the surface  $\partial\Omega$  is assumed to be

$$\phi|_{\mathbf{r} \in \partial\Omega} = \zeta, \quad (3.27)$$

and goes to zero infinitely far away from the surface

$$\lim_{|\mathbf{r}| \rightarrow \infty} \phi = 0, \quad (3.28)$$

while the only assumption on the ionic species is

$$\lim_{|\mathbf{r}| \rightarrow \infty} c^{(\pm)} = c_0. \quad (3.29)$$

Since the system is in equilibrium there is no net particle currents  $\mathbf{J}^{(\pm)} = 0$  and the velocity is zero and hence Equations (3.21) and (3.22) give

$$0 = \nabla \left( k_B T \ln \frac{c^{(\pm)}}{c_0} \pm Ze\phi \right), \quad (3.30)$$

where it has been assumed  $c^{(\pm)} \neq 0$ . Utilizing the above boundary conditions we integrate Equation (3.30) and get

$$c^{(\pm)} = c_0 \exp \left( \mp \frac{Ze}{k_B T} \phi \right). \quad (3.31)$$

Consequently, the charge density becomes

$$\rho_{\text{el}} = Ze \left( c^{(+)} - c^{(-)} \right) = -2Zec_0 \sinh \left( \frac{Ze}{k_{\text{B}}T} \phi \right). \quad (3.32)$$

The resulting equation is called the Poisson–Boltzmann equation

$$\nabla^2 \phi = 2 \frac{Zec_0}{\varepsilon} \sinh \left( \frac{Ze}{k_{\text{B}}T} \phi \right), \quad (3.33)$$

which, as shown below, is analytically solvable for simple systems. First, consider the limit where the electric energy  $Ze\zeta$  is low compared to the thermal energy  $k_{\text{B}}T$

$$\frac{Ze\zeta}{k_{\text{B}}T} \ll 1. \quad (3.34)$$

This is the so-called Debye–Hückel limit, where the Debye–Hückel screening length  $\lambda_D$  is given by

$$\lambda_D = \sqrt{\frac{\varepsilon k_{\text{B}}T}{2c_0 Z^2 e^2}}. \quad (3.35)$$

Equation (3.33) simplifies to

$$\nabla^2 \phi = \frac{1}{\lambda_D^2} \phi, \quad (3.36)$$

where we have used that  $\sinh(x) \approx x$  for  $x \ll 1$ . At room temperature  $T \approx 300$  K the thermal voltage is

$$\frac{k_{\text{B}}T}{e} \approx 25 \text{ mV}. \quad (3.37)$$

Typical experimentally measured values for the zeta-potential is in the range 10 mV to 100 mV [9], which demonstrates that the Debye–Hückel approximation has to be used with precaution.

### 3.2.7 Infinite plane

We can solve Equation (3.33) analytically for the special case of an infinite planar wall. Thus, consider the system depicted in Figure 3.1 on page 22 where an infinite large plane with surface normal  $\hat{\mathbf{n}} = \mathbf{e}_z$  at  $z = 0$  carries a surface charge (hence has a potential of  $\zeta$ ) and where the space  $z > 0$  is occupied with a binary, symmetric electrolyte. The system is translational invariant in the  $x$ - and  $y$ -direction such that the electric potential only depends on the  $z$ -coordinate  $\phi = \phi(z)$ . The solution to Equation (3.33) is called the Gouy–Chapmann solution

$$\phi(z) = \frac{4k_{\text{B}}T}{Ze} \operatorname{arctanh} \left[ \tanh \left( \frac{Ze\zeta}{4k_{\text{B}}T} \right) \exp \left( -\frac{z}{\lambda_D} \right) \right], \quad (3.38)$$

which is valid for arbitrarily high potentials. In the Debye–Hückel limit the solution to Equation (3.36) is

$$\phi(z) = \zeta \exp \left( -\frac{z}{\lambda_D} \right). \quad (3.39)$$

Furthermore, in this limit we can obtain the concentrations by Taylor-expanding Equation (3.31)

$$c^{(\pm)} = c_0 \left[ 1 \mp \frac{Ze\zeta}{k_B T} \exp\left(-\frac{z}{\lambda_D}\right) \right]. \quad (3.40)$$

The concentrations decay exponentially from their surface value to  $c_0$  in the bulk, as expected.

### 3.2.8 Parallel plates channel

Another special case we can solve analytically is that of parallel plates. This system is attractive in the context of microfluidics because it is a good approximation to straight, narrow microchannels. The system is completely analogous to the above case, only now there are two parallel, infinite plates at  $z = \pm H/2$ . Given the boundary conditions

$$\phi\left(\pm\frac{H}{2}\right) = \zeta, \quad (3.41)$$

the solution of Equation (3.36) is

$$\phi(z) = \zeta \frac{\cosh\left(\frac{z}{\lambda_D}\right)}{\cosh\left(\frac{H}{2\lambda_D}\right)}, \quad (3.42)$$

which we will use in the next section to derive the Helmholtz–Smoluchowski slip-velocity.

### 3.2.9 Application of external electric field to parallel plates channel

We will now use the results from the infinite plane and parallel plates to calculate the EO-flow when an external tangential electric field is applied to a parallel plates microchannel. We consider two cases; (i) only the lower wall carries a surface charge and produce one-wall EO-flow, and (ii) both walls carry a surface charge and produce two-wall EO-flow, see Figure 3.2. We assume that each physical quantity is a sum of an intrinsic and an externally applied field. Thus, the externally applied pressure  $p_{\text{ext}} = p_{\text{ext}}(\mathbf{r}, t)$ , electric potential  $\phi_{\text{ext}} = \phi_{\text{ext}}(\mathbf{r}, t)$ , and concentration field(s)  $c_{\text{ext}} = c_{\text{ext}}(\mathbf{r}, t)$  can be added with the intrinsic equilibrium pressure  $p_{\text{eq}} = p_{\text{eq}}(\mathbf{r}, t)$ , electric potential  $\phi_{\text{eq}} = \phi_{\text{eq}}(\mathbf{r}, t)$ , and concentration field(s)  $c_{\text{eq}} = c_{\text{eq}}(\mathbf{r}, t)$

$$p = p_{\text{eq}} + p_{\text{ext}}, \quad (3.43a)$$

$$\phi = \phi_{\text{eq}} + \phi_{\text{ext}}, \quad (3.43b)$$

$$c = c_{\text{eq}} + c_{\text{ext}} \quad (3.43c)$$

Two driving electrodes delivers the applied DC electric field  $\mathbf{E}_{\text{ext}}$

$$\mathbf{E}_{\text{ext}} = -\nabla\phi_{\text{ext}}. \quad (3.44)$$

Furthermore, we assume that electrochemical processes take place at the driving electrodes such that no double layers are formed here, which would otherwise screen the effect of the

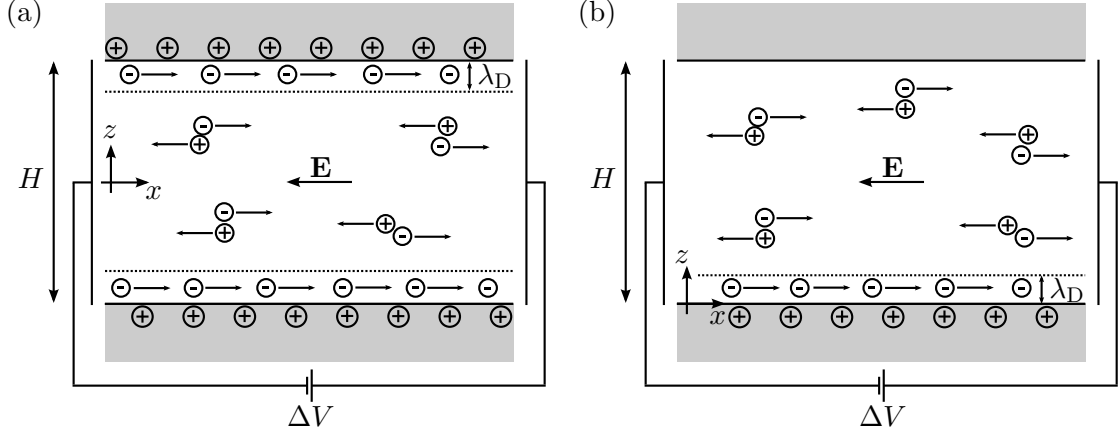


**Figure 3.2:** A parallel plates channel of height  $H$  for which (a) both walls carry a surface charge, and (b) only the lower wall carries a surface charge. We apply an electric field  $\mathbf{E} = -E\mathbf{e}_x$  whereby the ions in bulk begins to electromigrate. However, due to electro-neutrality, no net force is transferred to the electrolyte in the bulk. Contrary, in the Debye layer(s) the movement of the prevailing amount of counter-ions creates a net force on the electrolyte, and through viscous drag an EO-flow is generated. We look at this situation in steady-state.

external electric field. Also, we assume that the externally applied electric field does not introduce any changes in the intrinsic charge density  $\rho_{\text{el}}^{\text{eq}}$ . Under these assumptions Navier–Stokes equations are

$$\rho_b [\partial_t \mathbf{v} + (\mathbf{v} \cdot \nabla) \mathbf{v}] = -\nabla p_{\text{ext}} + \eta \nabla^2 \mathbf{v} + \rho_{\text{el}}^{\text{eq}} \mathbf{E}_{\text{ext}}. \quad (3.45)$$

Additionally, it is assumed that (i) the zeta potential is constant along the wall(s), (ii) the electric field is homogeneous, (iii) the flow is in steady-state, and (iv) the Debye length is much smaller than the half-width  $H/2$  of the channel,  $\lambda_D \ll H/2$ . The direction of the externally applied electric field is in the negative  $x$ -direction and the external pressure gradient is zero. Also, due to the translational invariance in the  $x$ - and  $y$  direction and that the driving force is along the  $x$ -direction, the velocity is simplified, and thus the fields are

$$\mathbf{E}_{\text{ext}} = -E\mathbf{e}_x, \quad (3.46a)$$

$$\nabla p_{\text{ext}} = \mathbf{0}, \quad (3.46b)$$

$$\mathbf{v} = v_x(z)\mathbf{e}_x, \quad (3.46c)$$

whereby Navier–Stokes equations reduce to

$$0 = \eta \partial_z^2 v_x(z) + [\varepsilon \partial_z^2 \phi_{\text{eq}}(z)] E. \quad (3.47)$$

In the situation where both walls carries a surface charge the  $z$ -axis origin is at the middle of the channel and we assume no-slip boundary conditions at the walls

$$v_x^\pm \left( \pm \frac{H}{2} \right) = 0, \quad (3.48)$$

where we have put two lines in superscript to distinguish between the one- and two-wall EO-flow. Furthermore, in the picture where only the lower wall carries a surface charge the  $z$ -axis origin is at the lower wall and the no-slip boundary conditions are

$$v_x^-(0) = v_x^-(H) = 0. \quad (3.49)$$

We use the expression for the equilibrium potential from Equation (3.42) and get for the two-wall EO-flow

$$v_x^-(z) = v_{eo} \left[ 1 - \frac{\cosh\left(\frac{z}{\lambda_D}\right)}{\cosh\left(\frac{H}{2\lambda_D}\right)} \right]. \quad (3.50)$$

Likewise, we use the expression for the equilibrium potential from Equation (3.39) and get for the one-wall EO-flow

$$v_x^-(z) = v_{eo} \left\{ 1 - \exp\left(-\frac{z}{\lambda_D}\right) - \frac{z}{H} \left[ 1 - \exp\left(-\frac{H}{\lambda_D}\right) \right] \right\}. \quad (3.51)$$

In both solutions the so-called EO velocity  $v_{eo}$  is defined as

$$v_{eo} = \frac{\varepsilon\zeta}{\eta} E. \quad (3.52)$$

We plot the velocity profiles of the one-wall and two-wall EO-flow in Figure 3.3 for the three cases  $\lambda_D/(H/2) = \{0.1, 0.01, 0.001\}$ . Note, that for  $\lambda_D/(H/2) \ll 1$  we almost have a perfect Couette and plug flow for the one- and two-wall EO-flow, respectively. Consequently, instead of resolving the thin Debye layer, an effective slip-velocity can be used instead. This leads to the linear- and nonlinear slip-velocity models which are the topic of the next section.

### 3.3 Slip-velocity models

We can use the Helmholtz–Smoluchowski velocity as an effective boundary condition if the Debye length is much smaller than the half width of the channel  $\lambda_D/(H/2) \ll 1$ . In this way we avoid the trouble of resolving the thin Debye layer and we have a unidirectional coupling from the electrostatic problem to the hydrodynamic flow, or in other words we decouple the problem. We exploit this feature in the linear- and nonlinear slip-velocity models, where the basic assumption is an infinitely thin double layer.

#### 3.3.1 Effective slip-velocity boundary condition for the linear and nonlinear slip-velocity models

The Helmholtz–Smoluchowski boundary condition is not restricted to the special case of parallel plates, but can be used on arbitrary surfaces via

$$\mathbf{v}_{hs} = -\frac{\varepsilon\zeta}{\eta} \mathbf{E}_s, \quad (3.53)$$



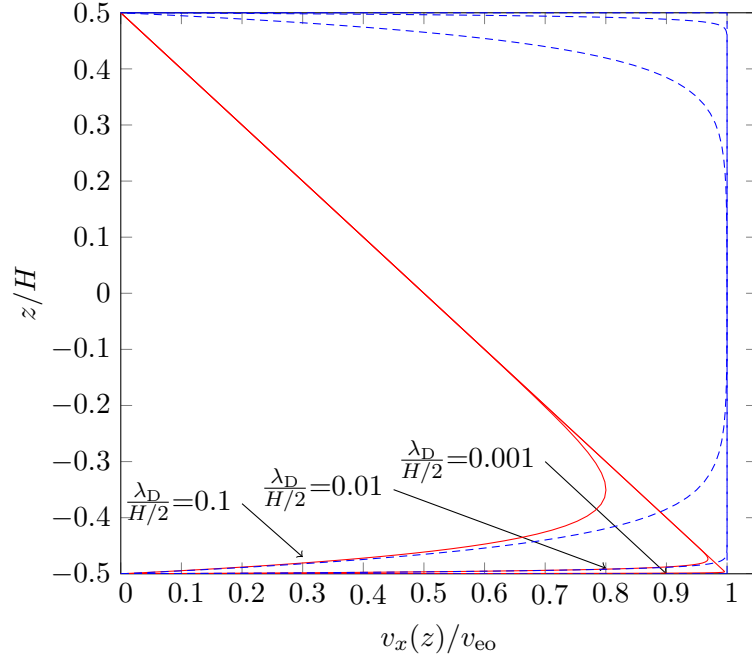


**Figure 3.3:** One-wall (red) and two-wall (dashed, blue) EO-flow velocity profiles normalized with  $v_{eo}$  in a parallel plates channel of height  $H$  filled with an electrolyte with intrinsic Debye screening length  $\lambda_D$ . We have used three parameters of  $\lambda_D/(H/2) = \{0.1, 0.01, 0.001\}$ . Note, for  $\lambda_D/(H/2) \leq 0.01$  the velocity profiles are close to perfect Couette and plug flows for the one- and two-wall EO-flow, respectively. This indicates that we can use the Helmholtz–Smoluchowski velocity as an effective boundary condition as long  $\lambda_D/(H/2) \ll 1$ .

where  $\mathbf{E}_s$  is the component of the electric field parallel to the surface given by

$$\mathbf{E}_s = \mathbf{E} - \hat{\mathbf{n}}(\hat{\mathbf{n}} \cdot \mathbf{E}), \quad (3.54)$$

where  $\hat{\mathbf{n}}$  is the surface normal vector.

### 3.3.2 Bulk equations for the linear and nonlinear slip-velocity models

We have assumed that the electric double layer is infinitely thin and thereby complete electro-neutrality

$$\rho_{el} = 0. \quad (3.55)$$

Thus, the electric force density drops out of Navier–Stokes equations

$$\rho_b [\partial_t \mathbf{v} + (\mathbf{v} \cdot \nabla) \mathbf{v}] = -\nabla p + \eta \nabla^2 \mathbf{v}, \quad (3.56)$$

and Poisson’s equation turns into Laplace’s equation

$$\nabla^2 \phi = 0. \quad (3.57)$$

We have now decoupled the hydrodynamic and electrostatic problems. With the linear and nonlinear slip velocity models we solve a given electrokinetic problem by first solving for the electrostatic potential. Having the electric potential, we can solve for the hydrodynamic flow using Equation (3.53) as an effective boundary condition on the electro-osmotic active boundaries. This is a significant simplification, both in terms of analytical and numerical manageability.

The difference between the linear and nonlinear slip-velocity models are the surface conduction in the Debye layer. This difference manifests itself in the boundary condition for the electrostatic potential on the electro-osmotic active walls.

### 3.4 Linear slip velocity model

In the linear slip-velocity model we neglect all charge dynamics in the double layer and assume complete electrical screening

$$\hat{\mathbf{n}} \cdot \nabla \phi = 0. \quad (3.58)$$

Note, this is an oversimplification, especially in the case of a high applied electric field. Nevertheless, this model is widely used and is for many purposes adequate for predicting EO-flows qualitatively. Though, in quantitative comparisons with experiments this model has shown to overestimate the slip velocity [21].

### 3.5 Nonlinear slip velocity model

The nonlinear slip velocity model is an extension of the linear slip velocity model in the sense that it gives more accurate results for high zeta-potentials where the Debye–Hückel approximation breaks down. However, it is purely a model for ICEO, and not for ordinary EO-flow. We will explain more about ICEO shortly.

The nonlinear slip-velocity model is accredited to Gaurav Soni from UCSB [21]. It realizes the electric double layer by solving a partial differential equation (PDE) on the double-layer-inducing surface. In short, the PDE is derived by conserving ionic charge in the double layer, where a normal ohmic current and a tangential surface conduction current are both considered in the charge conservation. It also allows for a nonlinear surface capacitance, which relates the surface charge density to the zeta-potential of the surface. This is more advanced than the linear slip-velocity model (or the Debye–Hückel approximation), which ignores the presence of surface conduction and uses a linearized surface capacitance; these simplifications are not valid for situations where the zeta-potential is much higher than the thermal voltage.

#### 3.5.1 Induced-charge electro-osmosis

ICEO refers to a phenomenon where a DC or AC electric field induces charge on a polarizable surface (metal or dielectric), and produces an electroosmotic slip by applying a body force on the electric double layer. Since the double layer is created and moved by

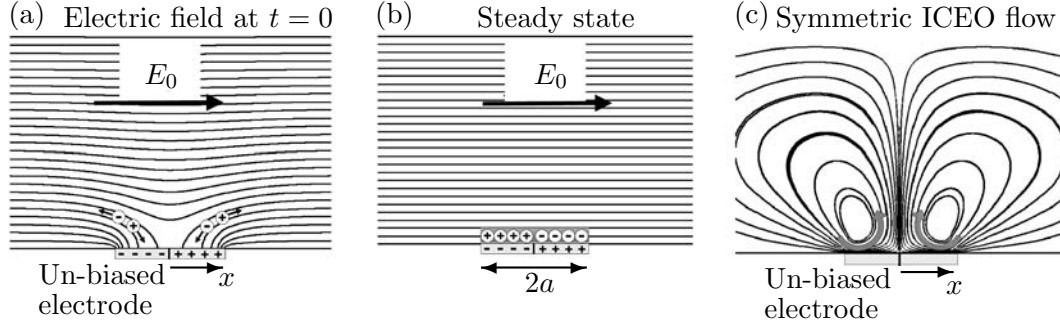


**Figure 3.4:** (a) The ICEO situation in the vicinity of the planar, un-biased electrode of width  $2a$ , immediately after  $t = 0$  the external electric field  $E_0$  is applied. (b) The ICEO situation at steady-state. (c) Flow lines of the symmetric ICEO flow.

the same electric field, this phenomenon gives rise to steady flows both in DC and AC electric fields. Consider a flat un-biased electrode surface of width  $2a$  in contact with an electrolytic solution, see Figure 3.4. When it is subjected to an external electric field  $\mathbf{E} = E\mathbf{e}_x$  at  $t = 0$ , the electric field lines intersect the surface at right angles and a charge density is induced on the surface because of charge separation. However, the field lines start changing their configuration as an electric current  $\mathbf{J}_{el} = \sigma\mathbf{E}$  drives positive ions toward one half of the surface ( $x < 0$ ) and negative ions to the other half ( $x > 0$ ). This process develops a double layer on the surface which grows as long as the normal electric field drives ions into it. In steady state, assuming that there is no surface conduction or faradaic reaction, the double layer insulates the surface completely and no electric field lines can penetrate into it. In this state, all the electric field lines are tangential to the surface and cause an electroosmotic slip directed from the edges toward the center giving rise to two symmetric rolls above the surface. An AC field will drive an identical flow as the change in direction of the field changes the polarity of the induced charge as well.

### 3.5.2 Surface conduction

Ions are brought into the double layer by the normal component of the electric field. However, the ions can also move tangential to the electrode surface due to the tangential component of the electric field and with the electroosmotic flow of the fluid i.e. by convection. Movement of ions along the electrode surface is generally referred to as surface conduction. When the applied potentials are high, the surface conduction is strong enough to change the electric field close to the electrode surface. Surface conduction creates a large tangential current which takes away the ions shielding the surface charge. In order to replenish the charge into the double layer, a lot of electric field lines become normal to the double layer. The normal current thus generated brings new ions into the double layer

for replenishment. Excessive surface conduction causes a large reduction in the tangential component of the electric field and thus deteriorates the slip velocity. In the presence of excessive surface conduction almost all electric field lines can become normal and leave no tangential field to drive the electroosmotic flow.

The electric surface current  $\mathbf{J}_s$  is dependent on the surface conductivity  $\sigma_s$  of the double layer

$$\mathbf{J}_s = \sigma_s \mathbf{E}_s, \quad (3.59)$$

where  $\mathbf{E}_s$  is the tangential electric field defined in Equation (3.54) The surface conductivity  $\sigma_s$  of a binary, symmetric electrolyte with

$$Z^{(+)} = -Z^{(-)} = Z, \quad (3.60a)$$

$$D^{(+)} = D^{(-)} = D, \quad (3.60b)$$

is given by [21]

$$\sigma_s = 4\lambda_D \sigma (1 + m) \sinh^2 \left( \frac{Ze\zeta}{k_B T} \right), \quad (3.61)$$

where  $\sigma$  is the bulk conductivity and

$$m = 2 \frac{\varepsilon}{\eta D} \left( \frac{k_B T}{Ze} \right)^2, \quad (3.62)$$

is a dimensionless parameter indicating the relative contribution of electroosmosis to surface conduction. For an aqueous solution of KCl at room temperature  $m \approx 0.45$ . Usually, the surface conduction is expressed in terms of a dimensionless parameter, the Dukhin number  $Du$

$$Du = \frac{\sigma_s}{\sigma a}, \quad (3.63)$$

where  $a$  is a characteristic length scale.

### 3.5.3 Charge conservation in the double layer

If we assume an infinitely thin double layer  $\lambda_D/a \ll 1$  and that double layer charging does not cause any gradients in the bulk electrolyte concentration, it is possible to derive a conservation law for the double layer surface charge density  $q$ . We consider a small patch of thin double layer where the charge is brought into it by a normal ohmic flux, see Figure 3.5 (a). This charge can accumulate or leak tangentially from the edges. A conservation law is then simply

$$\text{rate of accumulation} = \text{flux in} - \text{flux out},$$

which in mathematical form can be expressed as an integral over the surface  $S$

$$\int_S \partial_t q \, da = - \int_S \hat{\mathbf{n}} \cdot (\sigma \mathbf{E}) da - \int_{\partial S} \hat{\mathbf{n}}_s \cdot (\sigma_s \mathbf{E}_s) ds, \quad (3.64)$$

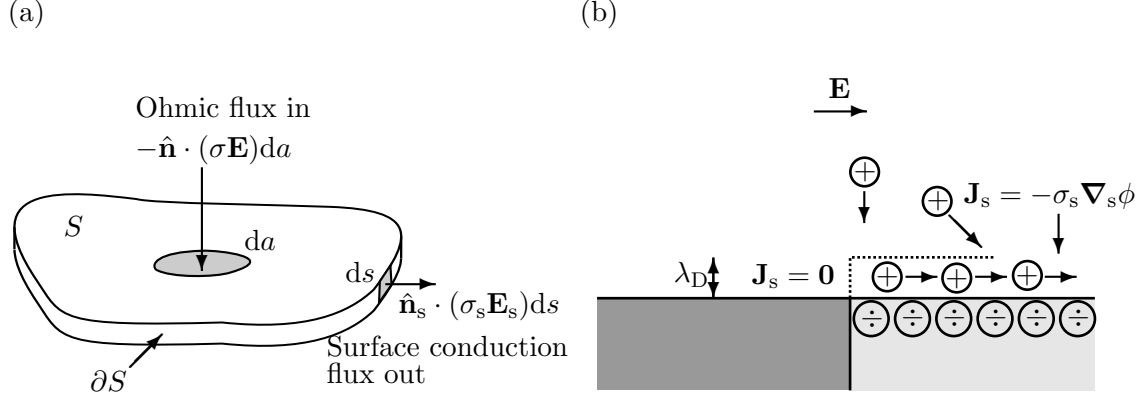


**Figure 3.5:** (a) Conservation of surface charge by a tangential surface conduction flux and a normal ohmic flux. (b) The surface conduction flux  $\mathbf{J}_s$  is zero at the edge of the electrode and therefore electric field lines become perpendicular so that ions can be supplied into the double layer to sustain the surface conduction flux away from the edge [21, 24]

where  $\hat{\mathbf{n}}$  is the outward normal vector and  $\hat{\mathbf{n}}_s$  is a vector tangential to the surface but perpendicular to the boundary. The second term is converted into an area integral by applying the divergence theorem

$$\int_S \partial_t q \, da = - \int_S \hat{\mathbf{n}} \cdot (\sigma \mathbf{E}) da - \int_S \nabla_s \cdot (\sigma_s \mathbf{E}_s) da, \quad (3.65)$$

where  $\nabla_s$  is the tangential gradient operator

$$\nabla_s = \nabla - \hat{\mathbf{n}} (\hat{\mathbf{n}} \cdot \nabla). \quad (3.66)$$

Since Equation (3.65) holds true for any arbitrarily small surface, the integrals can be removed

$$\partial_t q = -\hat{\mathbf{n}} \cdot (\sigma \mathbf{E}) - \nabla_s \cdot (\sigma_s \mathbf{E}_s), \quad (3.67)$$

and by using

$$\mathbf{E} = -\nabla \phi, \quad (3.68a)$$

$$\mathbf{E}_s = -\nabla_s \phi, \quad (3.68b)$$

the resulting conservation equation is

$$\partial_t q = \hat{\mathbf{n}} \cdot (\nabla \phi) + \nabla_s \cdot (\sigma_s \nabla_s \phi). \quad (3.69)$$

This equation constitutes an effective boundary condition for the electrostatic potential on the electrode surface. Note, in steady-state the PDE simply reads

$$0 = \hat{\mathbf{n}} \cdot (\nabla \phi) + \nabla_s \cdot (\sigma_s \nabla_s \phi), \quad (3.70)$$

which we will use later. Furthermore, we need to apply boundary conditions to the surface PDE in Equation (3.69). The edge of the electrode is visualized as a surface charge discontinuity kept in an external field, see Figure 3.5 (b). On one side of the edge, there is no surface charge and thus there is no double layer; hence no surface conduction flux can enter from the edge. Consequently, on the edge, electric field lines terminate perpendicularly to the electrode so that ions can be supplied into the double layer. In this picture there is no tangential electric field on the edge. On other points in the vicinity of the edge, the electric field has a tangential component which causes the ions to conduct away from the edge. Hence, we assume that the surface conduction flux is zero at the edge of the electrode

$$\hat{\mathbf{n}}_s \cdot (\sigma_s \nabla_s \phi) = 0. \quad (3.71)$$

Where the double layer in the linear slip velocity model leaves the electric field unaffected, it interacts with the electric field in the nonlinear slip-velocity model. The altered field distribution in the vicinity of the double layer is what makes the difference between the linear- and nonlinear slip-velocity models, as the fluid slip condition still is given by the Helmholtz–Smoluchowski velocity Equation (3.53), but now with  $\zeta$  and  $\mathbf{E}_s$  dependent on the surface conduction in the double layer.

We now have a strong foundation for doing numerical simulations on electrokinetic phenomena. We will use the full nonlinear and linear slip-velocity models in Chapter 5 to simulate the observed concentration drop across an un-biased electrode in a microchannel. In Chapter 6 we compare the linear- and nonlinear slip-velocity models against the full nonlinear model and quantify the deviations in an ICEO-flow for different parameters. In the next chapter we introduce the numerical implementation in COMSOL and do a benchmark against the analytical EO plug flow.

## Chapter 4

# Numerical implementation and validation in COMSOL

COMSOL is a powerful interactive environment for modeling and solving all kinds of scientific and engineering problems based on partial differential equations [25]. The software makes it possible to extend conventional models for one type of physics into multiphysics models that solve coupled physics phenomena simultaneously. It does not require an in-depth knowledge of mathematics or numerical analysis to use the software. The physics problem is written in one of three special syntaxes; *(i)* coefficient form, *(ii)* general (or strong) form, or *(iii)* weak form. In short, the coefficient form is for linear or almost linear PDEs, the general form is for nonlinear PDEs, and the weak form offers the maximum flexibility. Here we will employ the weak form because the problems we solve are very complex and in particular because they include numerically non-trivial boundary conditions. When the problem is described in one of the three syntaxes, COMSOL then internally compiles a set of PDEs representing the entire model. The problems can be defined in a graphical user interface or in MATLAB script language. COMSOL uses the finite element method (FEM) and runs the finite element analysis together with adaptive meshing and error control using a variety of numerical solvers. Consequently, we can easily define complex geometries in COMSOL or solve problems where high precision is only required in some parts of the domain. Finally, we note that we have used COMSOL version 3.4 for the the current work, but even as this thesis is written we have started using COMSOL version 3.5. Now follows a short description of the weak form.

### 4.1 Weak form implementation in COMSOL

The weak form is a particular way of specifying a model in COMSOL with a more general syntax. First, weak does not mean that the approach is inferior; weak form is very powerful and flexible. Weak form is a term borrowed from mathematics, but it has a slightly different meaning in this context. The strong points of the weak form that are relevant to this works is that it can *(i)* solve strongly nonlinear problems, *(ii)* add and modify nonstandard constraints, and *(iii)* build models with PDEs on boundaries, edges

and points. Additionally, adding weak constraints provides accurate fluxes and reaction forces. Furthermore, the weak solution form gives the exact Jacobian necessary for fast convergence of strongly nonlinear problems.

#### 4.1.1 Short derivation of the weak form

First, consider a general PDE problem for a single variable  $u$  defined on the 2D domain  $\Omega$  with boundary  $\partial\Omega$  in strong form

$$\partial_j \Gamma_{ij} = F_i, \quad i = x, y, \quad \text{in } \Omega, \quad (4.1)$$

where we use the Einstein summation notation. Let  $u^{(t)}$  be an arbitrary function on  $\Omega$  called the test-function ( $u^{(t)}$  belongs to a suitable chosen, well-behaved class of functions). Multiplying the PDE with this function and integrating yields

$$\int_{\Omega} u^{(t)} \partial_j \Gamma_{ij} da = \int_{\Omega} u^{(t)} F_i da. \quad (4.2)$$

We now use Green's theorem to integrate by parts

$$\int_{\partial\Omega} u^{(t)} (\hat{n}_j \Gamma_{ij}) ds - \int_{\Omega} [\partial_j u^{(t)}] \Gamma_{ij} da = \int_{\Omega} u^{(t)} F_i da. \quad (4.3)$$

This is rearranged to fit COMSOL syntax

$$0 = - \int_{\partial\Omega} u^{(t)} (\hat{n}_j \Gamma_{ij}) ds + \int_{\Omega} \left\{ [\partial_j u^{(t)}] \Gamma_{ij} + u^{(t)} F_i \right\} da. \quad (4.4)$$

This is the weak reformulation of the original PDE. Note, we have reduced the bulk divergence term  $\partial_j \Gamma_{ij}$  to a (Neumann) boundary condition  $\hat{n}_j \Gamma_{ij}$ . We simply substitute  $\hat{n}_j \Gamma_{ij}$  on the boundary where we want to implement a (Neumann) boundary condition. Dirichlet boundary conditions are still specified in strong form syntax

$$R_i = 0. \quad (4.5)$$

The weak formulation is a weaker condition on the solution than the strong form formulation. For instance, in the case of discontinuities in material properties, it is possible to find a solution in weak form while the strong form has no meaning. For this reason we use the weak form in the numerical simulations. With the weak form comes the implementation of weak constraints which is the subject of the next section.

#### 4.1.2 Weak constraints

COMSOL implements weak constraints by using finite elements on the constrained domain for the Lagrange multipliers, and by solving for the Lagrange multipliers along with the original problem. The advantages of weak constraints are (i) that they provide very accurate flux computations, (ii) that they handle nonlinear constraints; weak constraints can handle general nonlinearities because the Lagrange multipliers are updated as a part



of the solution-vector and give correct contributions to the stiffness matrix. (iii) They can implement constraints including derivatives — standard constraints only allows constraints on the tangential component of the derivative, whereas only weak constraints can handle nontangential restraints. However, one of the draw-backs of weak constraints are that the problem size increases, because extra unknowns are introduced for the Lagrange multipliers.

### Ideal and nonideal constraints

Using nonideal constraints modifies the way boundary conditions are interpreted. Switching to nonideal weak constraints therefore can modify the physics of the model.

The difference between ideal and nonideal constraints is the way the Lagrange multipliers — which can be interpreted as generalized reaction forces — are applied. In an ideal constraint, the Lagrange multipliers are applied symmetrically on all dependent variables involved in the constraint, so as to keep symmetric problems symmetric. In a nonideal constraint, the reaction forces are applied only on the corresponding dependent variable at the boundary where the constraint is specified.

Imagine a model with two dependent variables  $u$  and  $v$ . Furthermore, imagine a boundary  $\partial\Omega_i$  where we want to apply the boundary condition

$$u - v = 0, \quad \text{on } \partial\Omega_i. \quad (4.6)$$

The corresponding ideal weak constraint is

$$\int_{\partial\Omega_i} \mu^{(t)} (u - v) \, ds + \int_{\partial\Omega_i} \mu \left[ u^{(t)} - v^{(t)} \right] \, ds, \quad (4.7)$$

where  $\mu$  and  $\mu^{(t)}$  are the Lagrange multiplier and corresponding test function, and  $u^{(t)}$  and  $v^{(t)}$  are the test functions corresponding to  $u$  and  $v$ , respectively. Since  $\mu$  multiplies both test functions in the second integral, both  $u$  and  $v$  are affected by the constraint, which therefore is bidirectional. The corresponding nonideal weak constraint is

$$\int_{\partial\Omega_i} \mu^{(t)} (u - v) \, ds + \int_{\partial\Omega_i} \mu u^{(t)} \, ds. \quad (4.8)$$

Here, the Lagrange multiplier  $\mu$  only multiplies the test function  $u^{(t)}$ . All reaction forces therefore apply only to  $u$ , while  $v$  is left unaffected by the constraint. This makes the nonideal constraint unidirectional. We will make use of this feature when we apply the Helmholtz–Smoluchowski slip velocity as a boundary condition; there we need to couple unidirectional from the electric field to the hydrodynamic velocity fields and would not be able to do this without nonideal constraints.

## 4.2 Validation

As validation of the numerical framework we compute an EO-flow in a parallel plates channel and compared with the analytical solution. This model utilizes the nonideal constraints discussed above.

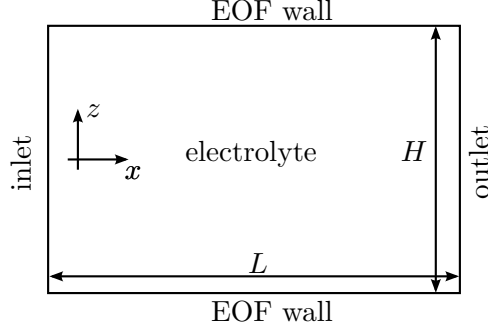


**Figure 4.1:** The rectangular computational domain  $\Omega$  of length  $L$  and height  $H$  for the EO-flow validation problem.

#### 4.2.1 Model

Consider the rectangular computational domain of length  $L$  and height  $H$  in Figure 4.1. The governing equation for the electrolyte are the Navier–Stokes equations given in the linear slip-velocity model in Equation (3.56). We assume steady-state and low Reynolds numbers, whereby the Stokes equations arise

$$0 = \partial_j \sigma_{ij}, \quad i = x, y, \quad (4.9)$$

where the viscous stress tensor is given by

$$\sigma_{ij} = -p\delta_{ij} + \partial_i v_j + \partial_j v_i. \quad (4.10)$$

In weak form notation the equation is

$$0 = \int_{\partial\Omega} v_i^{(t)} (\hat{n}_j \sigma_{ij}) \, ds - \int_{\Omega} (\partial_j v_i^{(t)}) \sigma_{ij} \, da, \quad (4.11)$$

where  $v_i^{(t)}$  are the matching hydrodynamic test functions. Correspondingly, the governing equation for the electric potential is given by Equation (3.57)

$$\nabla^2 \phi = 0. \quad (4.12)$$

In weak form notation this equation is

$$0 = \int_{\partial\Omega} \phi^{(t)} (\hat{n}_j \partial_j \phi) \, ds - \int_{\Omega} (\partial_j \phi^{(t)}) (\partial_j \phi) \, da, \quad (4.13)$$

where  $\phi^{(t)}$  is the test function to the electric potential.

### 4.2.2 Boundary conditions

For the hydrodynamic problem we assume stress-free flow at the in- and outlet

$$\hat{n}_j \sigma_{ij} = 0, \quad \text{at in- and outlet.} \quad (4.14)$$

At the EOF walls we apply the Helmholtz–Smoluchowski velocity from Equation (3.53) but in order to do this we need to introduce the reaction force  $\mathbf{f}$  (Lagrange multipliers) on the EOF walls  $\partial\Omega_{\text{EOF}}$  given by

$$f_i = \hat{n}_j \sigma_{ij}, \quad \text{on } \partial\Omega_{\text{EOF}}. \quad (4.15)$$

Furthermore, the part of the boundary integral that is on the EOF walls in Equation (4.11) needs to be rewritten

$$\int_{\partial\Omega_{\text{EOF}}} v_i^{(t)} (\hat{n}_j \sigma_{ij}) ds = \int_{\partial\Omega_{\text{EOF}}} v_i^{(t)} f_i ds + \int_{\partial\Omega_{\text{EOF}}} (v_{\text{hs},i} - v_i) f_i^{(t)} ds, \quad (4.16)$$

where  $f_i^{(t)}$  is the test functions corresponding to the reaction force and the Helmholtz–Smoluchowski velocity is

$$\mathbf{v}_{\text{hs}} = -\frac{\varepsilon\zeta}{\eta} (-\nabla_s \phi). \quad (4.17)$$

For the electrostatic potential we assume a constant potential  $\pm V_0/2$  at the in- and outlets, respectively

$$\phi = \pm \frac{V_0}{2}, \quad \text{at in- and outlet.} \quad (4.18)$$

Additionally, we assume no-charge on the EOF walls

$$\hat{n}_j \partial_j \phi = 0, \quad \text{at EOF walls.} \quad (4.19)$$

Finally, we assume a pressure free flow

$$p = 0, \quad \text{at in- and outlet.} \quad (4.20)$$

The COMSOL–MATLAB script for this problem is included in Appendix B.

### 4.2.3 Results

We use the parameters listed in Table 4.1 in our numerical simulation. Furthermore, we calculate the analytical EO velocity to

$$v_{\text{eo}} = 0.691 \text{ mm s}^{-1}. \quad (4.21)$$

As expected, our numerical results are in excellent agreement with the analytical electro-osmotic plug flow solution. Figure 4.2 (a) shows a plot of the numerically calculated EO-flow velocity field. Figure 4.2 (b) shows the relative difference between the numerical velocity profile and the analytical EO  $(v_x(z) - v_{\text{eo}})/v_{\text{eo}}$ . The relative deviation is on the order of  $10^{-13}$ , which shows that our numerical scheme is working properly.

**Table 4.1:** Parameters used in the calculation for the parallel plates EO-flow.

Symbol	Value	Symbol	Value
$H$	100 $\mu\text{m}$	$V_0$	10 V
$L$	1 mm	$\epsilon_r$	78
$\zeta$	-100 mV	$\eta$	1 mPa s

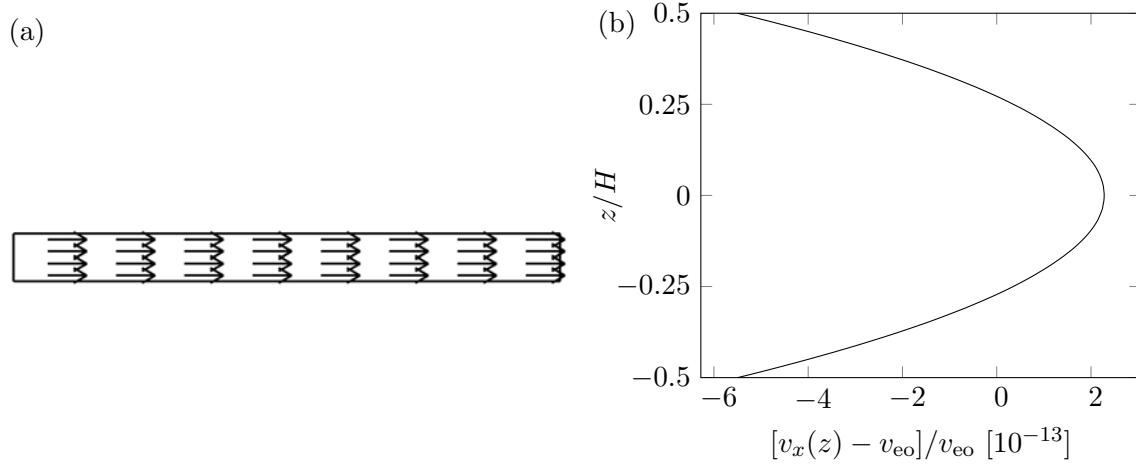


**Figure 4.2:** (a) Velocity plot of the numerically calculated EO-flow. Note that all the velocity arrows are parallel to the EOF walls. (b) Plot of the relative difference between the numerical and analytical EO-flow velocity. The relative difference is on the order of  $10^{-13}$ , which is a strong indication that our numerical implementation is valid.

## Chapter 5

# Numerical analysis of analyte transport across un-biased electrodes in microchannels

The original motivation for the current work is based on observations of charged species transport in microchannels containing un-biased electrodes. The observations were done by professor Sumita Pennathur, now at UCSB, but at the time of the initial observations also at the University of Twente in the Netherlands. Here she fabricated straight microchannels containing small metal geometries of different shapes so that the phenomenon could be systematically studied.

During the course of the current project the author visited the UCSB–Nanolab where the starting point was to utilize the microchannels for a more detailed investigation. This was done in close collaboration with students of professor Sumita Pennathur, in particular Jared Frey and Trevor Wolfscale. The work iterated toward the final setup which is the focus of this chapter; investigation of electrokinetic phenomena induced by the application of a potential difference to a buffer filled microchannel containing a simple rectangular metal structure and a fluorescence dye. We acquired data with optical epifluorescence microscopy and here we compare these observations to numerical simulations. In the numerical simulations we combine the full nonlinear model and linear slip-velocity models

### 5.1 Model system

The physical system is described in Chapter 2. For the numerical simulations we use a number of approximations of which the most important are: *(i)* the microchannel is modelled in the 2D  $xz$ -plane, see Figure 5.1. This is justified by the width-to-height ratio of 500 : 1 and necessary in terms of computational power. *(ii)* The electrode is modelled with zero height. In Chapter 6 we show that the finite height of an un-biased electrode can have a large impact on the flow solution if the height-to-width ratio of the electrode is more than 10%. For the current problem the height-to-width ratio is below one percent and we can safely ignore the finite height of the un-biased electrode. We define four types

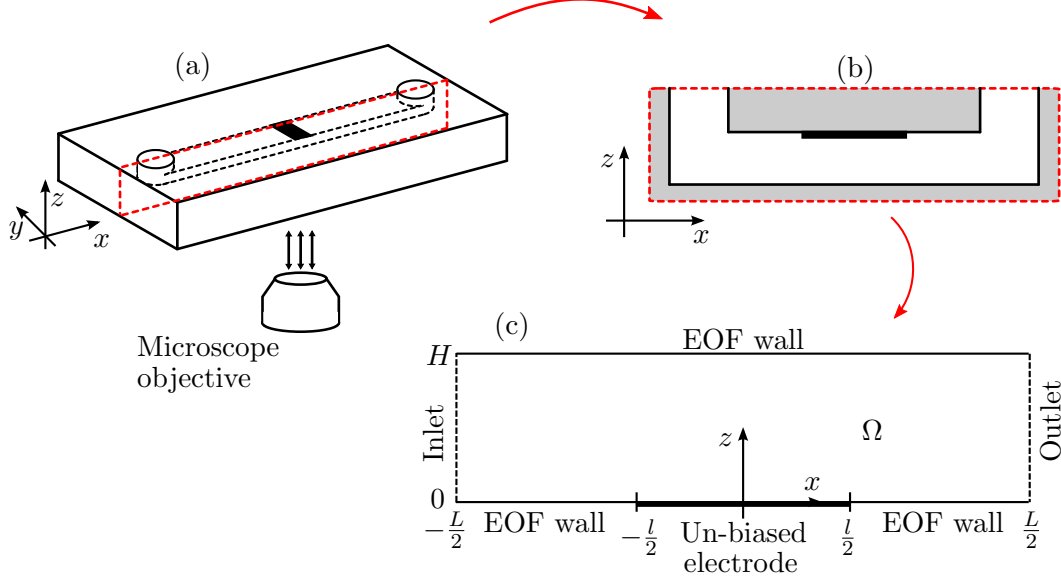


**Figure 5.1:** (a) The full 3D microchip. (b) The 2D cross-section with the un-biased electrode at the top wall. (c) The 2D computational domain  $\Omega$  with four boundary types; (i) inlet (dashed line), (ii) EOF walls (full, normal lines), (iii) un-biased electrode (full, thick line), and (iv) outlet (dashed line). We place our coordinate system in such a way that the un-biased electrode is at  $z = 0$  and  $-l/2 < x < l/2$ , and so  $\mathbf{e}_z$  points in the same direction as the surface normal  $\hat{\mathbf{n}}$  into the channel.

of different boundaries: inlet, EOF wall, un-biased electrode, and outlet, see Figure 5.1. The idea is to reduce the size of the problem by applying the linear slip-velocity model on the EOF walls, which constitute the major part of boundary in the domain. Then, we apply the full nonlinear model on the un-biased electrode in order to resolve the induced Debye layer. In our study we vary three parameters: (i) applied potential difference  $V_0$ , (ii) initial concentrations of positive  $c_0^{(+)}$  and negative  $c_0^{(-)}$  buffer ions, and (iii) initial concentration of dye  $c_0^{(d)}$ . Table 5.1 shows the specific values we use. It has for numerical reasons not been possible to use the concentrations mentioned in the experimental part in Chapter 2. As the concentrations get higher, the Debye–Hückel screening length gets

**Table 5.1:** Values used for the variable parameters.

Symbol	Values					
$c_0^{(\pm)}$	10 $\mu\text{M}$	100 $\mu\text{M}$	-	-	-	-
$c_0^{(d)}$	1 $\mu\text{M}$	10 $\mu\text{M}$	-	-	-	-
$V_0$	5 V	10 V	15 V	20 V	25 V	30 V

**Table 5.2:** Values of the constant parameters.

Symbol	Value	Symbol	Value
$D^{(\pm)}$	$2 \times 10^{-9} \text{ m}^2 \text{ s}^{-1}$	$Z^{(\pm)}$	$\pm 1$
$D^{(\text{d})}$	$8.8 \times 10^{-10} \text{ m}^2 \text{ s}^{-1}$	$Z^{(\text{d})}$	$-1$
$L$	9 mm	$\eta$	1 mPa s
$H$	0.5 $\mu\text{m}$	$\rho_{\text{b}}$	$10^3 \text{ kg m}^3$
$l$	60 $\mu\text{m}$	$\varepsilon_{\text{r}}$	78
$\zeta$	-100 mV	$T$	293.15 K

smaller

$$\lambda_D = \sqrt{\frac{\varepsilon k_{\text{B}} T}{e^2 \sum_i [Z^{(i)}]^2 c_0^{(i)}}}. \quad (5.1)$$

Hence, since we resolve the double layer on the un-biased electrode, we get numerical convergence problems for too high concentrations. The same issue is true for high applied potential differences which explains why the values in Table 5.1 are lower than mentioned in Chapter 2. Furthermore, the valences of the different ionic species we model are for the positive and negative buffer ions  $|Z^{(\pm)}| = 1$ . Instead of introducing two additional species for the fluorescence dye we simple model the fluorescent active component and assign it a valence  $Z^{(\text{d})} = -1$ . In practice, we achieve electro-neutrality in our system by specifying the initial concentrations of the negative buffer ion  $c_0^{(-)}$  and of the dye  $c_0^{(\text{d})}$  and then calculate the initial concentration of the positive buffer ion by

$$c_0^{(+)} = c_0^{(-)} + c_0^{(\text{d})}, \quad (5.2)$$

which means the positive buffer ion concentration  $c_0^{(+)}$  listed in Table 5.1 has to be corrected by this calibration for the positive buffer ion. We also assign values for the buffer diffusivities  $D^{(\pm)}$ , the dye diffusivity  $D^{(\text{d})}$ , the length of the un-biased electrode  $l$ , the length  $L$  and height  $H$  of the microchannel, the zeta potential  $\zeta$ , the dynamic viscosity  $\eta$ , the buffer mass-density  $\rho_{\text{b}}$ , the relative permittivity  $\varepsilon_{\text{r}}$ , and the temperature  $T$ . The constant parameters are listed in Table 5.2 We implement the governing equations from the full nonlinear model in Chapter 3 in the computational domain  $\Omega$ .

## 5.2 Boundary conditions

At the inlet we assume the normal derivative of the  $x$ -component of the velocity  $v_x$ , the  $z$ -component of the velocity  $v_z$ , and the pressure to be zero. Also, we assume a constant electric potential, and constant concentrations

$$\partial_x v_x = 0, \quad v_z = 0, \quad p = 0, \quad \phi = \frac{V_0}{2}, \quad c^{(\pm)} = c_0^{(\pm)}, \quad c^{(\text{d})} = c_0^{(\text{d})}, \quad \text{at inlet.} \quad (5.3)$$

At the outlet we have identical boundary conditions except for the electric potential

$$\partial_x v_x = 0, \quad v_z = 0, \quad p = 0, \quad \phi = -\frac{V_0}{2}, \quad c^{(\pm)} = c_0^{(\pm)}, \quad c^{(d)} = c_0^{(d)}, \quad \text{at outlet.} \quad (5.4)$$

At the EOF walls we assume the  $x$ -component of the velocity to be given by the Helmholtz–Smoluchowski velocity, the  $z$ -component of the velocity to be zero, no-charge density, and no particle current

$$v_x = -\frac{\varepsilon\zeta}{\eta}(-\partial_x \phi), \quad v_z = 0, \quad \partial_z \phi = 0, \quad J_z^{(\pm)} = 0, \quad J_z^{(d)} = 0, \quad \text{at EOF walls.} \quad (5.5)$$

Finally, at the un-biased electrode we assume no-slip, constant electric potential, and no particle current

$$v_x = 0, \quad v_z = 0, \quad \phi = \text{const.}, \quad J_z^{(\pm)} = 0, \quad J_z^{(d)} = 0, \quad \text{at un-biased electrode.} \quad (5.6)$$

### 5.3 Initial conditions

For numerical reasons, we start the simulation at the time  $t_0 = -10^{-10}$  s where we specify a zero velocity field, zero pressure, zero electric potential, and initial concentrations of the ionic species as given in Table 5.1

$$v_x = 0, \quad v_z = 0, \quad p = 0, \quad \phi = 0, \quad c^{(\pm)} = c_0^{(\pm)}, \quad c^{(d)} = c_0^{(d)}, \quad \text{in } \Omega \text{ at } t = t_0. \quad (5.7)$$

It is not until  $t = 0$  we apply the potential difference  $V_0$  across the channel, which means the boundary conditions for the electric potential in Equations (5.3) and (5.4) are modified to

$$\phi = 0, \quad \text{at in- and outlet for } t_0 < t < 0. \quad (5.8)$$

We use some of COMSOLs numerical techniques to implement the problem as described in the next section.

## 5.4 Numerics in COMSOL

### 5.4.1 Constant potential on the un-biased electrode

We implement the constant potential on the un-biased electrode using COMSOLs so-called coupling variable. Essentially, we define a point at  $(x, z) = (0, 0)$  where COMSOL probes the electric potential and makes this value available in the calculation. We then apply this value as a Dirichlet condition on the potential on the entire un-biased electrode

$$\phi(x, 0) = \phi(0, 0), \quad \text{on the un-biased electrode.} \quad (5.9)$$

The advantage of this procedure is a higher degree of numerical stability than if we impose the boundary condition through a zero tangential derivative  $\partial_x \phi = 0$  on the un-biased electrode.



### 5.4.2 Logarithmic concentration fields

Another issue is the extreme values of the concentration fields that can occur in the simulation. For high externally applied voltages there is a large degree of charge separation on the un-biased electrode making the concentrations of the charged species go to zero or to very high values. This gap in concentration values can be somewhat close by making a logarithmic transformation of the concentration fields

$$c^{(i)}(x, z) = c_n^{(i)} \exp \left[ \check{c}^{(i)}(x, z) \right], \quad i = +, -, d, \quad (5.10)$$

where  $\check{c}^{(i)} = \check{c}^{(i)}(x, z)$  is the transformed field and  $c_n^{(i)}$  is a normalization constant ( $[c_n^{(i)}] = \text{m}^{-3}$ ). This procedure makes the solution more smooth at the expense of more nonlinearity in the governing equations. The governing equations for the transformed fields are

$$\partial_t \check{c}^{(i)} + \nabla \check{c}^{(i)} \cdot \check{\mathbf{J}}^{(i)} + \nabla \cdot \check{\mathbf{J}}^{(i)} + \mathbf{v} \cdot \nabla \check{c}^{(i)} = 0, \quad (5.11)$$

where the pseudo-particle-current-density is

$$\check{\mathbf{J}}^{(i)} = -D^{(i)} \left[ \nabla \check{c}^{(i)} + \frac{Z^{(i)} e}{k_B T} \nabla \phi \right]. \quad (5.12)$$

Correspondingly, the charge density changes to

$$\rho_{\text{el}} = e \sum_i Z^{(i)} c_0^{(i)} \exp \left[ \check{c}^{(i)} \right], \quad (5.13)$$

but otherwise the governing equations are unchanged. The Dirichlet boundary- and the initial-conditions  $c^{(i)} = c_0^{(i)}$  for the logarithmically transformed fields are

$$\check{c}^{(i)} = \ln \left( \frac{c_0^{(i)}}{c_n^{(i)}} \right), \quad \text{at in- and outlet}, \quad (5.14a)$$

$$\check{c}^{(i)} = \ln \left( \frac{c_0^{(i)}}{c_n^{(i)}} \right), \quad \text{at } t = t_0. \quad (5.14b)$$

Note, that convergence problems can occur if  $c_n^{(i)} = c_0^{(i)}$ , despite that this choice seems like the most natural one. Hence, we use  $c_n^{(i)} = 1 \text{ m}^{-3}$ . The Neumann boundary conditions are expressed as before, in terms of the pseudo-particle-current-density (essentially due to the no-slip boundary conditions)

$$\hat{\mathbf{n}} \cdot \check{\mathbf{J}}^{(i)} = 0, \quad \text{at EOF walls and un-biased electrode.} \quad (5.15)$$

At the end of our simulations we apply the inverse of the transformation in Equation (5.10) to get back to the physical concentration fields.

## 5.5 Results

We solve the model transiently from the equilibrium situation at time  $t_0 = -10^{-10}$  s just before the external voltage is applied at  $t = 0$  to the time  $t = 10^4$  s to be absolutely sure steady-state has set in (which we verify by looking at combined temporal and spatial plots for the fields in the simulation). We then plot the normalized concentration of the dye  $c^{(d)}(x, z)/c_0^{(d)}$  along the bottom wall i.e. along the line  $(x, 0)$ . However, the microscope only sees a limited part of the microchannel, and for this reason we can only compare with the experimental results in a relatively small region around the un-biased electrode i.e.  $-400 \mu\text{m} < x < 400 \mu\text{m}$ . The results are grouped according to the available experimental data into four categories (*i*) low buffer and low dye concentration Figure 5.2 (a) and (b), (*ii*) low buffer and high dye concentration Figure 5.2 (c) and (d), (*iii*) high buffer and low dye concentration Figure 5.3 (a) and (b), and (*iv*) high buffer and high dye concentration Figure 5.3 (c) and (d). Furthermore, we plot the corresponding experimental results next to the numerical results for comparison. However, the experimentally observed upstream  $x < 0$  intensity levels vary with applied voltage. Hence, for the sake of comparing intensity drops in between data series, we normalize the intensity  $I_x(x)$  (defined in Equation (2.16) on page 16) for each applied voltage with its upstream intensity level, in order to get an intensity  $I_x^*(x)$  with a common upstream reference level of unity

$$I_x^*(x) = \frac{I_x(x)}{I_x(x_0)}, \quad x_0 < -\frac{l}{2}, \quad (5.16)$$

as seen in the figures.

We observe a number of characteristic features in our numerical results that are in accordance with the experimental observations: (*i*) a concentration drop in the dye across the un-biased electrode, (*ii*) the drop increases with increasing applied voltage, (*iii*) the drop is affected by the concentration of buffer and dye, and (*iv*) high concentration enrichment of dye on the un-biased electrode. In the next section we discuss the possible mechanisms behind the phenomena.

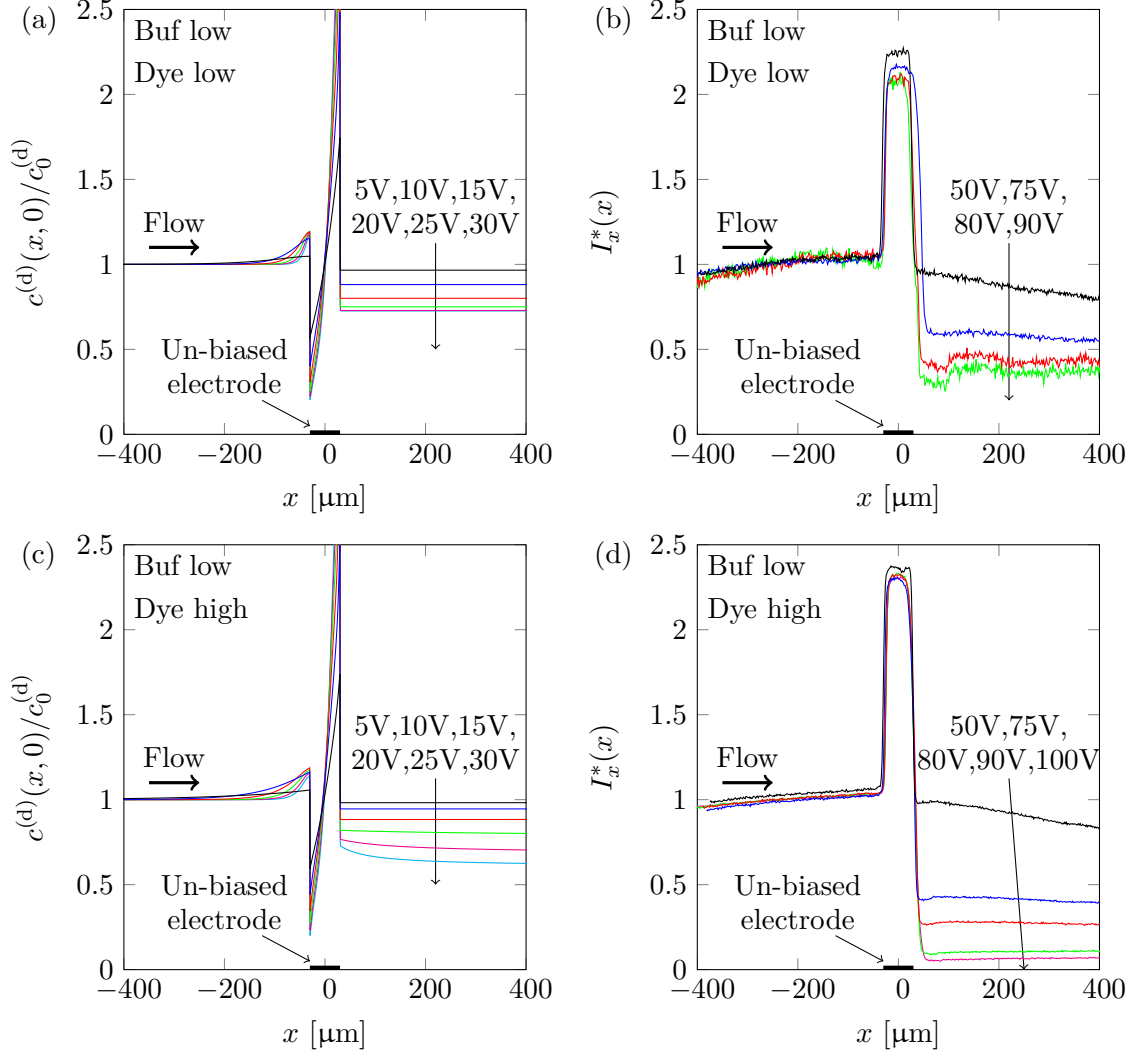


**Figure 5.2:** Concentration drop across the un-biased electrode in steady-state for several applied voltages for the low buffer concentrations. **(a) and (c): Numerical simulations;** plot of  $c^{(d)}(x, 0)$  for six applied voltages in the range  $V_0 = 5 \text{ V} - 30 \text{ V}$  with negative buffer ion concentration  $c_0^{(-)} = 10 \mu\text{M}$ . The positive buffer ion  $c_0^{(+)}$  and dye  $c_0^{(d)}$  concentrations are in (a)  $11 \mu\text{M}$  and  $1 \mu\text{M}$ , and in (c)  $20 \mu\text{M}$  and  $10 \mu\text{M}$ . **(b) and (d): Experimental observations;** plot of the normalized and averaged intensity  $I_x^*(x)$  for four and five applied voltages in the range  $V_0 = 50 \text{ V} - 100 \text{ V}$  with phosphate buffer concentration  $[\text{Na}_2\text{HPO}_4] = 1 \text{ mM}$ . The concentration of BODIPY dye [BNa] is in (b)  $1 \mu\text{M}$ , and in (d)  $10 \mu\text{M}$ .

## 5.6 Discussion

We imagine that the induced concentration drop in essence can be explained by the asymmetry in the problem caused by the left-to-right-going EO-flow. To explain this hypothesis, first note the electric potential in Figure 5.4. At  $t = 0.01 \text{ s}$  immediately after the voltage

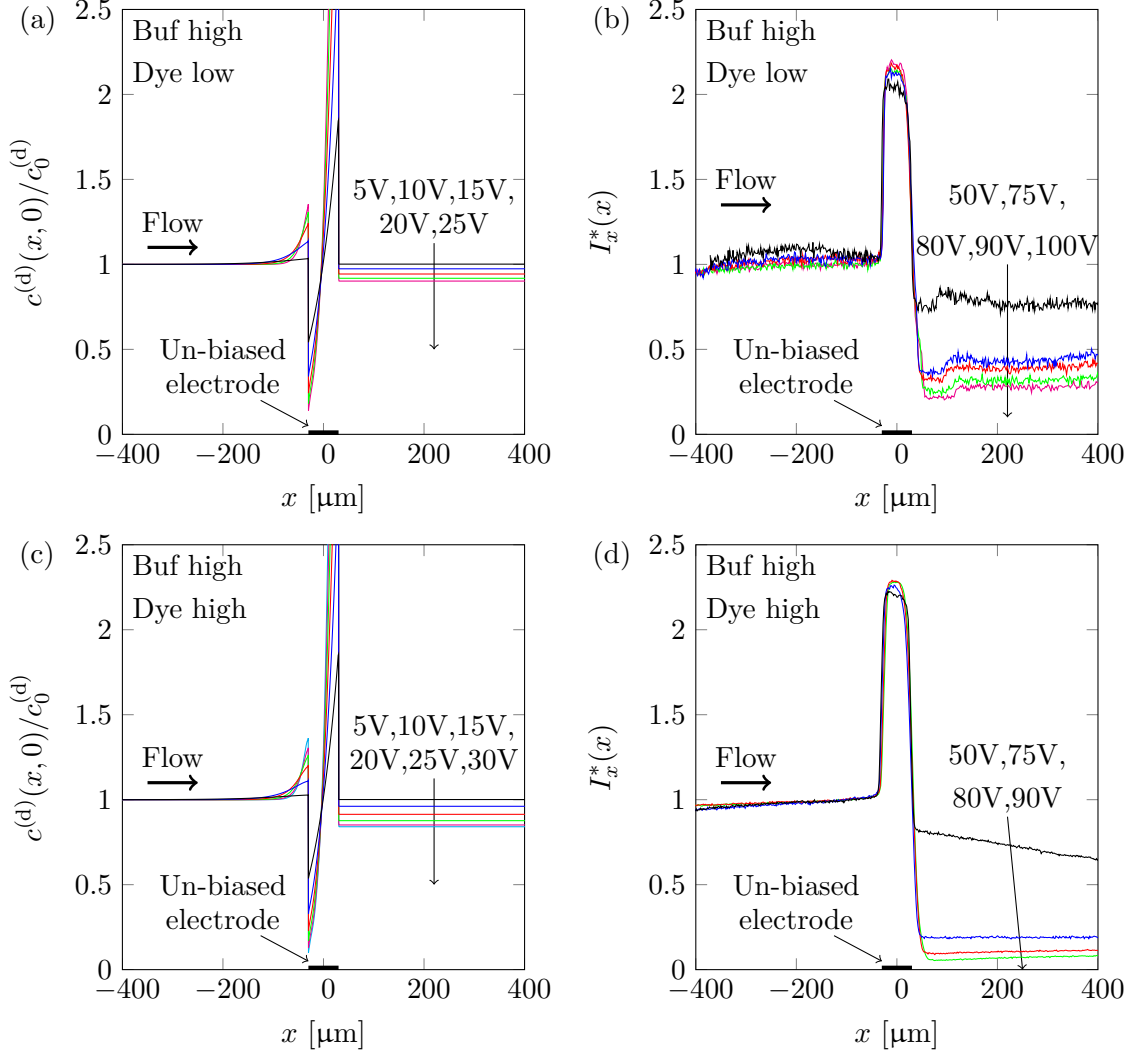


**Figure 5.3:** Concentration drop across the un-biased electrode in steady-state for several applied voltages for the high buffer concentrations. **(a) and (c): Numerical simulations;** plot of  $c^{(d)}(x, 0)/c_0^{(d)}$  for six applied voltages in the range  $V_0 = 5 \text{ V} - 30 \text{ V}$  with negative buffer ion concentration  $c_0^{(-)} = 100 \mu\text{M}$ . The positive buffer ion  $c_0^{(+)}$  and dye  $c_0^{(d)}$  concentrations are in (a)  $101 \mu\text{M}$  and  $1 \mu\text{M}$ , and in (c)  $110 \mu\text{M}$  and  $10 \mu\text{M}$ . **(b) and (d): Experimental observations;** plot of the normalized and averaged intensity  $I_x^*(x)$  for five and four applied voltages in the range  $V_0 = 50 \text{ V} - 100 \text{ V}$  with phosphate buffer concentration  $[\text{Na}_2\text{HPO}_4] = 10 \text{ mM}$ . The concentration of BODIPY dye [BNa] is in (b)  $1 \mu\text{M}$ , and in (d)  $10 \mu\text{M}$ .

difference  $V_0$  has been applied  $\phi$  is antisymmetric around  $x = 0$ . However, in steady-state  $t = 10000 \text{ s}$  we see an increase in the potential and the antisymmetry is broken. Essentially, the potential still varies linearly within the up- and downstream segments of the channel, but it has a kink at the un-biased electrode, see Figure 5.4 (a). It follows, that the Helmholtz-Smoluchowski slip velocity Equation (3.53) is larger in magnitude in the

downstream segment than in the upstream segment. Consequently, due to the continuity of the fluid a negative counterpressure is build up inside the channel which creates a pressure driven flow that exactly cancels the imbalance between the up- and downstream EO-flow rates, see Figure 5.4 (b), (c), (d) and (e). Also, we plot the electric charge density  $\rho_{el}(x, z)$  on the electrode surface and see a symmetry-break in steady-state, see Figure 5.5 (a). Due to vertical confinement the Debye layer spans a considerable amount of the microchannel cross-section, and hence the charge density is subjected to a relatively big convective force. We believe this convection distorts the charge density whereby a highly complex and coupled interaction between flow, electrode and charge density occurs, see Figure 5.5 (b). Consequently, for the parameters in this study, the result is a concentration drop in charged species across the un-biased electrode.

We explain the quantitative differences between the experimental and numerical observed concentration drops in terms of two main complications: (i) the difference in applied voltages between numerical simulations and experiments, and (ii) fluorescence effects.

First, we are not able to apply similarly high voltages in the numerical simulations as in the experiments. The potential drop across the un-biased electrode ranges from 300 mV–600 mV in our experiments which is high above the thermal voltage of 25 mV. Consequently, our experiments are conducted in a highly nonlinear regime where we can imagine a number of effects that our continuum model is unable to capture. However, in our simulations the potential drop across the un-biased electrode is 30 mV–200 mV, which confirm that our numerical implementation is able to successfully solve highly nonlinear electrokinetic problems.

Secondly, there is no guarantee that the experimentally observed fluorescence intensity is directly proportional to the concentration of dye. The intensity is not only a function of concentration, also fading and chemical interactions play a role. Fading is a process in which the fluorescence intensity decreases as a function of illumination time. Though, it is difficult to estimate if this process has a large influence on the observations. Furthermore, we imagine that the BODIPY dye might be affected by the large concentrations and the high potential drop in the vicinity of the un-biased electrode. Some of the BODIPY molecules might form complexes that do not fluoresce, thus making the apparent concentration drop seem larger. Regardless, the results are so systematic that we are confident that our numerical simulations are able to explain part of the mechanism behind the observed concentration drop.

## 5.7 Conclusion

In conclusion, we are able to qualitatively reproduce the experimental observations with our numerical model. Furthermore, from our results we are able to give some insight into the dynamics of the phenomenon. Basically, the symmetry breaking, left-to-right-going EO-flow from the microchannel-walls exerts a convective force on the finite charge-distribution in the Debye-layer on the un-biased electrode. This in turn gives rise to further coupled and complex interactions between the flow, the charge density, and the un-biased electrode. The result is the observed concentration drop. Future and more detailed studies

might reveal in more detail the physical processes leading to the concentration drop.

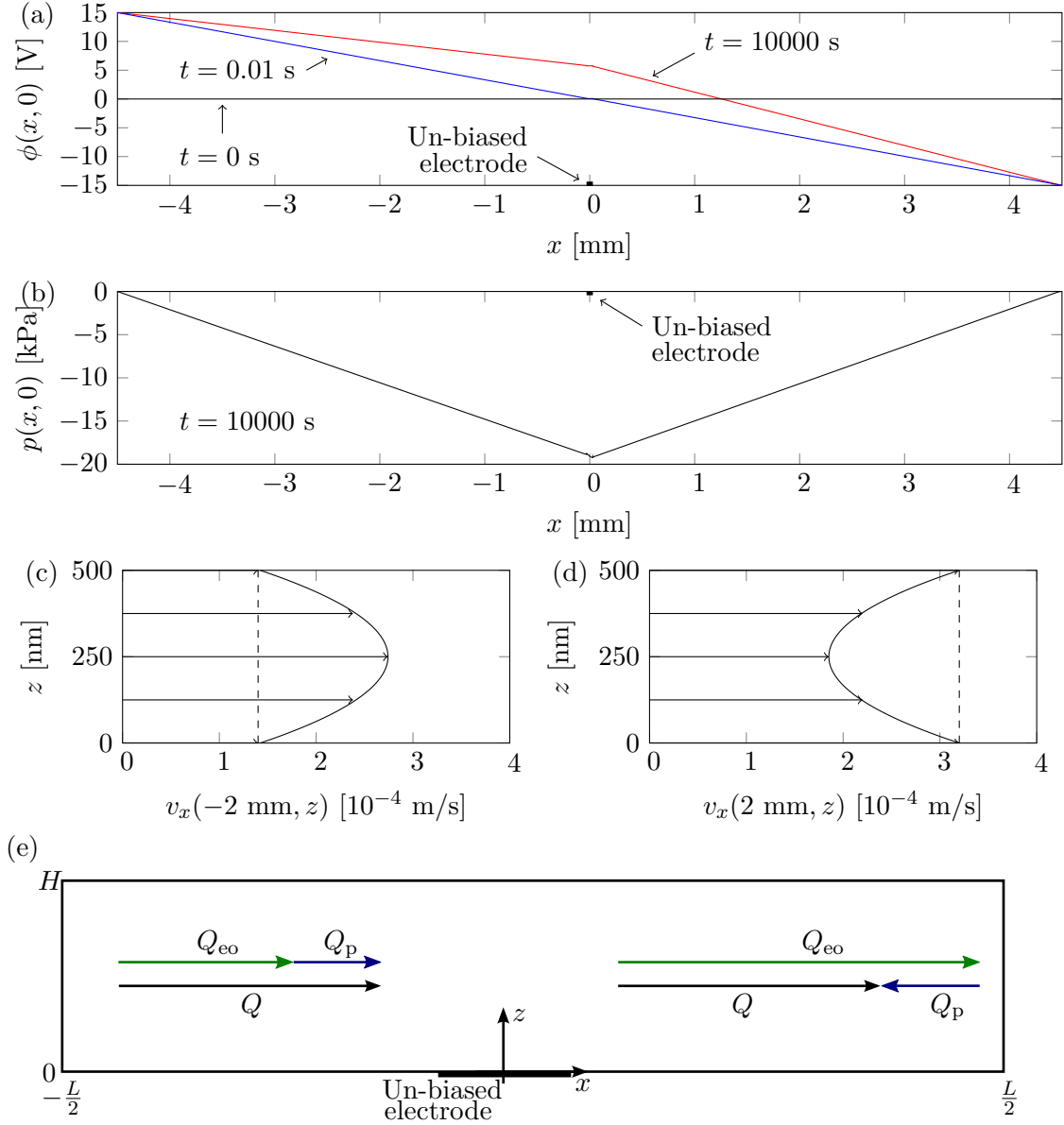


**Figure 5.4:** Sequence of figures based on numerical simulations for  $c_0^{(-)} = 10 \mu\text{M}$ ,  $c_0^{(+)} = 11 \mu\text{M}$ , and  $c_0^{(d)} = 1 \mu\text{M}$  at  $V_0 = 30 \text{ V}$ . (a) Plot of the electric potential along the bottom wall  $\phi(x, 0)$  for three times  $t = \{0 \text{ s}, 0.01 \text{ s}, 10000 \text{ s}\}$ . Note, at  $t = 10000 \text{ s}$  the potential on the un-biased electrode is increased to  $\phi(0, 0) \approx 5 \text{ V}$ . Consequently, the electric field has a larger magnitude for  $x > 0$  and thus the EO-flow will be larger here than the EO-flow for  $x < 0$ . (b) Plot of the pressure for  $t = 10000 \text{ s}$ . This pressure creates a flow that balances out the flow rate difference in the up- and downstream EO-flows. (c) and (d) Velocity profiles at up- and downstream positions  $v_x(\pm 2 \text{ mm}, z)$ . The dashed line indicates a division of the profiles into a contributions purely from EO- and pressure-flow, respectively. In the upstream segment (c)  $x < 0$  both the EO- and pressure-flow is to the right, whereas in the downstream segment (d)  $x > 0$  the EO- and pressure flows are to the right and left, respectively. (e) Sketch showing how the EO-flow rate  $Q_{eo}$  is increased for  $x < 0$  and decreased for  $x > 0$  by a pressure driven flow rate  $Q_p$ , so as to make the total flow rate  $Q$  constant in the channel.

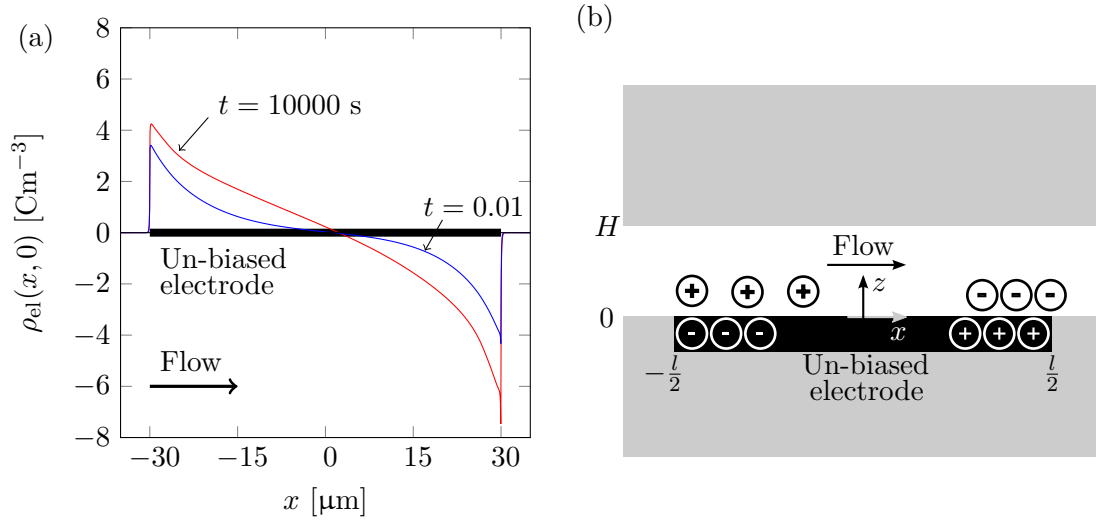


**Figure 5.5:** (a) Plot of the charge density on the electrode  $\rho_{el}(x, 0)$  for the same parameters as in Figure 5.4. Note, the distribution of the charge density across the electrode goes from almost anti-symmetric  $t = 0.01$  s to distorted  $t = 10000$  s due to the influence of convection from the left-to-right going EO-flow. (b). Sketch of the charge on the electrode at steady-state  $t = 10000$  s. The Debye-length is significant compared to the channel height, and hence a large part of the charge in the double layer feels the convection from the left-to-right going EO-flow. Consequently, the charge distribution is distorted in a non-trivial way and this ultimately causes the shift from zero to positive potential on the electrode as seen in Figure 5.4 (a).



## Chapter 6

# Numerical analysis of finite Debye-length effects in induced-charge electro-osmosis

In this chapter a microchamber filled with a binary electrolyte and containing a flat unbiased center electrode at one wall, is subjected to the three numerical models to study the strength of the resulting ICEO flow rolls: (*i*) the full nonlinear continuum model resolving the double layer, (*ii*) the linear slip-velocity model not resolving the double layer and without tangential charge transport inside this layer, and (*iii*) the nonlinear slip-velocity model extending the linear model by including the tangential charge transport inside the double layer. The latter two models are only strictly valid for infinitely thin double layers, and it is shown to which extent they reproduce the results of the full nonlinear model.

We show that compared to the full model, the slip-velocity models significantly overestimate the ICEO flow. This provides a partial explanation of the quantitative discrepancy between observed and calculated ICEO velocities reported in the literature. The discrepancy increases significantly for increasing Debye length relative to the electrode size, i.e. for nanofluidic systems. However, even for electrode dimensions in the micrometer range, the discrepancies due to the finite Debye length can be more than 10% for an electrode of zero height and more than 100% for electrode heights comparable to the Debye length.

### 6.1 Introduction

In spite of the growing interest in the literature not all aspects of the EO-flow-generating mechanisms have been explained so far. While qualitative agreement is seen between theory and experiment, quantitative agreement is often lacking as reported by Gregersen *et al.* [19], Harnett *et al.* [26], and Soni *et al.* [21]. The present chapter seeks to illuminate some of the possible reasons underlying these observed discrepancies.

Squires *et al.* [27] have presented an analytical solution to the ICEO flow problem around a metallic cylinder using a linear slip-velocity model in the two dimensional plane perpendicular to the cylinder axis. The discrepancy between this analytical result and a

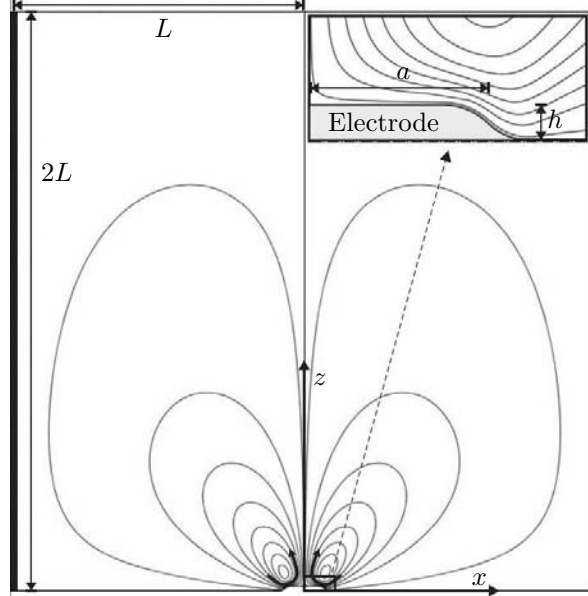


**Figure 6.1:** A sketch of the square  $2L \times 2L$  electrolytic microchamber in the  $xz$ -plane. The external voltage is applied to the two electrodes (thick black lines) at  $x = \pm L$ . It induces two counter-rotating flow rolls (curved black arrows) by electro-osmosis over the un-biased metallic center electrode of length  $2a$  and height  $h$  placed at the bottom wall around  $(x, z) = (0, 0)$ . The spatial extent of the flow rolls is represented by the streamline plot (thin black curves) drawn as equidistant contours of the flow rate. The inset is a zoom-in on the right half,  $0 < x < a$ , of the un-biased center electrode and the nearby streamlines.

numerical solution of the full equation system, where the double layer is fully resolved, has become the primary motivation for the study presented in this chapter.

## 6.2 Model system

To keep the analysis simple, a single un-biased metallic electrode in a uniform, external electric field is considered. The electrode of width  $2a$  and height  $h$  is placed at the bottom center,  $-a < x < a$  and  $z = 0$ , of a square  $2L \times 2L$  domain in the  $xz$ -plane filled with an electrolyte, see Figure 6.1. The system is unbounded and translational invariant in the perpendicular  $y$ -direction. The uniform electric field, parallel to the surface of the center electrode, is provided by biasing the driving electrodes placed at the edges  $x = \pm L$  with the DC voltages  $\mp V_0$ , respectively. This anti-symmetry in the bias voltage ensures that the constant potential of the center electrode is zero. A double layer, or a Debye screening layer, is induced above the center electrode, and an ICEO flow is generated consisting of two counter-rotating flow rolls. Electric insulating walls at  $z = 0$  (for  $|x| > a$ ) and at  $z = 2L$  confine the domain in the  $z$ -direction. The symmetry of the system around  $x = 0$  is exploited in the numerical calculations.

## 6.3 Full nonlinear model (FN)

### 6.3.1 Dimensionless form

To simplify the numerical implementation, we rewrite the governing equations from Section 3.2 in dimensionless form, using the characteristic parameters of the system: The geometric half-length  $a$  of the electrode, the ionic concentration  $c_0$  of the bulk electrolyte, and the thermal voltage  $\phi_0 = k_B T / (Ze)$ . The characteristic zeta-potential  $\zeta$  of the center electrode, i.e. its induced voltage, is given as the voltage drop along half of the electrode,  $\zeta = (a/L)V_0$ , and the dimensionless zeta-potential  $\alpha$  is introduced as  $\zeta \equiv \alpha\phi_0$ , or  $\alpha = (aV_0)/(L\phi_0)$ . The characteristic velocity  $v_0$  is chosen as the Helmholtz–Smoluchowski slip velocity induced by the local electric field  $E = \zeta/a$ , and finally the pressure scale is set by the characteristic microfluidic pressure scale  $p_0 = \eta v_0/a$ . In summary,

$$\phi_0 = \frac{k_B T}{Ze}, \quad v_0 = \frac{\varepsilon \zeta}{\eta a} = \frac{\varepsilon \phi_0^2}{\eta a} \alpha^2, \quad p_0 = \frac{\eta v_0}{a}. \quad (6.1)$$

The new dimensionless variables (denoted by a tilde) thus become

$$\tilde{\mathbf{r}} = \frac{\mathbf{r}}{a}, \quad \tilde{c}^{(i)} = \frac{c^{(i)}}{c_0}, \quad \tilde{\phi} = \frac{\phi}{\phi_0}, \quad \tilde{\mathbf{v}} = \frac{\mathbf{v}}{v_0}, \quad \tilde{p} = \frac{p}{p_0}. \quad (6.2)$$

To exploit the symmetry of the system, the governing equations are reformulated in terms of the average ion concentration  $c \equiv (c^{(+)} + c^{(-)})/2$  and half the charge density  $\rho \equiv (c^{(+)} - c^{(-)})/2$ . Correspondingly, the average ion current density  $\mathbf{J}^{(c)} = (\mathbf{J}^{(+)} + \mathbf{J}^{(-)})/2$  and half the charge current density  $\mathbf{J}^{(\rho)} = (\mathbf{J}^{(+)} - \mathbf{J}^{(-)})/2$  are introduced. Thus, the resulting full system of coupled nonlinear equations takes the following form for the ionic fields

$$\tilde{\nabla} \cdot \tilde{\mathbf{J}}^{(c)} = \tilde{\nabla} \cdot \tilde{\mathbf{J}}^{(\rho)} = 0, \quad (6.3a)$$

$$\tilde{\mathbf{J}}^{(c)} = -\tilde{\rho} \tilde{\nabla} \tilde{\phi} - \tilde{\nabla} \tilde{c} + P\tilde{e} \tilde{c} \tilde{\mathbf{v}}, \quad (6.3b)$$

$$\tilde{\mathbf{J}}^{(\rho)} = -\tilde{c} \tilde{\nabla} \tilde{\phi} - \tilde{\nabla} \tilde{\rho} + P\tilde{e} \tilde{\rho} \tilde{\mathbf{v}}, \quad (6.3c)$$

$$P\tilde{e} = \frac{v_0 a}{D}, \quad (6.3d)$$

while the electric potential obeys

$$\tilde{\nabla}^2 \tilde{\phi} = -\frac{1}{\epsilon} \tilde{\rho}, \quad (6.4)$$

and finally the fluid fields satisfy

$$\tilde{\nabla} \cdot \tilde{\mathbf{v}} = 0, \quad (6.5a)$$

$$Re(\tilde{\mathbf{v}} \cdot \tilde{\nabla}) \tilde{\mathbf{v}} = -\tilde{\nabla} \tilde{p} + \tilde{\nabla}^2 \tilde{\mathbf{v}} - \frac{\tilde{\rho}}{\epsilon^2 \alpha^2} \tilde{\nabla} \tilde{\phi}, \quad (6.5b)$$

$$Re = \frac{\rho v_0 a}{\eta}. \quad (6.5c)$$

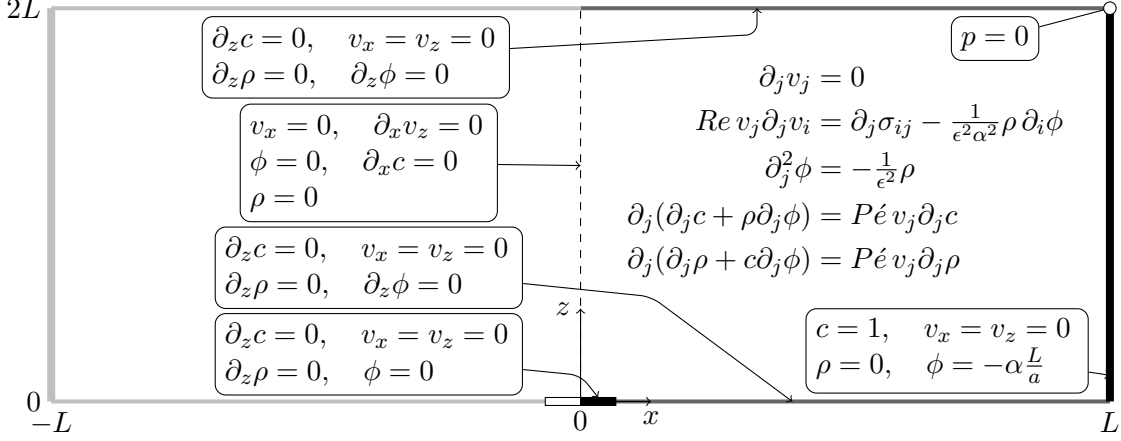


**Figure 6.2:** The governing equations (without box) and boundary conditions (with boxes, arrows points to specific boundaries) for the full continuum model in dimensionless form (the tilde is omitted for clarity) for the entire quadratic  $2L \times 2L$  domain (not shown in correct aspect ratio) bisected into two symmetric halves. Only the right half ( $x > 0$ ) of the domain is included in the simulations. The boundaries are; surface of the un-biased center electrode (black rectangle), solid insulating walls (dark gray), external electrode (black, thick line), and symmetry line (dashed dark gray).

Here the small dimensionless parameter  $\epsilon = \lambda_D/a$  has been introduced

$$\epsilon = \frac{\lambda_D}{a} = \frac{1}{a} \sqrt{\frac{\epsilon k_B T}{2(Ze)^2 c_0}}. \quad (6.6)$$

### 6.3.2 Boundary conditions

The symmetry around  $x = 0$  is exploited by only considering the right half ( $0 < x < L$ ) of the domain, see Figure 6.2. The three models employed here have the same boundary conditions, except on the un-biased electrode; hence, only on this boundary will there be differences between the three models. As boundary conditions on the driving electrode both ion concentrations are taken to be constant and equal to the bulk charge neutral concentration. Correspondingly, the charge density is set to zero. Consequently, all dynamics taking place on the driving electrode is ignored and it is simply treated as an equipotential surface with the value  $V_0$ . A no-slip condition for the fluid velocity is assumed, and thus at  $x = L$

$$\tilde{c} = 1, \quad \tilde{\rho} = 0, \quad \tilde{\phi} = -\frac{V_0}{\phi_0} = -\alpha \frac{L}{a}, \quad \tilde{\mathbf{v}} = \mathbf{0}. \quad (6.7)$$

On the symmetry axis ( $x = 0$ ) the potential and the charge density must be zero due to the anti-symmetry of the applied potential. Moreover, there is neither a fluid flux nor a net ion flux in the normal direction and the shear stresses vanish. Thus, at  $x = 0$

$$\tilde{\phi} = 0, \quad \hat{\mathbf{n}} \cdot \tilde{\mathbf{J}}^{(c)} = 0, \quad \tilde{\rho} = 0, \quad (6.8a)$$

$$\hat{\mathbf{t}} \cdot \tilde{\boldsymbol{\sigma}} \cdot \hat{\mathbf{n}} = 0, \quad \hat{\mathbf{n}} \cdot \tilde{\mathbf{v}} = 0, \quad (6.8b)$$

where  $\hat{\mathbf{t}}$  is the tangential unit vector which in 2D, contrary to 3D, are uniquely defined. On the solid, insulating walls there are no fluxes in the normal direction, the normal component of the electric field vanishes and there are no-slip on the fluid velocity

$$\hat{\mathbf{n}} \cdot \tilde{\mathbf{J}}^{(c)} = 0, \quad \hat{\mathbf{n}} \cdot \tilde{\mathbf{J}}^{(\rho)} = 0, \quad \hat{\mathbf{n}} \cdot \tilde{\nabla} \tilde{\phi} = 0, \quad \tilde{\mathbf{v}} = \mathbf{0}. \quad (6.9)$$

On the un-biased electrode the constant potential is zero due to symmetry and the fluid velocity obeys a no-slip condition. Additionally, there are no fluxes in the normal direction

$$\hat{\mathbf{n}} \cdot \tilde{\mathbf{J}}^{(c)} = 0, \quad \hat{\mathbf{n}} \cdot \tilde{\mathbf{J}}^{(\rho)} = 0, \quad \tilde{\phi} = 0, \quad \tilde{\mathbf{v}} = \mathbf{0}. \quad (6.10)$$

A complete overview of the governing equations and boundary conditions (on the un-biased electrode only for the full continuum model) is given in Figure 6.2.

### 6.3.3 The strongly nonlinear regime

As Chapter 5 we employ a logarithmic transformation of the concentration fields,  $\check{c}^{(\pm)} = \ln(c^{(\pm)}/c_0)$ . By inserting

$$c^{(\pm)} = c_0 \exp \left[ \check{c}^{(\pm)} \right] \quad (6.11)$$

in the governing equations a new, equivalent set of governing equations is derived. Again, the symmetry is exploited by defining the symmetric  $\check{c} = \check{c}^{(+)} + \check{c}^{(-)}$  and antisymmetric  $\check{\rho} = \check{c}^{(+)} - \check{c}^{(-)}$  combinations of the logarithmic fields and the corresponding formulation of the governing equations is

$$\tilde{\nabla}^2 \check{c} = P\epsilon \tilde{\mathbf{v}} \cdot \tilde{\nabla} \check{c} - \frac{(\tilde{\nabla} \check{c})^2 + (\tilde{\nabla} \check{\rho})^2}{2} - \tilde{\nabla} \tilde{\phi} \cdot \tilde{\nabla} \check{\rho}, \quad (6.12a)$$

$$\tilde{\nabla}^2 (\check{\rho} + 2\tilde{\phi}) = P\epsilon \tilde{\mathbf{v}} \cdot \tilde{\nabla} \check{\rho} - \tilde{\nabla} \check{c} \cdot \tilde{\nabla} \check{\rho} - \tilde{\nabla} \tilde{\phi} \cdot \tilde{\nabla} \check{\rho}, \quad (6.12b)$$

$$\tilde{\nabla}^2 \tilde{\phi} = -\frac{1}{\epsilon^2} e^{\check{c}/2} \sinh \left( \frac{\check{\rho}}{2} \right), \quad (6.12c)$$

$$Re(\tilde{\mathbf{v}} \cdot \tilde{\nabla}) \tilde{\mathbf{v}} = -\tilde{\nabla} \tilde{p} + \tilde{\nabla}^2 \tilde{\mathbf{v}} - \frac{1}{\epsilon^2 \alpha^2} e^{\check{c}/2} \sinh \left( \frac{\check{\rho}}{2} \right) \tilde{\nabla} \tilde{\phi}, \quad (6.12d)$$

while the continuity equation remains the same as in Equation (6.5a). The governing equations and boundary conditions for the logarithmic fields (breve-notation) is summarized in Figure 6.3.

## 6.4 The linear slip-velocity model (LS)

The double-layer screening of the electrodes leaves the bulk electrolyte charge neutral, and hence the governing equations only include the potential  $\phi$ , the pressure field  $p$  and the flow velocity field  $\mathbf{v}$ .

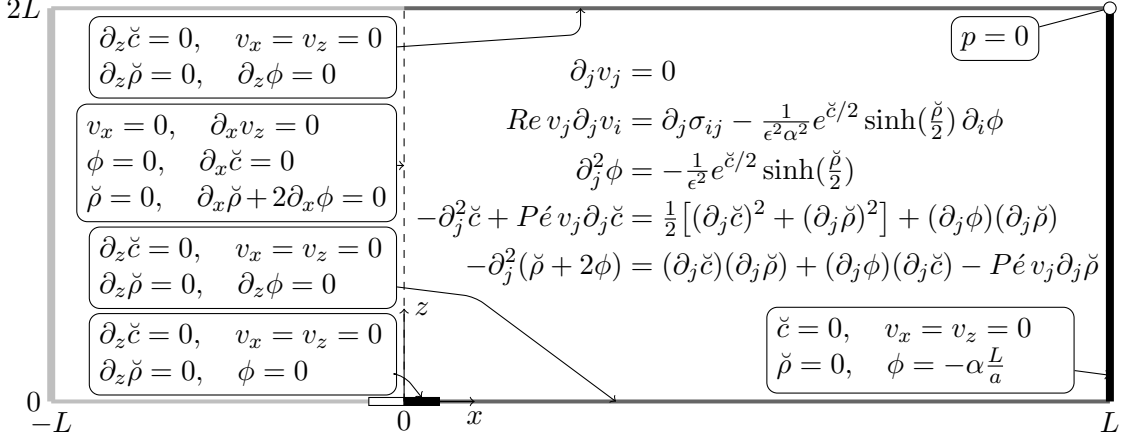


**Figure 6.3:** The governing equations (without box) and boundary conditions (with boxes) in dimensionless form (the tilde is omitted) using the logarithmic concentrations (denoted by a breve) for the full continuum model. Also, it has been necessary to distort the domain to fit the equations, but otherwise the figure is identical to Figure 6.2.

#### 6.4.1 Dimensionless form

In dimensionless form they become,

$$\tilde{\nabla}^2 \tilde{\phi} = 0, \quad (6.13a)$$

$$Re(\tilde{\mathbf{v}} \cdot \tilde{\nabla})\tilde{\mathbf{v}} = -\tilde{\nabla} \tilde{p} + \tilde{\nabla}^2 \tilde{\mathbf{v}}, \quad (6.13b)$$

$$\tilde{\nabla} \cdot \tilde{\mathbf{v}} = 0. \quad (6.13c)$$

The electrostatic problem is solved independently of the hydrodynamics, and the potential is used to calculate the effective slip velocity applied to the fluid at the un-biased electrode surface. The boundary conditions of the potential and fluid velocity are equivalent to the conditions applied to the full nonlinear system, except at the surface of the un-biased electrode. Here, the normal component of the electric field vanishes, and the effective slip velocity of the fluid is calculated from the electrostatic potential using  $\zeta = -\phi$  and  $\mathbf{E}_s = -[(\hat{\mathbf{t}} \cdot \tilde{\nabla})\tilde{\phi}] \hat{\mathbf{t}}$ ,

$$\hat{\mathbf{n}} \cdot \tilde{\nabla} \tilde{\phi} = 0, \quad (6.14a)$$

$$\tilde{\mathbf{v}}_{hs} = \frac{1}{\alpha^2} \tilde{\phi} [(\hat{\mathbf{t}} \cdot \tilde{\nabla})\tilde{\phi}] \hat{\mathbf{t}}. \quad (6.14b)$$

This represents the simplest possible, so-called linear slip-velocity model; a model which is widely applied as a starting point for numerical simulations of actual microfluidic systems [3]. In this simple model all the dynamics of the double layer has been neglected, an assumption known to be problematic when the voltage across the electrode exceeds the thermal voltage.

## 6.5 The nonlinear slip-velocity model (NLS)

### 6.5.1 Dimensionless form

Conservation of charge takes the dimensionless form

$$0 = \hat{\mathbf{n}} \cdot (\tilde{\nabla} \tilde{\phi}) + \tilde{\nabla}_s \cdot [Du \tilde{\nabla}_s \cdot \tilde{\phi}], \quad (6.15)$$

and at the edges of the electrode

$$Du(\hat{\mathbf{t}} \cdot \nabla)\phi|_{x=\pm a} = 0. \quad (6.16)$$

In this context the Dukhin number  $Du$  is

$$Du = \frac{\sigma_s}{a\sigma} = \frac{4\lambda_D}{a}(1+m)\sinh^2\left(\frac{Ze\zeta}{k_B T}\right). \quad (6.17)$$

## 6.6 Numerics in COMSOL

We use the same approach as in Chapter 4 to implement the Helmholtz–Smoluchowski slip boundary condition for the linear and nonlinear slip-velocity models.

Furthermore, in the nonlinear slip-velocity model the Laplace equation is multiplied with the electrostatic test function  $\phi^{(t)}$  and partially integrated to get a boundary term and a bulk term

$$0 = \int_{\partial\Omega} \phi^{(t)} (\partial_i \phi) n_i ds - \int_{\Omega} (\partial_i \phi^{(t)}) (\partial_i \phi) da. \quad (6.18)$$

Then, on the un-biased electrode the boundary integration term is simplified by substitution of Equation (6.15)

$$\int_{\partial\Omega_{ue}} \phi^{(t)} (\partial_i \phi) n_i ds = - \int_{\partial\Omega_{ue}} \phi^{(t)} [\hat{t}_i \partial_i (Du \hat{t}_j \partial_j \phi)] ds. \quad (6.19)$$

Again, the resulting boundary integral is partially integrated, which gives us explicit access to the surface conduction at end-points of the un-biased electrode. This is necessary for applying the boundary conditions Equation (6.16) for the 1D PDE effective boundary condition

$$\begin{aligned} & \int_{\partial\Omega_{ue}} \phi^{(t)} [\hat{t}_i \partial_i (Du \hat{t}_j \partial_j \phi)] ds \\ &= \left[ \phi^{(t)} Du (\hat{t}_i \partial_i \phi) \right]_{x=-a}^{x=+a} - \int_{\partial\Omega_{ue}} (\hat{t}_i \partial_i \phi^{(t)}) Du (\hat{t}_j \partial_j \phi) ds. \end{aligned} \quad (6.20)$$

We re-stress, that in this formulation the zeta-potential is given by the potential just outside the Debye layer  $\zeta = -\phi$ , and it is therefore not necessary to include the zeta-potential as a separate variable.

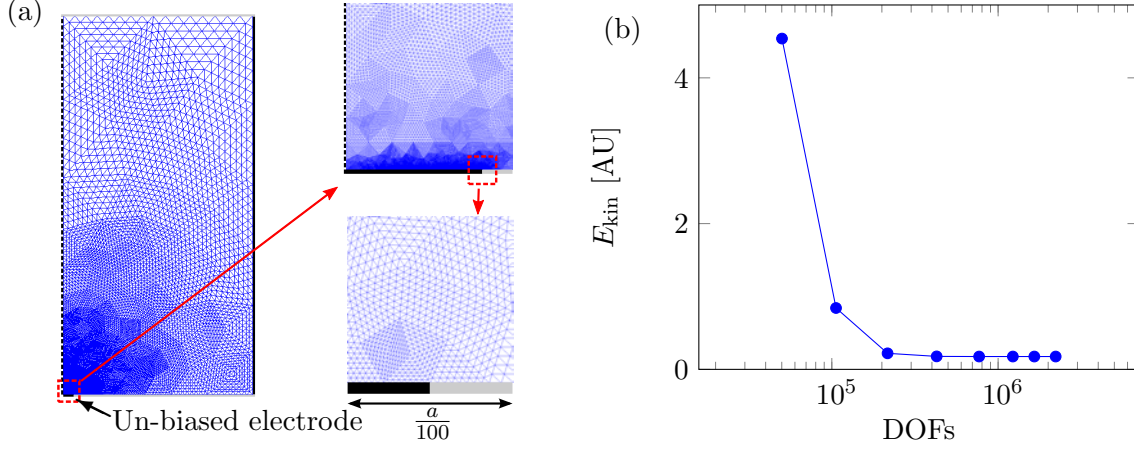


**Figure 6.4:** (a) Figure of a fully converged mesh from a computation with  $\epsilon = 0.01$  and  $\alpha = 0.1$ . The series of pictures show a zoom in on the edge of the un-biased electrode which is a singular point due to the transition from metal (constant potential) to wall (linearly varying potential), thus a kink arises with an infinite second order derivative and through Poisson's equation an infinite charge density. Because the singularity is confined to a single point the general solution is unaffected, but it requires high mesh resolution to get numerical convergence. (b) Example of a convergence run. The kinetic energy ( $E_{\text{kin}}$ , here in arbitrary units) is evaluated on a initial mesh containing a low number of DOFs. In the next step of the iteration the mesh is refined by COMSOL's build in adaptive routine and a new and more accurate solution is produced and a mesh with more DOFs. The new solution is compared to the previous solution(s), and so on. When the standard deviation relative to the mean value of five consecutive solutions is less than a given threshold value (typically  $10^{-5}$ ), the iterative run is assumed to have converged and is terminated.

### 6.6.1 Convergence analysis

The accuracy and the mesh dependence of the simulation has been investigated as follows. The comparison between the three models quantifies relative differences of orders down to  $10^{-3}$ , and the convergence of the numerical results is ensured in the following way. COMSOL has a build-in adaptive mesh generation technique that is able to refine a given mesh so as to minimize the error in the solution. The adaptive mesh generator increases the mesh density in the immediate region around the electrode to capture the dynamics of the ICEO in the most optimal way under the constraint of a maximum number of DOFs, see Figure 6.4 (a). For a given set of physical parameters, the problem is solved several times, each time increasing the number of DOFs and comparing consecutive solutions. As a convergence criterion it is demanded that the standard deviation of the kinetic energy relative to the mean value should be less than a given threshold value typically chosen to be around  $10^{-5}$ . All of the simulations ended with more than  $10^6$  DOFs, and the ICEO flow is therefore sufficiently resolved even for the thinnest double layers in the study for which  $\epsilon = 10^{-4}$ , see Figure 6.4 (b).



## 6.7 Results

The comparison of the three numerical models is primarily focused on variations of the three dimensionless parameters  $\epsilon$ ,  $\alpha$ , and  $\beta$  relating to the Debye length  $\lambda_D$ , the applied voltage  $V_0$ , and the height  $h$  of the electrode, respectively,

$$\epsilon = \frac{\lambda_D}{a}, \quad \alpha = \frac{aV_0}{L\phi_0}, \quad \beta = \frac{h}{a}. \quad (6.21)$$

The strength of the generated ICEO flow could be measured as the mechanical power input  $P_{\text{mech}}$  exerted on the electrolyte by the slip-velocity just outside the Debye layer or equivalently by the kinetic energy dissipation  $P_{\text{kin}}$  in the bulk of the electrolyte. However, both these methods suffers from numerical inaccuracies due to the dependence of both the position of the integration path and of the less accurately determined velocity gradients in the stress tensor  $\boldsymbol{\sigma}$ . To obtain a numerically more stable and accurate measure, the strength of the ICEO flow is characterized by the kinetic energy  $E_{\text{kin}}$  of the induced flow field  $\mathbf{v}$ ,

$$E_{\text{kin}} = \frac{1}{2} \rho_m \int_{\Omega} v^2 \, dx \, dz, \quad (6.22)$$

which depends on the velocity field and not its gradients, and which furthermore is a bulk integral of good numerical stability.

### 6.7.1 Zero height of the un-biased electrode

The height  $h$  of the un-biased electrode is assumed to be zero, i.e.  $\beta = 0$ , while varying the Debye length and the applied voltage through the parameters  $\epsilon$  and  $\alpha$ . Note, that the linear slip-velocity model Equations (6.13) and (6.14) is independent of the dimensionless Debye length  $\epsilon$ . It is therefore natural to use the kinetic energy  $E_{\text{kin}}^{\text{LS}}$  of this model as a normalization factor.

Figure 6.5 shows the kinetic energies in the full nonlinear  $E_{\text{kin}}^{\text{NL}}$  and nonlinear slip-velocity  $E_{\text{kin}}^{\text{NLS}}$  models, normalized by the energy  $E_{\text{kin}}^{\text{LS}}$  as a function of the inverse Debye length  $1/\epsilon$  for three different values of the applied voltage,  $\alpha = 0.05, 0.5$  and  $5$ , ranging from the linear to the strongly nonlinear voltage regime.

First note that in the limit of vanishing Debye length (to the right in the graph) all models converge toward the same value for all values of the applied voltage  $\alpha$ . For small values of  $\alpha$  the nonlinear slip-velocity model  $E_{\text{kin}}^{\text{NLS}}$  is fairly close to the linear slip-velocity model  $E_{\text{kin}}^{\text{LS}}$ , but as  $\alpha$  increases, it requires smaller and smaller values of  $\epsilon$  to obtain the same results in the two models. In the linear regime  $\alpha = 0.05$  a deviation less than 5% is obtained already for  $\epsilon < 1$ . In the nonlinear regime  $\alpha = 0.5$  the same deviation requires  $\epsilon < 10^{-2}$ , while in the strongly nonlinear regime  $\epsilon < 10^{-4}$  is needed to obtain a deviation lower than 5%.

In contrast, it is noted how the more realistic full model  $E_{\text{kin}}^{\text{NL}}$  deviates strongly from  $E_{\text{kin}}^{\text{LS}}$  for most of the displayed values of  $\epsilon$  and  $\alpha$ . To obtain a relative deviation less than 5% in the linear ( $\alpha = 0.05$ ) and nonlinear ( $\alpha = 0.5$ ) regimes, a minute Debye length of  $\epsilon < 10^{-3}$  is required, and in the strongly nonlinear regime the 5% level it not reached at all.

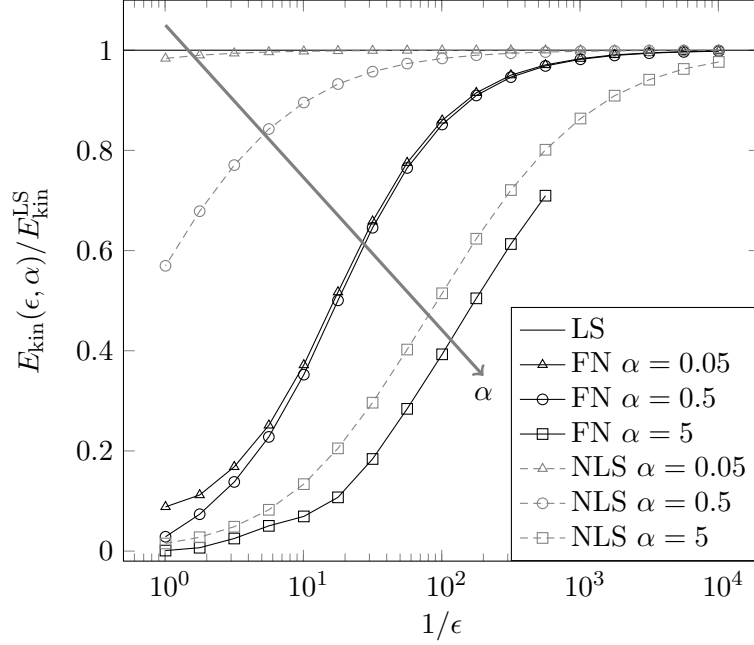


**Figure 6.5:** The total induced kinetic energy  $E_{\text{kin}}^{\text{NLS}}$  (gray dashed) and  $E_{\text{kin}}^{\text{NL}}$  (black) for the non-linear slip-velocity model and the full model, respectively, relative to  $E_{\text{kin}}^{\text{LS}}$  (horizontal black line) of the linear slip-velocity model as a function of dimensionless inverse Debye length  $1/\epsilon$ . Each are shown for three values of the dimensionless applied voltage  $\alpha = 0.05, 0.5$  and  $5$ . The value of  $\epsilon$  decreases from  $1$  to  $10^{-4}$  going from left to right.

The deviations are surprisingly large. The Debye length in typical electrokinetic experiments is  $\lambda_D = 30$  nm. For a value of  $\epsilon = 0.01$  this corresponds to an electrode of width  $2 \times 3 \mu\text{m} = 6 \mu\text{m}$ , comparable to those used in Refs. [28, 29, 19]. In Figure 6.5 we see that for  $\alpha = 5$ , corresponding to a moderate voltage drop of  $0.26$  V across the electrode, the linear slip-velocity model overestimates the ICEO strength by a factor  $1/0.4 = 2.5$ . The nonlinear slip-model does a better job. For the same parameters it only overestimates the ICEO strength by a factor  $0.5/0.4 = 1.2$ .

For more detailed comparisons between the three models, the relative overestimates of the two slip-velocity models as a function of  $\alpha$  and  $\epsilon$  are plotted in Figure 6.6 as  $(E_{\text{kin}}^{\text{LS}}/E_{\text{kin}}^{\text{NL}}) - 1$  and  $(E_{\text{kin}}^{\text{NLS}}/E_{\text{kin}}^{\text{NL}}) - 1$ , respectively. For any value of the applied voltage  $\alpha$ , both models overestimates by more than 100% for large Debye lengths  $\epsilon = 10^{-1}$  and by more than 10% for  $\epsilon = 10^{-2}$ . For the minute Debye length  $\lambda_D = 1.8 \times 10^{-3}$  the overestimates are about 3% in the linear and weakly nonlinear regime  $\alpha < 1$ , however, as we enter the strongly nonlinear regime with  $\alpha = 5$  the overestimation increases to a level above 10%.

The same data is plotted in Figure 6.7, but here in a double-logarithmic plot as a function of the inverse Debye length  $1/\epsilon$  for three different values of the applied voltage. It is clearly seen how the relative deviation decreases proportional to  $\epsilon$  as  $\epsilon$  approaches zero.

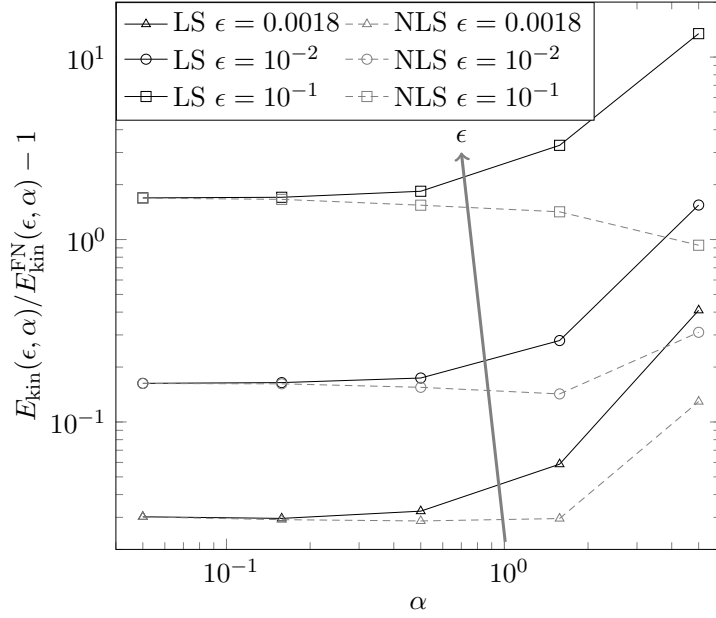


**Figure 6.6:** The difference between the induced kinetic energies  $E_{\text{kin}}^{\text{LS}}$  and  $E_{\text{kin}}^{\text{NLS}}$  of the linear and nonlinear slip-velocity models, respectively, relative to the full model  $E_{\text{kin}}^{\text{NL}}$  as a function of the voltage bias  $\alpha$  for three different Debye layer thicknesses  $\epsilon = 1.8 \times 10^{-3}, 10^{-2}, 10^{-1}$ .

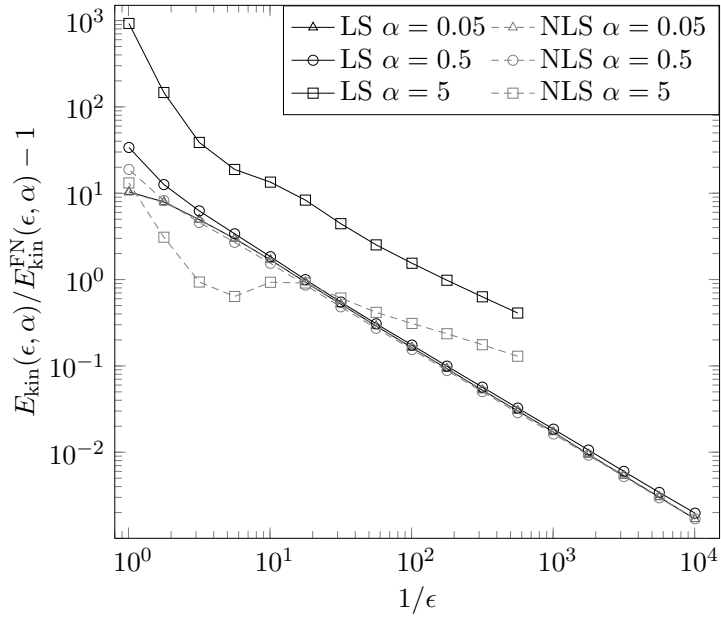


**Figure 6.7:** The difference between the induced kinetic energies  $E_{\text{kin}}^{\text{LS}}$  and  $E_{\text{kin}}^{\text{NLS}}$  of the linear and nonlinear slip-velocity models, respectively, relative to the full model  $E_{\text{kin}}^{\text{NL}}$  as a function of the inverse Debye length  $1/\epsilon$  for three different applied voltages  $\alpha = 0.05, 0.5, 5$ .

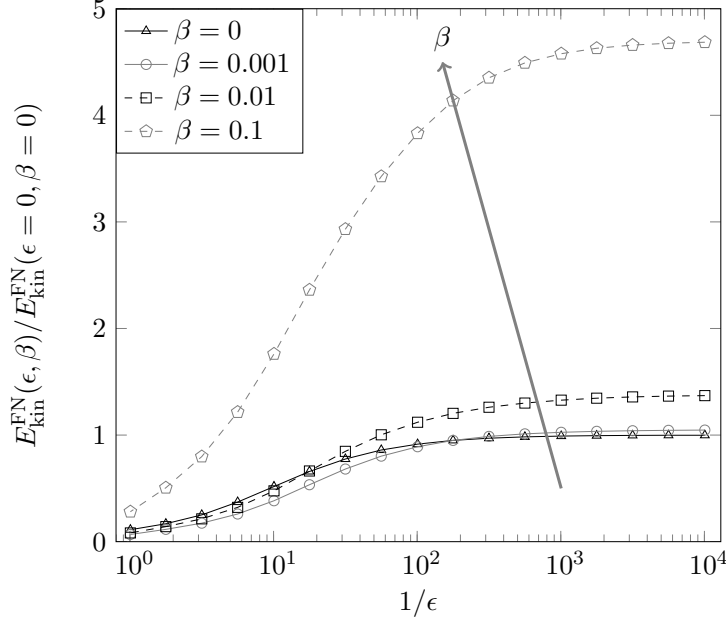


**Figure 6.8:** The difference between the induced kinetic energies  $E_{\text{kin}}^{\text{NL}}(\epsilon, \beta)$  of the full model at finite Debye length and electrode height relative to the full model  $E_{\text{kin}}^{\text{NL}}(0, 0)$  at zero Debye length and zero electrode height as a function of the inverse Debye length  $1/\epsilon$  for four electrode heights  $\beta = 0, 10^{-3}, 10^{-2}, 10^{-1}$ .

### 6.7.2 Finite height of the un-biased electrode

Compared to the full numerical model, the slip-velocity models are convenient to use, but even for small Debye lengths, say  $\lambda_D = 0.01a$ , they are prone to significant quantitative errors as shown above. Similarly, it is of relevance to study how the height of the un-biased electrode influences the strength of the ICEO flow rolls. In experiments the thinnest electrodes are made by evaporation techniques. The resulting electrode heights are of the order 50 nm – 200 nm, which relative to the typical electrode widths  $a \approx 5 \mu\text{m}$  results in dimensionless heights  $10^{-3} < \beta < 10^{-1}$ .

Figure 6.8 shows the results for the numerical calculation of the kinetic energy  $E_{\text{kin}}^{\text{NL}}(\epsilon, \beta)$  using the full numerical model. The dependence on the kinetic energy of the dimensionless Debye length  $\epsilon = \lambda_D/a$  and the dimensionless electrode height  $\beta = h/a$  is measured relative to the value  $E_{\text{kin}}^{\text{NL}}(\epsilon, \beta)$  of the infinitely small Debye length for an electrode of zero height.

For small values of the height no major deviations are seen. The curve for  $\beta = 0$  and  $\beta = 0.001$  are close. As the height is increased to  $\beta = 10^{-2}$  we note that the strength of the ICEO is increased by 20%–25% as  $\beta > \epsilon$ . This tendency is even stronger pronounced for the higher electrode  $\beta = 10^{-1}$ . Here the ICEO strength is increased by approximately 400% for a large range of Debye lengths.

## 6.8 Conclusion

We show that the ICEO velocities calculated using the simple zero-width models significantly overestimates those calculated in more realistic models taking the finite size of the Debye screening length into account. This may provide a partial explanation of the observed quantitative discrepancy between observed and calculated ICEO velocities. The discrepancy increases substantially for increasing  $\epsilon$ , i.e. in nanofluidic systems.

Even larger deviations of the ICEO strength is calculated in the full numerical model when a small, but finite height of the un-biased electrode is taken into account.

Our study shows that for systems with a small, but non-zero Debye length of 0.001 to 0.01 times the size of the electrode, and even when the Debye-Hückel approximation is valid, a poor quantitative agreement between experiments and model calculations must be expected when applying the linear slip-velocity model based on a zero Debye-length. It is advised to employ the full numerical model of ICEO, when comparing simulations with experiments.



## Chapter 7

# Conclusion and outlook

This report has two main results: (i) an experimental and numerical investigation of the concentration drop across an un-biased electrode in a microchannel, and (ii) a study of the effect of using effective slip-velocity boundary conditions in numerical simulations of electrokinetic phenomena.

For the first part, we have conducted experiments using inverted, epifluorescence microscopy to visualize the flow in a microchannel filled with phosphate buffer and BODIPY fluorescence dye. We apply an external voltage  $V_0 = 50\text{ V} - 100\text{ V}$  between the channel-inlets whereby two electrokinetic effects are induced in the system: (i) an EO-flow, and (ii) an electric double-layer on the un-biased electrode. We observe a characteristic drop in concentration of dye on the downstream side of the electrode and for steady-state we capture and post-process data as a function of applied voltage, and buffer- and dye concentrations. Furthermore, in order to understand the concentration drop we have carried out numerical simulations of the system. Our numerical model is characterized by: (i) a 2D computational domain with the same height  $H = 0.5\text{ }\mu\text{m}$  and length  $L = 9\text{ mm}$  as the microchannel, (ii) that the double layer of width  $\lambda_D \approx 10\text{ nm} - 50\text{ nm}$  is resolved on the un-biased electrode, (iii) a Helmholtz–Smoluchowski slip-velocity on the channel walls. We compare the numerical results to the experimental data and find a qualitatively agreement for the concentration drop on two parameters: (i) it increases with increasing applied voltage, and (ii) it depends on the absolute and relative concentrations of buffer and dye. Additionally, from our numerical results we show that the symmetry of the system is broken by the left-to-right going EO-flow which by convection distorts the charge density in the Debye-layer on the un-biased electrode. Consequently, a complicated situation arises which results in a reduction and amplification of the up- and downstream electric field, respectively. All together, the transport of charged species is affected by these coupled phenomena and the result is a concentration drop on the downstream side of the un-biased electrode. However, we only reproduce the concentration drop numerically and provide some insight in the dynamics; a more detailed physical explanation could be a candidate for future studies.

For the second part, we report a numerical study of the difference between a linear slip-velocity model, a nonlinear slip-velocity model, and a full nonlinear model, used for

calculations of an ICEO flow. Our model system is a microchamber filled with a binary electrolyte and containing a flat un-biased center electrode at one wall. The linear slip-velocity model does not resolve the double layer and ignores tangential charge transport inside double-layer. The nonlinear slip-velocity model extends the linear model as it includes the tangential charge transport inside the double layer. The full nonlinear continuum model resolves the double layer. We show that compared to the full model, the slip-velocity models significantly overestimate the ICEO flow. This could provide a partial explanation of the quantitative discrepancy between observed and calculated ICEO velocities reported in the literature. The discrepancy increases significantly for increasing Debye length relative to the electrode size, i.e. for nanofluidic systems. However, even for electrode dimensions in the micrometer range, the discrepancies due to the finite Debye length can be more than 10% for an electrode of zero height and more than 100% for electrode heights comparable to the Debye length. Thus, future research should try to explain the dynamics in the double layer of an ICEO flow such that more precise slip-velocity models can be derived.

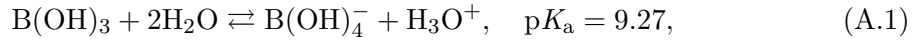


# Appendix A

## Borate buffer and fluorescein dye

### A.1 Borate buffer

The borate buffer used in the current work is an aqueous solution of orthoboric acid  $\text{B(OH)}_3$  that mainly forms two charged species when it is dissolved in water; hydronium ions  $\text{H}_3\text{O}^+$  and borate ions  $\text{B(OH)}_4^-$  in the reaction



where polynuclear boron species such as  $\text{B}_3\text{O}_3(\text{OH})_4^-$ ,  $\text{B}_4\text{O}_5(\text{OH})_4^{2-}$ , and  $\text{B}_5\text{O}_6(\text{OH})_4^-$  are negligible at concentrations below 25 mM [30]. Additionally, the solubility of boric acid powder in water is 0.94 M, higher than the maximum concentration of 10 mM used in the experiment, and thus no powder remains in solid form but is completely dissolved [12]. The acid dissociation constant  $\text{p}K_{\text{a}}$  is for a temperature of 20 °C [13].

As for the phosphate buffer, the  $\text{p}K_{\text{a}}$  in Equation (A.1) is relatively high, such that the expression in Equation (2.10) is a good approximation from which the concentrations of borate  $[\text{B(OH)}_4^-]$  and hydronium  $[\text{H}_3\text{O}^+]$  are calculated and listed in Table A.1. It is worth noting that the concentrations of charged species are relatively low in the borate buffer.

**Table A.1:** The concentrations (all in units of mM) of charged species ( $[\text{B(OH)}_4^-]$  and  $[\text{H}_3\text{O}^+]$ ) for the two concentrations (1 mM and 10 mM) of orthoboric acid ( $[\text{B(OH)}_3]$ ) in the borate buffers used in the experiments of the current work. Additionally, the pH based on Equation (2.6) is listed as this is an important parameter for the workings of the fluorescein dye.

$[\text{B(OH)}_3]$	$[\text{B(OH)}_4^-]$	$[\text{H}_3\text{O}^+]$	pH
1	$732 \times 10^{-6}$	$732 \times 10^{-6}$	6.1
10	$2.32 \times 10^{-3}$	$2.32 \times 10^{-3}$	5.6

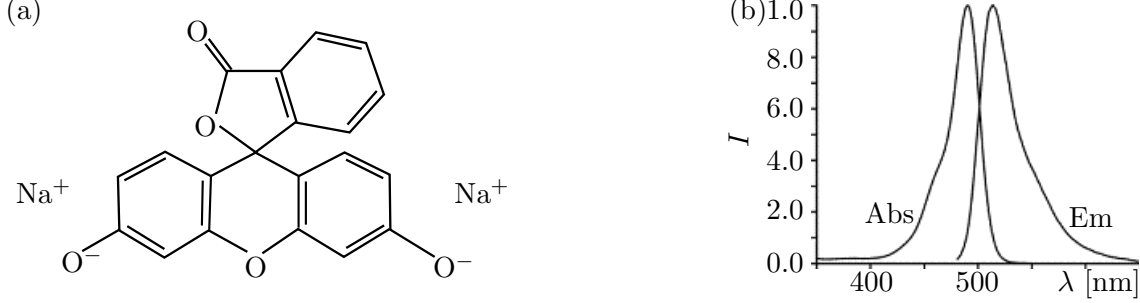


**Figure A.1:** (a) Fluorescein molecule with two negatively charged oxygen groups  $O^-$  and two dissociated, positively charged sodium atoms  $Na^+$  [31]. (b) Spectral profile of the fluorescein dye used in the current work, but in a solution of known  $pH = 9$ . The figure shows the intensity  $I$  curves of absorption Abs and emission Em as function of light wavelength  $\lambda$ , each normalized against its maximum value [33].

## A.2 Fluorescein dye

Fluorescein is a widely used fluorophore. The particular fluorescein used in the current work is the disodium salt  $C_{20}H_{10}Na_2O_5$  (denoted by  $FNa_2$ ) [31] and it is assumed to dissociate completely in an aqueous buffer through the reaction



and hence the concentrations of charged fluorescein  $[F^{2-}]$  and sodium  $[Na^+]$  are related to the initial concentration of fluorescein  $[FNa_2]$  by

$$[F^{2-}] = [FNa_2], \quad (A.3a)$$

$$[Na^+] = 2[FNa_2]. \quad (A.3b)$$

The molecular structure of fluorescein is shown in Figure A.1 (a). Additionally, fluorescein is dependent on pH and does not fluoresce for pH below 3, has a transition region for pH from 3 to 9, and has a constant fluorescence for pH above 9 [32]. Compared to the calculated pH values for the borate and phosphate buffers (Table 2.1 and A.1) this could indicate that a degree of uncertainty in the fluorescence signal from fluorescein is to be expected. Though, in a liquid of  $pH \sim 9$  the absorption and emission maxima are around 490 nm and 513 nm, see Figure A.1 (b).

## Appendix B

# COMSOL–MATLAB script for EO-flow in parallel plates

Below we show the script for the computation of an EO-flow in the validation section. Note, the script does not separate the electrostatic and hydrodynamic problems, even though this is the strong point of the linear and nonlinear slip velocity models. In this case we only use the solution for validation and the size of the problem is so small that it is not necessary to decouple the problems.

```
1 % EOF in parallel plates channel
  % Mathias Bækbo Andersen
3 % DTU Nanotech 2009

5 clear all
  close all

7
  % Parameters
9 H = 100e-6;
  L = 10*H;
11 epsr = 78;
  eps0 = 8.854e-12;
13 fem.const.ep = epsr*eps0;
  fem.const.zeta = -100e-3;
15 fem.const.eta = 1e-3;
  fem.const.V0 = 10;
17
  % Geometry
19 fem.geom = rect2(-L/2,L/2,-H/2,H/2);

21 % Mesh
  fem.mesh = meshinit(fem,'hauto',3);
23
  % Variables
25 fem.sdim = {'x' 'z'};
  fem.dim = {'u' 'v' 'p' 'phi' 'fx'};
27 fem.shape = [2,2,1,2,2];
  fem.expr = {'sigmaXX' '-p+2*eta*ux' ...
```

```

29         'sigmaXZ' 'eta*(vx+uz)' ...
        'sigmaZX' 'eta*(uz+vx)' ...
31         'sigmaZZ' '-p+2*eta*vz' };

33 % Governing equations
fem.form = 'weak';
35 fem.equ.shape = {[1:4]};
fem.equ.weak = {[ '-ux_test*sigmaXX-uz_test*sigmaXZ' ...
37               '-vz_test*sigmaZZ-vx_test*sigmaZX' ...
               'p_test*(ux+vz)' ...
39               '-phix_test*phix-phiz_test*phiz' ]};

% Boundary conditions
41 % group [1] inlet
% group [2] EOF walls
43 % group [3] outlet
fem.bnd.ind = {[4] [1 3] [2]};
45 fem.bnd.shape = {[1:4] [1:5] [1:4]};
fem.bnd.expr = {'veoX' {'{ 'ep*zeta*phiTx/eta' }}};
47 fem.bnd.weak = [{'phi_test*nx*phix' ...
                  'u_test*fx' 'fx_test*(veoX-u)' 'v_test*sigmaZZ' } ...
                  {'phi_test*nx*phix'}];
49 fem.bnd.constr = [{'V0/2-phi' '0-p' } ...
                   {'0-v' } ...
                   {'-V0/2-phi' '0-p' }];
51

53 % Point conditions
55 fem.pnt.ind = {[1 2 3 4]};
fem.pnt.shape = {[5]};
57 fem.pnt.constr = {'0-fx' };

59 % Extend mesh
fem.xmesh = meshextend(fem);
61

% Solve
63 fem.sol = femstatic(fem);

```

## Appendix C

# COMSOL–MATLAB script for concentration drop across un-biased electrode in a microchannel

We have employed the script below in the computations of the concentration drop across an un-biased electrode in a microchannel. Due to sophisticated meshing it is possible to use this script on an ordinary laptop computer despite that the model uses a real-sized geometry and resolves the finite double layer on the un-biased electrode.

```
1 % Concentration drop across un-biased electrode in a microchannel
  % Mathias Bækbo Andersen
3 % DTU Nanotech 2008

5 close all
  clear all
7
  % USER INPUT
9 fem.const.V0      = 45; % applied voltage [V]
  fem.const.NA      = 6.022e23; % Avogadros number [1/mol]
11 fem.const.ZP      = 1; % valence of positive buffer ion
  fem.const.ZN      = -1; % valence of negative buffer ion
13 fem.const.ZA      = -1; % valence of analyte
  fem.const.cN0     = 1e-2*fem.const.NA; % negative buffer ion equilibrium
    concentration [1/m^3]
15 fem.const.cA0     = 1e-3*fem.const.NA; % analyte equilibrium concentration
    [1/m^3]
  fem.const.cP0     = -(fem.const.ZN*fem.const.cN0+fem.const.ZA*fem.const.cA0)
    /fem.const.ZP; % positive buffer ion equilibrium concentration [mol/L]
17 fem.const.DP      = 2e-9; % diffusivity of positive buffer ion [m^2/s]
  fem.const.DN      = 2e-9; % diffusivity of negative buffer ion [m^2/s]
19 fem.const.DA      = 8.8e-10; % diffusivity of analyte [m^2/s]
  fem.const.a       = 60e-6; % length of floating electrode [m]
21 fem.const.L       = 9e-3; % length of channel [m]
```

```

fem.const.H      = 500e-9; % height of channel [m]
23 fem.const.zeta  = -0.1; % wall zeta potential [V]
fem.const.ton    = 0; % time at which DC bias is turned on [s]
25 fem.const.tend  = 10000; % time from turn on to simulation stop [s]
Nlong            = 100; % mesh related
27 Nelec          = 200; % mesh related
timestamp        = datestr(now,'yyyy-mm-dd'); % time of execution
29
% PHYSICAL CONSTANTS
31 fem.const.eta   = 1e-3; % dynamic viscosity [Pa*s]
fem.const.rho     = 1e3; % density [kg/m^3]
33 fem.const.epsr  = 78; % relative permittivity
fem.const.eps0    = 8.854e-12; % vacuum permittivity [F/m]
35 fem.const.e     = 1.602e-19; % electron charge [C]
fem.const.kB      = 1.381e-23; % Boltzmanns constant [J/K]
37 fem.const.T     = 293.15; % temperature [K]

39 % CALCULATED NUMBERS
fem.const.I       = (fem.const.ZP^2*fem.const.cP0+ ...
41 fem.const.ZN^2*fem.const.cN0+ ...
fem.const.ZA^2*fem.const.cA0)/2; % ionic strength
43 fem.const.lambdaD = sqrt(fem.const.epsr*fem.const.eps0*fem.const.kB*fem.
const.T/(2*fem.const.e^2*fem.const.I)); % Debye layer length

45 % PRINT TO SCREEN
fprintf(1, '\nNumbers:\n');
47 fprintf(1, 'lambda_D = %11.2g      m\n', fem.const.lambdaD);

49 % GEOMETRY
s1 = rect2(-fem.const.L/2,fem.const.L/2,0,fem.const.H);
51 s2 = rect2(-fem.const.L/2+10e-6,fem.const.L/2-10e-6,0,fem.const.H);
s3 = rect2(-100e-6,100e-6,0,fem.const.H);
53 s4 = rect2(-fem.const.a/2-500e-9,fem.const.a/2+500e-9,0,fem.const.H);
s5 = rect2(-fem.const.a/2-10e-9,-fem.const.a/2+10e-9,0,5e-9);
55 s6 = rect2(-fem.const.a/2,fem.const.a/2,0,fem.const.H/2);
s7 = rect2(-fem.const.a/2,fem.const.a/2,fem.const.H/2,fem.const.H);
57 s8 = rect2(fem.const.a/2-10e-9,fem.const.a/2+10e-9,0,5e-9);

59 c1 = line1([-fem.const.a/2+10e-9,0,fem.const.a/2-10e-9],[5e-9,20e-9,5e-9]);
c2 = line1([-fem.const.a/2,0,fem.const.a/2],[15e-9,50e-9,15e-9]);
61 c3 = line1([-fem.const.a/2,0,fem.const.a/2],[35e-9,130e-9,35e-9]);

63 p1 = point2(0,0);

65 % ANALYZED GEOMETRY
s.objs = {s1,s2,s3,s4,s5,s6,s7,s8};
67 c.objs = {c1,c2,c3};
p.objs = {p1};
69
fem.draw = struct('s',s,'c',c,'p',p);
71 fem.geom = geomcsg(fem);
% figure, geomplot(fem,'sublabels','on','edgelabels','on','pointlabels','on')
73 % return

```

```

75 % MESH
fem.mesh=meshinit(fem, ...
77     'hmaxfact',5, ...
    'hcurve',1, ...
79     'hgrad',2, ...
    'hcutoff',0.05, ...
81     'hnarrow',0.01, ...
    'hmaxvtx',[11,10e-9,25,10e-9], ...
83     'hnumedg',{1,10, ...
        5,Nlong, ...
85        6,Nlong, ...
        8,40, ...
87        9,40, ...
        11,20, ...
89        14,10, ...
        17,12, ...
91        19,12, ...
        20,5, ...
93        21,0.9*0.9*Nelec, ...
        22,10, ...
95        23,0.9*0.9*0.9*Nelec, ...
        24,5, ...
97        28,Nelec, ...
        29,0.9*Nelec, ...
99        30,Nelec, ...
        31,0.9*Nelec, ...
101        32,0.9*0.9*Nelec, ...
        33,0.9*0.9*0.9*Nelec, ...
103        35,12, ...
        36,12, ...
105        38,10, ...
        41,5, ...
107        42,10, ...
        43,5, ...
109        46,20, ...
        48,40, ...
111        49,40, ...
        51,Nlong, ...
113        52,Nlong, ...
        56,10});
115
% figure , meshplot(fem.mesh)
117 % return

119 % VARIABLES
fem.sdim = {'x' 'z'};
121 fem.dim = {'u' 'v' 'p' 'phi' 'LcP' 'LcN' 'LcA' 'lmu'};
fem.shape = [2 2 1 2 2 2 2 2];
123 fem.frame = {'ref'};
fem.expr = { ...
125     'ep' 'epsr*eps0' ... % permittivity
    'sigmaXX' '-p+2*eta*ux' ... % stress tensor component
127     'sigmaXZ' 'eta*(vx+uz)' ... % stress tensor component
    'sigmaZX' 'eta*(uz+vx)' ... % stress tensor component

```

```

129      'sigmaZZ' '-p+2*eta*vz' ... % stress tensor component
      'rhoEL' 'e*(ZP*exp(LcP)+ZN*exp(LcN)+ZA*exp(LcA))' ... % electric
          body force
131      'JLcPX' '-DP*LcPx-DP*ZP*e*phiz/(kB*T)' ... % diffusive and
          electric particle current
      'JLcPZ' '-DP*LcPz-DP*ZP*e*phiz/(kB*T)' ... % diffusive and
          electric particle current
133      'JLcNX' '-DN*LcNx-DN*ZN*e*phiz/(kB*T)' ... % diffusive and
          electric particle current
      'JLcNZ' '-DN*LcNz-DN*ZN*e*phiz/(kB*T)' ... % diffusive and
          electric particle current
135      'JLcAX' '-DA*LcAx-DA*ZA*e*phiz/(kB*T)' ... % diffusive and
          electric particle current
      'JLcAZ' '-DA*LcAz-DA*ZA*e*phiz/(kB*T)'; % diffusive and
          electric particle current
137 % INTEGRAL DOMAIN CONTRIBUTIONS
139 fem.form = 'weak';
      fem.equ.shape = {[1:7]};
141 fem.equ.dweak = {{ ...
          'u_test*rho*ut' ... % NS eq., time dependent terms
          'v_test*rho*vt' ... % NS eq., time dependent terms
          '0' ...
          '0' ...
          'LcP_test*LcPt' ... % transport eq., time dependent terms
          'LcN_test*LcNt' ... % transport eq., time dependent terms
          'LcA_test*LcAt'}}; % transport eq., time dependent terms
149 fem.equ.weak = {{ ...
          '-ux_test*sigmaXX-uz_test*sigmaXZ-u_test*rhoEL*phiz-u_test*
              rho*(u*ux+v*uz)' ... % x-component NS eq.
          '-vx_test*sigmaZX-vz_test*sigmaZZ-v_test*rhoEL*phiz-v_test*
              rho*(u*vx+v*vz)' ... % y-component NS eq.
          'p_test*(ux+vz)' ... % pressure eq.
          '-phiz_test*ep*phiz-phiz_test*ep*phiz+phi_test*rhoEL' ... %
              Poisson eq.
          'LcPx_test*JLcPX+LcPz_test*JLcPZ-LcP_test*(LcPx*JLcPX+LcPz*
              JLcPZ)-LcP_test*(u*LcPx+v*LcPz)' ... % transport eq.
          'LcNx_test*JLcNX+LcNz_test*JLcNZ-LcN_test*(LcNx*JLcNX+LcNz*
              JLcNZ)-LcN_test*(u*LcNx+v*LcNz)' ... % transport eq.
          'LcAx_test*JLcAX+LcAz_test*JLcAZ-LcA_test*(LcAx*JLcAX+LcAz*
              JLcAZ)-LcA_test*(u*LcAx+v*LcAz)'}; % transport eq.
157 % BOUNDARY CONDITIONS
159 % group [1] inlet
      % group [2] bottom wall left
161 % group [3] top wall
      % group [4] floating electrode
163 % group [5] bottom wall right
      % group [6] outlet
165 fem.bnd.ind = {[1] [2 5 8 11 14] [3 6 9 12 26 44 49 52 55] [17 28 30 35] [38
          46 48 51 54] [56]};
      fem.bnd.shape = {[1:7] [1:8] [1:8] [1:8] [1:8] [1:7]};
167 fem.bnd.expr = {'us' {'', '-ep*zeta*(-phiTx)/eta' '-ep*zeta*(-phiTx)/eta' '0'
          '-ep*zeta*(-phiTx)/eta' ''}};

```



```

169 % INTEGRAL BOUNDARY CONTRIBUTIONS
fem.bnd.weak = {{ 'v_test*sigmaZX' 'phi_test*ep*phix' '-LcP_test*JLcPX' '-
    LcN_test*JLcNX' '-LcA_test*JLcAX' } ...
171      { 'u_test*lmu' '(us-u)*lmu_test' 'v_test*sigmaZZ' } ...
      { 'u_test*lmu' '(us-u)*lmu_test' '-v_test*sigmaZZ' } ...
173      { 'u_test*lmu' '(us-u)*lmu_test' 'v_test*sigmaZZ' 'phi_test*
        ep*phiz' } ...
      { 'u_test*lmu' '(us-u)*lmu_test' 'v_test*sigmaZZ' } ...
175      { '-v_test*sigmaZX' '-phi_test*ep*phix' 'LcP_test*JLcPX' '
        LcN_test*JLcNX' 'LcA_test*JLcAX' } } };

177 % DIRICHLET CONSTRAINTS (IDEAL CONSTRAINTS)
fem.bnd.constr = {{ '0-v' '0-p' 'V0*(t>ton)/2-phi' 'log(cP0)-LcP' 'log(cN0)-
    LcN' 'log(cA0)-LcA' } ...
179      { '0-v' } ...
      { '0-v' } ...
181      { '0-v' 'phic-phi' } ...
      { '0-v' } ...
183      { '0-v' '0-p' '-V0*(t>ton)/2-phi' 'log(cP0)-LcP' 'log(cN0)-
        LcN' 'log(cA0)-LcA' } } };

185 % POINT CONDITIONS
fem.pnt.ind = {[1 2 11 25 39 40]};
187 fem.pnt.shape = {[8]};
fem.pnt.constr = {{ '0-lmu' } };
189
clear elemcpl
191 % INTEGRATION COUPLING VARIABLES
clear elem
193 elem.elem = 'elcplscalar';
elem.g = {'1'}; % geometries
195 src = cell(1,1);
clear pnt
197 pnt.expr = {{ {} , 'phi' } };
pnt.ipoints = {{ {} , '1' } };
199 pnt.frame = {{ {} , 'ref' } };
pnt.ind = {{ '1', '2', '3', '4', '5', '6', '7', '8', '9', '10', '11', '12', '13', ...
201      '14', '15', '16', '17', '18', '20', '21', '22', '23', '24', '25', ...
      '26', '27', '28', '29', '30', '31', '32', '33', '34', '35', '36', ...
203      '37', '38', '39', '40' }, {'19' } };
src{1} = {pnt, {}, {}};
205 elem.src = src;
geomdim = cell(1,1);
207 geomdim{1} = {};
elem.geomdim = geomdim;
209 elem.var = {'phic'}; % variable names
elem.global = {'1'};
211 elemcpl{1} = elem;
fem.elemcpl = elemcpl;
213
% EXTEND MESH
215 fem.xmesh = meshextend(fem);

```

```

217 % CREATE SOLUTION OBJECT
init = asseminit(fem, ...
219     'outcomp',{ 'u' 'v' 'p' 'phi' 'LcP' 'LcN' 'LcA' }, ...
    'init',{ 'u' '0' ...
221         'v' '0' ...
        'p' '0' ...
223         'phi' '0' ...
        'LcP' 'log(cP0)' ...
225         'LcN' 'log(cN0)' ...
        'LcA' 'log(cA0)' });
227
% SOLVE
229 tlist = [fem.const.ton-1e-10 (logspace(0,3,10)-1)/(10^3-1) 1+fem.const.ton+
    fem.const.tend*(logspace(0,3,40)-1)/(10^3-1)];
fem = femtime(fem, ...
231     'linsolver','pardiso', ...
    'initialstep', 0.5e-10, ...
233     'solfile','on', ...
    'tlist',tlist, ...
235     'init',init, ...
    'solcomp',{ 'u' 'v' 'p' 'phi' 'LcP' 'LcN' 'LcA' 'lmu' }, ...
237     'outcomp',{ 'u' 'v' 'p' 'phi' 'LcP' 'LcN' 'LcA' 'lmu' }, ...
    'estrat',1, ...
239     'tout','tlist', ...
    'tsteps','free', ...
241     'out','fem');

243 % SAVE
save(['Some_name_' timestamp '.mat'], 'fem')

```

## Appendix D

# COMSOL–MATLAB scripts for finite Debye-length investigation

### D.1 Grid Engine script for utilizing the high performance computing facility at DTU

We have used the high performance computing facility (HPC) at DTU for the analysis of the finite Debye-length effects in ICEO flow. This was necessary due to the large scale of the problem. The following Grid Engine script calls the COMSOL–MATLAB script and passes it on to the HPC computers where the 64-bit version of COMSOL is run on 4 processors and with a considerable large amount of RAM. The name of the script is “GE.sh” and it is executed from a UNIX terminal using the command “qsub GE.sh”

```
#!/bin/sh
2 #
# Genral options
4 ## -N name_of_job
## -S /bin/sh
6 ## -o name_of_log_file.log
## -e name_of_error_file.log
8 #
# Execute the job from the current working directory
10 ## -cwd
#
12 # Request parallel job
#
14 ## -l cre
## -pe HPC 4
16 #
# Program name and options
18 comsol -64 -np 4 matlab path -ml -nodesktop -ml -nosplash -mlr
    name_of_COMSOL_MATLAB_script
```

## D.2 Full nonlinear model

The following COMSOL–MATLAB script was used for the full nonlinear model calculations in the finite Debye-length investigation.

```

% Script for the full nonlinear model for the finite Debye-length
  investigation
2 % Mathias Bækbo Andersen
  % DTU Nanotech 2008
4
close all
6 clear all

8 format short g
  flreport('off')
10
for epsi = 0.0001
12   % PARAMETERS
    alph = 10; % applied voltage parameter
14   H = 0; % height of electrode
    sens = 5e-5; % sensitivity of std.dev.
16
    fem.const.L = 0.5;
18   fem.const.D = 2e-9; % diffusivity of symmetric electrolyte; [m^2/s]
    fem.const.Z = 1; % valence of symmetric electrolyte
20   fem.const.eta = 1e-3; % dynamic viscosity [Pa*s]
    fem.const.rhob = 1e3; % density [kg/m^3]
22   fem.const.nu = fem.const.eta/fem.const.rhob; % kinematic viscosity [m^2/
    s]
    fem.const.epsr = 78; % relative permittivity
24   fem.const.eps0 = 8.854e-12; % vacuum permittivity [F/m]
    fem.const.e = 1.602e-19; % electron charge [C]
26   fem.const.kB = 1.381e-23; % Boltzmanns constant [J/K]
    fem.const.T = 293.15; % temperature [K]
28   fem.const.phi0 = fem.const.kB*fem.const.T/(fem.const.Z*fem.const.e); %
    characteristic potential [V]
    fem.const.alph = alph;
30   fem.const.epsi = epsi;
    fem.const.H = H;
32
    % GEOMETRY
34   g1 = rect2(0,7.5,0,15);
    g2 = rect2(0,0.6,0,0.1);
36   g3 = curve2([0,0.5],[0,0]);

38   % ANALYZED GEOMETRY
    c.objs = {g3};
40   s.objs = {g1,g2};

42   fem.draw = struct('c',c,'s',s);
    fem.geom = geomcsg(fem);
44   % figure,geomplot(fem,'sublabels','on','edgelabels','on','
    pointlabels',
    % 'on'),return

```

```

46      % MESH
48      fem.mesh = meshinit(fem, ...
50          'hmaxedg',[2,0.0001], ...
52          'hmaxvtx',[4,0.00001], ...
54          'hauto',5);
56      % figure, meshplot(fem.mesh), return

58      % VARIABLES
59      fem.sdim = {'x' 'z'};
60      fem.dim = {'u' 'v' 'p' 'phi' 'c' 'rho'};
61      fem.shape = [2 2 1 2 2 2];
62      fem.expr = {'Re' 'epsr*eps0*(alph*phi0)^2/(2*nu*eta)' ...% Reynolds
63          number
64          'Pe' 'epsr*eps0*(alph*phi0)^2/(2*eta*D)' ...% Péclet number
65          'sigmaxx' '-p+2*ux' ... % stress tensor component
66          'sigmaxz' 'vx+uz' ... % stress tensor component
67          'sigmazx' 'uz+vx' ... % stress tensor component
68          'sigmazz' '-p+2*vz' ... % stress tensor component
69          'charge' 'exp(c/2)*sinh(rho/2)/epsi^2' ...
70          'crhs' '(cx^2+cz^2+rhox^2+rhoz^2)/2+Z*(phix*rhox+phiz*rhoz)-Pe*(u*cx
71          +v*cz)' ...
72          'rhorhs' '(cx*rhox+cz*rhoz)+Z*(phix*cx+phiz*cz)-Pe*(u*rhox+v*rhoz)'
73          };

74      % GOVERNING EQUATIONS
75      fem.form = 'weak';
76      fem.equ.shape = {[1:6]};

77      % INTEGRAL DOMAIN CONTRIBUTIONS
78      fem.equ.weak = {{'-ux_test*sigmaxx-uz_test*sigmaxz-u_test*(Re*(u*ux+v*uz
79          )+2*Z*phix*charge/alph^2)' ... % x-component NS eq.
80          '-vx_test*sigmaxz-vz_test*sigmazz-v_test*(Re*(u*vx+v*vz)+2*Z*phiz*
81          charge/alph^2)' ... % y-component NS eq.
82          'p_test*(ux+vz)' ... % pressure eq.
83          '-phix_test*Z*phix-phiz_test*Z*phiz+phi_test*charge' ... % Poisson
84          eq.
85          '-cx_test*cx-cz_test*cz+c_test*crhs' ... % Nernst-Planck
86          '-rhox_test*(rhox+2*Z*phix)-rhoz_test*(rhoz+2*Z*phiz)+rho_test*
87          rhorhs'}}; % Nernst-Planck

88      % BOUNDARY CONDITIONS
89      % group [1] solid walls
90      % group [2] floating electrode
91      % group [3] external electrode
92      % group [4] open boundary
93      % group [5] symmetry boundary
94      fem.bnd.ind = {[6 8] [2] [9] [5] [1 3]};

95      % INTEGRAL BOUNDARY CONTRIBUTIONS
96      fem.bnd.weak = {{ 'u_test*sigmaxx' 'v_test*sigmazz' } ...
97          { 'u_test*sigmaxz' 'v_test*sigmazz' 'phi_test*Z*phiz' } ...
98          { '-u_test*sigmaxx' '-v_test*sigmaxz' '-phi_test*Z*phix' '-c_test*cx'
99          '-rho_test*(rhox+2*Z*phix)' } ...

```

```

92      {'-u_test*sigmaxz' '-v_test*sigmaz' '-c_test*cz' '-rho_test*rhoz'}
93      ...
94      {'u_test*sigmaxx' 'v_test*uz' 'phi_test*Z*phix'}}};

96      % DIRICHLET CONSTRAINTS (IDEAL CONSTRAINTS)
97      fem.bnd.constr = {{'0-u' '0-v'} ...
98      {'0-u' '0-v' '0-phi'} ...
99      {'0-u' '0-v' '-alph*15/(2*Z)-phi' '0-c' '0-rho'} ...
100     {'0-u' '0-v' '0-c' '0-rho'} ...
101     {'0-u' '0-phi' '0-rho'}}};

102     % POINT CONDITIONS
103     % Clamp pressure at a single point to fix the pressure level
104     fem.pnt.ind = {[8]};
105     fem.pnt.shape = {[3]};
106     fem.pnt.constr = {'0-p'};

108     % EXTEND MESH
109     fem.xmesh = meshextend(fem);

110
111     Nnp0 = flngdof(fem); % get DOFs

112
113     % SOLVE
114
115     tic
116
117     [fem,Nnp] = adaption(fem, ...
118     'solfile','on', ...
119     'nonlin','on', ...
120     'hnlm','off', ...
121     'solver','stationary', ...
122     'linsolver','pardiso', ...
123     'maxiter',1000, ...
124     'ngen',1, ...
125     'maxt',100000, ...
126     'rmethd','meshinit', ...
127     'tpfun','fltpft', ...
128     'tppar',0.9, ...
129     'hauto',8, ...
130     'out',{'fem' 'Nnp'});

132     % SAVE
133     fem0 = fem;

134
135     % POST PROCESS
136     time = toc; % get time

137
138     time0 = time; % save time

139
140     Nnp0 = [Nnp0 Nnp]; % save DOFs

141
142     ind = [];

143
144     v2avg0 = postint(fem,'u^2+v^2')./postint(fem,'1'); % calculated induced

```

```

    kinetic energy
146     h = posteval(fem,'h','edim',2); % find minimum element size
148     h0 = min(h.d);
150     save(['epsi=' num2str(fem.const.epsi,'%7.6f') '_conv_' datestr(now,'yyyy-
    mm-dd') '.mat'], 'Nnp0','v2avg0','h0','time0')
152     save(['epsi=' num2str(fem.const.epsi,'%7.6f') '_fem_' datestr(now,'yyyy-
    mm-dd') '.mat'], 'fem')
154     fprintf(1,'\nalph:%3.1f, epsi:%7.6f\n',fem.const.alph,fem.const.epsi);
    fprintf(1,'DOFs:%8.0f, time:%6.0f, h.d:%3.2e\n',Nnp,time,min(h.d));
156
    maxdof = 5000000; % stop criteria for loop
158
    ndev = 5; % stop criteria for loop
160    stddev = 1; % stop criteria for loop
162    while ((max(stddev) > sens) || (Nnp < 1e6)) && (1.2*Nnp < maxdof) && Nnp
        ~= Nnp0(end-1)
164        % CHECK MINIMUM ELEMENT SIZE
        if min(h.d) > 1.75e-6
166            string1 = 'meshinit';
            string2 = 'fltpft';
168            string3 = 0.9;
        else
170            string1 = 'regular';
            string2 = 'fltpqty';
172            string3 = 1;
        end
174
        %SOLVE
176        tic
178        [fem,Nnp] = adaption(fem, ...
            'init',fem0.sol, ...
180            'u',fem0.sol, ...
            'solfile','on', ...
182            'solver','stationary', ...
            'linsolver','pardiso', ...
184            'nonlin','on', ...
            'hnlin','off', ...
186            'maxiter',1000, ...
            'ngen',1, ...
188            'rmethd',string1, ...
            'tpfun',string2, ...
190            'tppar',string3, ...
            'hauto',8, ...
192            'out',{'fem' 'Nnp'});
194
        % SAVE

```

```

196     fem0 = fem;
198     % POST PROCESS
198     time = toc;
200     time0 = [time0 time];
202     ind = [];
204     v2avg = postint(fem, 'u^2+v^2') ./ postint(fem, '1');
206     v2avg0 = [v2avg0; v2avg];
208     if size(v2avg0, 1) >= ndev
210         stddev = sqrt(sum((v2avg0(end-ndev+1:end)-mean(v2avg0(end-ndev
                +1:end)))^2) ./ mean(v2avg0(end-ndev+1:end)));
212     end
214     Nnp0 = [Nnp0 Nnp];
216     h = posteval(fem, 'h', 'edim', 2);
218     h0 = [h0 min(h.d)];
220     save(['epsi=' num2str(fem.const.epsi, '%7.6f') '_conv_' datestr(now, '
        yyyy-mm-dd') '.mat'], 'Nnp0', 'v2avg0', 'h0', 'time0');
222     save(['epsi=' num2str(fem.const.epsi, '%7.6f') '_fem_' datestr(now, '
        yyyy-mm-dd') '.mat'], 'fem');
224     fprintf(1, 'DOFs:%8.0f, time:%6.0f, h.d:%3.2e, std.dev.:%3.2e\n', Nnp,
        time, min(h.d), stddev);
226     end
228     fprintf(1, '\nEnd of script\n\n')
230     return

```

### D.3 Linear slip model

The COMSOL–MATLAB script for the linear slip-velocity model deviates only slightly from the full nonlinear model script. Thus, we only list the differences below.

```

% Script for the linear slip velocity model for the finite Debye-length
  investigation
2 % Mathias Bækbo Andersen
% DTU Nanotech 2008

```

```

% VARIABLES

```



```

44 fem.sdim = {'x' 'y'};
   fem.dim = {'u' 'v' 'p' 'phi' 'fx' 'fy'};
46 fem.shape = [2 2 1 2 2 2];
   fem.expr = {'sigmaxx' '-p+2*ux' ... % stress tensor component
48             'sigmaxy' 'vx+uy' ... % stress tensor component
             'sigmayx' 'uy+vx' ... % stress tensor component
50             'sigmayy' '-p+2*vy'}; % stress tensor component

52 % GOVERNING EQUATIONS
   fem.form = 'weak';
54 fem.equ.shape = {[1:4]};
   fem.equ.weak = {'-ux_test*sigmaxx-uy_test*sigmaxy-u_test*Re*(u*ux+v*vy)'
   ...
56                  '-vx_test*sigmayx-vy_test*sigmayy-v_test*Re*(u*vx+v*vy)'
   ...
                  'p_test*(ux+vy)' ...
58                  '-phix_test*phix-phiy_test*phiy'};

60 % BOUNDARY CONDITIONS
   % group [1] solid walls
62 % group [2] floating electrode
   % group [3] external electrode
64 % group [4] open boundary
   % group [5] symmetry boundary
66 fem.bnd.ind = {[6 8] [2] [9] [5] [1 3]};
   fem.bnd.shape = {[1:4] [1:6] [1:4] [1:4] [1:4]};
68 fem.bnd.expr = {'us' '-2*phi*phiTx/alph^2' 'vs' '-2*phi*phiTy/alph^2'};
   fem.bnd.weak = {'u_test*sigmaxy' 'v_test*sigmayy'} ...
70                  {'u_test*fx' 'v_test*fy' 'fx_test*(us-u)' 'fy_test*(vs-v)'}
   ...
                  {'-u_test*sigmaxx' '-v_test*sigmayx' '-phi_test*phix'} ...
72                  {'-u_test*sigmaxy' '-v_test*sigmayy'} ...
                  {'u_test*sigmaxx' 'v_test*uy' 'phi_test*phix'};
74 fem.bnd.constr = {'0-u' '0-v'} ...
                   {} ...
76                   {'0-u' '0-v' '-alph*15/2-phi'} ...
                   {'0-u' '0-v'} ...
78                   {'0-u' '0-phi'};

80 % POINT CONDITIONS
   % Clamp pressure at a single point to fix the pressure level
82 fem.pnt.ind = {[8] [1 4]};
   fem.pnt.shape = {[3] [5 6]};
84 fem.pnt.constr = {'0-p' {'0-fx' '0-fy'}};

```

## D.4 Nonlinear slip model

Again, we only include the differences to the full nonlinear model script here. Note, in this script we solve the decoupled electrostatic problem first and then the hydrodynamic problem.

```
% Script for the nonlinear slip velocity model in the finite Debye length
    investigation
2 % Mathias Bækbo Andersen & Gaurav Soni
% DTU Nanotech 2008
```

```
% VARIABLES
62 fem.sdim = {'x' 'z'};
fem.dim = {'u' 'v' 'p' 'phi' 'f'};
64 fem.shape = [2 2 1 2 2];
fem.expr = {'sigmaxx' '-p+2*ux' ... % stress tensor component
66 'sigmaxz' 'vx+uz' ... % stress tensor component
'sigmaxz' 'uz+vx' ... % stress tensor component
68 'sigmazx' '-p+2*vz'}; % stress tensor component

70 % INTEGRAL DOMAIN CONTRIBUTIONS
fem.form = 'weak';
72 fem.equ.shape = {[1:4]};
fem.equ.weak = {'-ux_test*sigmaxx-uz_test*sigmaxz-u_test*Re*(u*ux+v*uz)
' ... % x-component NS eq.
74 '-vx_test*sigmaxz-vz_test*sigmazx-v_test*Re*(u*vx+v*vz)' ... % y-
component NS eq.
'p_test*(ux+vz)' ... % pressure eq.
76 '-phix_test*phix-phiz_test*phiz'}; % Laplace eq.

78 % BOUNDARY CONDITIONS
% group [1] solid walls
80 % group [2] floating electrode
% group [3] external electrode
82 % group [4] open boundary
% group [5] symmetry boundary
84 fem.bnd.ind = {[6 8] [2] [9] [5] [1 3]};
fem.bnd.shape = {[1:4] [1:5] [1:4] [1:4] [1:4]};
86 fem.bnd.expr = {'Du' {'' '4*epsi*(1+m)*sinh(-phi/4)^2' '' '' ''}} ... %
Dukhin number on electrode
'us' {'' '-2*phiTx*phi/alph^2' '' '' ''}}; % eo slip on electrode
88

90 % INTEGRAL BOUNDARY CONTRIBUTIONS
fem.bnd.weak = {'u_test*sigmaxz' 'v_test*sigmazx' ...
{'u_test*f' 'f_test*(us-u)' 'v_test*sigmazx' '-phiTx_test*Du*phiTx'}
...
92 {'-u_test*sigmaxx' '-v_test*sigmaxz' '-phi_test*phix'} ...
{'-u_test*sigmaxz' '-v_test*sigmazx' ...
94 {'u_test*sigmaxx' 'v_test*uz' 'phi_test*phix'}};

96 % DIRICHLET CONSTRAINTS (IDEAL CONSTRAINTS)
fem.bnd.constr = {'0-u' '0-v' ...
98 {'0-v' ...
{'0-u' '0-v' '-alph*15/2-phi'} ...
100 {'0-u' '0-v' } ...
{'0-u' '0-phi'}};
102

104 % POINT CONDITIONS
% group [1] midpoint of floating electrode
% group [2] right end point of floating electrode
```

```

106      % group [3] upper right hand corner of domain
      fem.pnt.ind = {[1] [4] [8]};
108      fem.pnt.shape = {[4:5] [4:5] [3]};
      fem.pnt.expr = {'Du' {'4*epsi*(1+m)*sinh(-phi/4)^2' '' ''}};
110      fem.pnt.weak = {'-phi_test*Ductx' ...
          {} ...
112      {}};
      fem.pnt.constr = {'0-phi' '0-f' ...
114      {'0-f' ...
          {'0-p'}};

```



# Bibliography

- [1] H. A. Stone, A. D. Stroock, and A. Ajdari, “Engineering flows in small devices: Microfluidics toward a lab-on-a-chip,” *Annual review of fluid mechanics*, vol. 36, pp. 381–411, 2004.
- [2] “Microfluidic (keyword search).” <http://www.isiwebofknowledge.com/>, January 2009. ISI Web of Knowledge.
- [3] H. Bruus, *Theoretical microfluidics*. Oxford University Press, 2008.
- [4] “Introduction to fluorescence microscopy.” <http://www.microscopyu.com/articles/-fluorescence/fluorescenceintro.html>, February 2009. Nikon MicroscopyU.
- [5] R. B. Schoch, P. Renaud, R. B. Schoch, J. Han, R. B. Schoch, J. Han, and R. B. Schoch, “Transport phenomena in nanofluidics,” *Reviews of Modern Physics*, vol. 80, no. 3, pp. 839–883, 2008.
- [6] F. Persson, L. H. Thamdrup, M. B. L. Mikkelsen, S. E. Jaarlgard, P. Skafte-Pedersen, H. Bruus, and A. Kristensen, “Double thermal oxidation scheme for the fabrication of sio2 nanochannels,” *Nanotechnology*, vol. 18, p. 245301, 2007.
- [7] L. H. Thamdrup, F. Persson, H. Bruus, A. Kristensen, and H. Flyvbjerg, “Experimental investigation of bubble formation during capillary filling of sio2 nanoslits,” *Applied Physics Letters*, vol. 91, p. 163505, 2007.
- [8] S. Pennathur and J. G. Santiago, “Electrokinetic transport in nanochannels. 1. theory,” *Analytical Chemistry*, vol. 77, pp. 6772–6781, 2005.
- [9] S. Pennathur and J. G. Santiago, “Electrokinetic transport in nanochannels. 2. experiments,” *Analytical Chemistry*, vol. 77, pp. 6782–6789, 2005.
- [10] T. Vo-Dinh, *Biomedical Photonics Handbook*. CRC Press LLC, 2003.
- [11] “Acid-base reaction.” <http://www.search.eb.com/globalproxy.cvt.dk/eb/article-49257>, 26 January 2009. Encyclopædia Britannica Online.
- [12] D. R. Lide, “Physical constants of inorganic compounds.” CRC Handbook of Chemistry and Physics, 89th Edition (Internet Version 2009), January 2009. CRC Press/-Taylor and Francis, Boca Raton, FL.

- [13] D. R. Lide, "Dissociation constants of inorganic acids and bases." CRC Handbook of Chemistry and Physics, 89th Edition (Internet Version 2009), January 2009. CRC Press/Taylor and Francis, Boca Raton, FL.
- [14] A. Loudet and K. Burgess, "BODIPY dyes and their derivatives: Syntheses and spectroscopic properties," *Chemical Reviews*, vol. 107, pp. 4891–4932, 2007.
- [15] "Product structure B10006." <http://www.invitrogen.com/site/us/en/home/support/Product-Technical-Resources/Product-Structures.-10006.html>, January 2009. Invitrogen Corporation.
- [16] "Product spectra - BODIPY FL/MeOH." <http://www.invitrogen.com/site/us/en/home/support/Product-Technical-Resources/Product-Spectra.2184moh.html>, January 2009. Invitrogen Corporation.
- [17] R. Bharadwaj, J. G. Santiago, and B. Mohammadi, "Design and optimization of on-chip capillary electrophoresis," *Electrophoresis*, vol. 23, pp. 2729–2744, 2002.
- [18] R. Dhopeswarkar, D. Hlushkou, M. Nguyen, U. Tallarek, and R. M. Crooks, "Electrokinetics in microfluidic channels containing a floating electrode," *Journal of the American Chemical Society*, vol. 130, pp. 10480–10481, 2008.
- [19] M. M. Gregersen, L. H. Olesen, A. Brask, M. F. Hansen, and H. Bruus, "Flow reversal at low voltage and low frequency in a micro-fabricated AC electrokinetic pump," *Physical Review E*, vol. 76, p. 056305, 2007.
- [20] L. H. Olesen, *AC Electrokinetic micropumps*. PhD thesis, Technical University of Denmark, 2006.
- [21] G. Soni, T. M. Squires, and C. D. Meinhart, "Nonlinear phenomena in induced charge electroosmosis," in *Proceedings of IMECE2007*, 2007.
- [22] B. D. Storey, L. R. Edwards, M. S. Kilic, and M. Z. Bazant, "Steric effects on ac electro-osmosis in dilute electrolytes," *Physical Review E*, vol. 77, p. 036317, 2008.
- [23] A. J. Bard and L. R. Faulkner, *Electrochemical methods: fundamentals and applications*. John Wiley & Sons, Inc., 2001.
- [24] A. S. Khair and T. M. Squires, "Surprising consequences of ion conservation in electroosmosis over a surface charge discontinuity," *Journal of Fluid Mechanics*, vol. 615, pp. 323–334, 2008.
- [25] *COMSOL Multiphysics User's Guide*.
- [26] C. K. Harnett, J. Templeton, Dunphy-Guzman, K. A, Y. M. Senousy, and M. P. Kanouff, "Model based design of a microfluidic mixer driven by induced charge electroosmosis," *Lab on a Chip*, vol. 8, pp. 565–572, 2008.

- [27] T. M. Squires and M. Z. Bazant, "Induced-charge electro-osmosis," *Journal of Fluid Mechanics*, vol. 509, pp. 217–252, 2004.
- [28] V. Studer, A. Pépin, Y. Chen, and A. Ajdari, "An integrated AC electrokinetic pump in a microfluidic loop for fast and tunable flow control," *The Analyst*, vol. 129, pp. 944–949, 2004.
- [29] B. P. Cahill, A. Stemmer, L. J. Heyderman, and J. Gobrecht, "Electro-osmotic streaming on application of traveling-wave electric fields," *Physical Review E*, vol. 70, p. 036305, 2004.
- [30] R. E. Zeebe, A. Sanyal, J. D. Ortiz, and D. A. Wolf-Gladrow, "A theoretical study of the kinetics of the boric acid-borate equilibrium in seawater," *Marine Chemistry*, vol. 73, pp. 113–124, 2001.
- [31] D. R. Lide, "Physical constants of organic compounds." CRC Handbook of Chemistry and Physics, 89th Edition (Internet Version 2009), January 2009. CRC Press/Taylor and Francis, Boca Raton, FL.
- [32] P. L. Desbne, C. J. Morin, A. M. D. Monvernay, and R. S. Groult, "Utilization of fluorescein sodium salt in laser-induced indirect fluorimetric detection of ions separated by capillary zone electrophoresis," *Journal of Chromatography A*, vol. 689, pp. 135–148, 1995.
- [33] "Product spectra - fluorescein/pH 9.0." <http://www.invitrogen.com/site/us/en/home/support/Product-Technical-Resources/Product-Spectra.1300ph9.html>, January 2009. Invitrogen Corporation.